

1-1-2004

The volcanology and petrogenesis of the Northern Lunar Crater Volcanic Field, Nye County, Nevada

Elizabeth Kay Stickney
University of Nevada, Las Vegas

Follow this and additional works at: <https://digitalscholarship.unlv.edu/rtds>

Repository Citation

Stickney, Elizabeth Kay, "The volcanology and petrogenesis of the Northern Lunar Crater Volcanic Field, Nye County, Nevada" (2004). *UNLV Retrospective Theses & Dissertations*. 1637.
<http://dx.doi.org/10.25669/dma6-dii1>

This Thesis is protected by copyright and/or related rights. It has been brought to you by Digital Scholarship@UNLV with permission from the rights-holder(s). You are free to use this Thesis in any way that is permitted by the copyright and related rights legislation that applies to your use. For other uses you need to obtain permission from the rights-holder(s) directly, unless additional rights are indicated by a Creative Commons license in the record and/or on the work itself.

This Thesis has been accepted for inclusion in UNLV Retrospective Theses & Dissertations by an authorized administrator of Digital Scholarship@UNLV. For more information, please contact digitalscholarship@unlv.edu.

INFORMATION TO USERS

This manuscript has been reproduced from the microfilm master. UMI films the text directly from the original or copy submitted. Thus, some thesis and dissertation copies are in typewriter face, while others may be from any type of computer printer.

The quality of this reproduction is dependent upon the quality of the copy submitted. Broken or indistinct print, colored or poor quality illustrations and photographs, print bleedthrough, substandard margins, and improper alignment can adversely affect reproduction.

In the unlikely event that the author did not send UMI a complete manuscript and there are missing pages, these will be noted. Also, if unauthorized copyright material had to be removed, a note will indicate the deletion.

Oversize materials (e.g., maps, drawings, charts) are reproduced by sectioning the original, beginning at the upper left-hand corner and continuing from left to right in equal sections with small overlaps.

ProQuest Information and Learning
300 North Zeeb Road, Ann Arbor, MI 48106-1346 USA
800-521-0600

UMI[®]

THE VOLCANOLOGY AND PETROGENESIS OF THE
NORTHERN LUNAR CRATER VOLCANIC
FIELD, NYE COUNTY
NEVADA

by

Elizabeth Kay Stickney

Bachelor of Science
University of California at Santa Cruz
1997

A thesis submitted in partial fulfillment
of the requirement for the degree of

Master of Science Degree in Geoscience
Department of Geoscience
College of Sciences

Graduate College
University of Nevada, Las Vegas
May 2004

UMI Number: 1422156



UMI Microform 1422156

Copyright 2004 by ProQuest Information and Learning Company.

All rights reserved. This microform edition is protected against
unauthorized copying under Title 17, United States Code.

ProQuest Information and Learning Company
300 North Zeeb Road
P.O. Box 1346
Ann Arbor, MI 48106-1346



Thesis Approval

The Graduate College
University of Nevada, Las Vegas

DECEMBER 3, 2004

The Thesis prepared by

ELIZABETH KAY STICKNEY

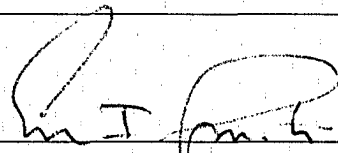
Entitled

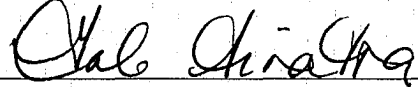
THE VOLCANOLOGY AND PETROGENESIS OF THE NORTHERN LUNAR CRATER


VOLCANIC FIELD, NYE COUNTY, NEVADA

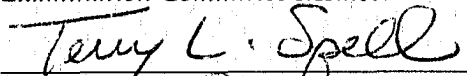
is approved in partial fulfillment of the requirements for the degree of

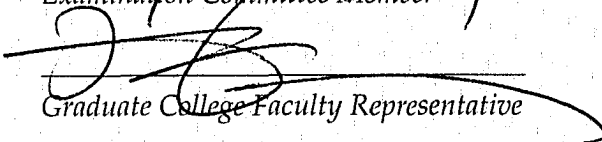
MASTER OF SCIENCE IN GEOSCIENCE


Examination Committee Chair


Dean of the Graduate College


Examination Committee Member


Examination Committee Member


Graduate College Faculty Representative

ABSTRACT

The Volcanology and Petrogenesis of the Northern Lunar Crater Volcanic Field, Nye County, Nevada

by

Elizabeth Kay Stickney

Dr. Eugene I. Smith, Examination Committee Chair
Professor of Geoscience
University of Nevada, Las Vegas

The Northern Lunar Crater Volcanic Field (NLCVF) is located along the axis of the Great Basin in Nye County, Nevada. This area of Pliocene to Recent cinder cones, maars and alkali basalt lava flows represents the northern terminus of the Death Valley-Pancake Range Basalt Zone. Basalts from this area can be divided into two distinct groups, those of trace element enrichment relative to Ocean Island Basalt, and those of trace element depletion relative to Ocean Island Basalt, with each group containing a range of compositions. The NLCVF represents a simple volcanic area, with basalts formed by differing degrees of partial melting, independent of one another with no evidence for crustal contamination or commingling. A mantle melting column for the area indicates a deep (176 to 130 km) asthenospheric mantle source with temperatures 200° C hotter than average. This might be attributed to a mantle melting anomaly, such as a mantle roll. The deep, hot asthenospheric source coupled with the short melting column, a mantle melting anomaly, and a thicker lithosphere all contribute to the unique location of the NLCVF, and explain why this young volcanic field is small in volume.

Future eruptions can be expected in the next 38-56 ka in the vicinity of Black Rock or the Northern Black Rock Cluster Cones area. Disruption of U.S. Highway 6, and the transportation of medium-level nuclear waste to the Yucca Mountain Nuclear Repository would occur in the event of a future eruption.

TABLE OF CONTENTS

ABSTRACT	iii
LIST OF FIGURES	vii
ACKNOWLEDGEMENTS	ix
CHAPTER 1 INTRODUCTION	1
Regional Geology	2
Death Valley-Lunar Crater Basalt Zone	4
Related Work	6
CHAPTER 2 STRATIGRAPHY AND ERUPTIVE SEQUENCE	11
Oligocene Ignimbrite	12
Tower Road Cones and Basalt Flow	12
Central Flow Basalt	13
Northeast Finger Basalt	13
G-Cone and G-Cone Basalt Flow	14
Huge Cone and Huge Cone Basalt Flow	14
Three Cone and Three Cone Basalt Flow	15
North Black Rock Cluster Cones	16
F-1 Basalt Flow	16
F-2 Basalt Flow	17
F-3 Basalt Flow	17
Black Rock Cone and Black Rock Basalt Flow	17
Table 1 Geochronology	19
Table 2 Cone Radius and Height	20
Table 3 Flow Characteristics	21
Table 4 Petrography	22
Photograph of Bomb	23
Photograph of Flow Characteristics	24
CHAPTER 3 GEOCHEMISTRY	25
Analytical Techniques	25
Geochemistry of Mafic Rocks	26
Major Elements	26
Trace Elements and Isotopes	27
CHAPTER 4 INTERPRETATION	37
Models	37

Observations and Assumptions.....	38
Fractional Melting Model.....	39
Assimilation Fractional Crystallization	40
Fractional Crystallization within Individual Flow	41
Magma Mixing.....	41
Summary	42
Table 5 Distribution Coefficients.....	47
CHAPTER 5 MANTLE MELTING MODEL	48
Introduction.....	48
Methods.....	50
Conclusions.....	51
CHAPTER 6 FUTURE ERUPTIONS.....	56
CHAPTER 7 SUMMARY AND CONCLUSIONS	57
REFERENCES CITED.....	59
APPENDIX A GEOCHEMICAL DATA.....	65
APPENDIX B ISOTOPE DATA.....	70
APPENDIX C PETROGRAPHY	71
APPENDIX D MODEL DATA-FRACTIONAL MELTING.....	77
APPENDIX E SAMPLE LOCATION	79
APPENDIX F GEOCHRONOLOGY	80
APPENDIX G ACCURACY AND PRECISION	90
PLATE 1: Map of Northern Lunar Crater Volcanic Field showing volcanic stratigraphy	in pocket
VITA.....	93

LIST OF FIGURES

Figure 1:	Index Map showing the location of the Northern Lunar Crater Volcanic Field within the Death Valley-Pancake Range Basalt Zone.....	8
Figure 2:	Major and trace element signatures of volcanic fields in the Death Valley-Pancake Range Basalt Zone.....	9
Figure 3:	Classification of Northern Lunar Crater Volcanic Field mafic rocks alkaline vs. subalkaline.....	10
Figure 4:	Classification of Northern Lunar Crater Volcanic Field mafic rocks using LeBas system	29
Figure 5:	Major element Harker variation diagram for rocks in the Northern Lunar Crater Volcanic Field.....	30
Figure 6a:	Ocean Island Basalt-normalized trace element distribution diagram for enriched group of samples in the Northern Lunar Crater Volcanic Field.....	31
Figure 6b:	Ocean Island Basalt-normalized trace element distribution diagram for depleted group of samples in the Northern Lunar Crater Volcanic Field.....	32
Figure 7:	Ocean Island Basalt-normalized trace element distribution diagram for F-1 and F-2 flows	33
Figure 8:	Ce/Yb vs. Rb diagram showing two distinct groups of mafic rocks in the Northern Lunar Crater Volcanic Field.....	34
Figure 9:	Epsilon Nd vs. Sr isotopes for select samples in the Northern Lunar Crater Volcanic Field.....	35
Figure 10:	Pb isotopes for select samples in the Northern Lunar Crater Volcanic Field	36
Figure 11:	Fractional melting model for F-1 basalt flow, with partial melt of residuum.....	43
Figure 12:	Fractional melting model for F-1 basalt flow, with differing degrees of partial melting	44

Figure 13: Fractional crystallization model for F-1 and F-2 flows.....	45
Figure 14: Magma mixing model for F-1 and F-2 flows.....	46
Figure 15: FeO* vs. MgO diagram for mantle melting model calculations	53
Figure 16: Mantle melting model	54
Figure 17: Cartoon representation of mantle roll anomaly theory.....	55

ACKNOWLEDGMENTS

I would like to thank all the staff, faculty and students at the Department of Geoscience at the University of Nevada, Las Vegas. I would also like to thank the Bernada E. French endowment and the Nevada Agency for Nuclear Affairs for the financial support which helped make this project possible. I wish to extend a special thanks to my committee members for their involvement. I would especially like to thank Dr. Gene Smith for the tremendous patience, help and guidance he provided from day one, and for helping me to see the path to success.

This thesis is dedicated to my family; my mom and dad, Richard D. Stickney and Dr. Nancy K. Stickney, who I respect more than anyone: to my husband, Joe D. Mosby, the rock on which can always count on, I cherish you more than words: and to the memory of my uncle Gary Palmer, who's thirst for knowledge was highly contagious and immensely inspirational, you will always live on in my heart, my mind and the G-Cone and G-Cone flow.

CHAPTER 1

INTRODUCTION

The northern Lunar Crater Volcanic Field (NLCVF) is located in the Great Basin in Nevada (Figure 1). It is situated along the axis of the Great Basin and is isolated from the Pliocene-Quaternary mafic volcanic fields of the Sierran Province/Western Great Basin to the west and the transition zone/Colorado Plateau to the east (Yogodzinski et al., 1996). This area provides one of the best examples of Pliocene to Recent cinder cones, maars and alkali basalt lava flows in the United States. The NLCVF is part of a narrow, northeast trending zone of volcanic fields that extends from Death Valley to the south, through Crater Flat, near Yucca Mountain, to the Reville Range and Lunar Crater in the central Pancake Range (Figure 1) (Farmer et al., 1989; Dickson, 1998). This zone was named the Death Valley-Pancake Range Basalt Zone (DV-PRBZ) (Vaniman et al., 1982; Farmer et al., 1989).

The purpose of this thesis is to determine the volcanology and petrogenesis of the NLCVF at the northern end of the DV-PRBZ. The major problems and questions of this project include the determination of (1) the volcanic history of the NLCVF.

This includes the determination of eruptive history, type of eruption, and the complexity of eruption at individual centers. (2) What is the geochemical evolution of the field? Specific questions include the nature of the mantle source and subsequent evolutionary history. (3) What are the reasons for the unique location of the volcanic field? Why does the DV-PRBZ lie along the axis of the Great Basin? What features of the lithosphere or asthenosphere control the isolated location of the NLCVF in the DV-PRBZ? (4) What are volcanic hazards associated with the field? What is the likelihood of future eruptions and the dangers they may pose with special consideration to the transport of nuclear waste along U.S. Highway 6?

Several hypotheses were tested including (1) The location of the NLCVF is due to unique features of the mantle or lithosphere (e.g. an unusually thick or thin lithosphere, an unusually hot mantle, a mantle plume, or mantle anomaly). (2) The volcanic field may be of low volume, but it is complex in its petrogenesis. (3) Future eruptions could threaten U.S. Highway 6, and ultimately the transport of nuclear material to Yucca Mountain.

Regional Geology

Basaltic volcanism occurred in the Great Basin after a shift in the style of tectonics and magmatism related to the intersection of the East Pacific Rise and the Pacific Margin of the North American Plate at ~ 30 Ma (Fitton et al., 1991). This intersection migrated north with time, reaching the latitude of Lunar Crater at ~ 10 Ma (Severinghaus and Atwater, 1990).

Crustal extension occurred before and after this intersection and the structures accommodating extension changed from mainly detachment (before the intersection) to high-angle faulting (after the intersection). This intersection also marks the change in composition of volcanic rocks from bi-modal suite of basalt and rhyolite to predominantly basaltic (Christiansen and Lipman, 1972). During the Cenozoic, the Great Basin experienced uplift by as much as 3 km (Bradshaw, 1991), and over the last 17 Ma the Great Basin underwent crustal thinning. During the past 15 Ma the lithosphere of the Great Basin has thinned, and Cenozoic extension and volcanism were coeval (Eaton, 1982). Uplift may be related to an area of high heat flow, or a mantle plume beneath the Great Basin (Best and Brimhall, 1974; Farmer et al., 1989; Fitton et al., 1991).

The DV-PRBZ is located along the axis of the Great Basin and is characterized by Pliocene to Holocene cinder cones and lava flows (Farmer et al., 1989). Basalts from the southern part of the zone, near Crater Flat, are some of the most isotopically enriched with respect to ocean island basalt (OIB) in the region ($^{87}\text{Sr}/^{86}\text{Sr} \sim 0.707$, $\epsilon_{\text{Nd}} < -8.5$) (Farmer et al., 1989; Livaccari and Perry, 1993), and have major and trace element signatures of rocks derived from the lithospheric mantle (hypersthene-normative with low FeO^* , TiO_2 , Rb/Ba , and Ti/Hf and high La/Ta and Ba/Nb) (Fitton et al., 1988). In contrast, basalts from the northern areas (Reveille Range, Pancake Range) of the DV-PRBZ are isotopically depleted ($^{87}\text{Sr}/^{86}\text{Sr} \sim 0.7035$, $\epsilon_{\text{Nd}} > +3$) (Farmer et al., 1989; Foland and Bergman, 1992) and have major and trace element signatures similar to OIB (nepheline-normative with high FeO^* , TiO_2 , Ti/Hf , and Rb/Ba and low La/Ta and Ba/Nb) (Fitton et al., 1988, 1991; Farmer et al., 1989; Yogodzinski et al., 1996) (Figure 2).

Isotopic data suggest that some of the youngest basalts in the northern DV-PRBZ were derived from currently upwelling asthenosphere (Foland et al., 1987). Isotopic signatures from eastern Death Valley, and much of the Nevada Test Site, Crater Flat, and vicinity suggest that crustal contamination has influenced basalt geochemistry more in this area than in others (Farmer et al., 1989).

Death Valley-Lunar Crater Basalt Zone

The Southern Nevada Volcanic field is located in the southern part of the DV-PRBZ, and is composed mainly of rhyolite ash-flow tuffs, rhyolite domes and andesite to dacite lava flows and domes which erupted between ~11 and 8 Ma (Byers et al., 1976; Christiansen et al., 1977). This initial event was followed by basaltic volcanism that occurred over the past 11.2 m.y. (Wells et al., 1990). Five Quaternary volcanic centers are present at Crater Flat which is bounded on its eastern side by Yucca Mountain (Wells et al., 1990; Bradshaw and Smith, 1994). Small volume cinder cones in Crater Flat were active from ~3.7 to 1 Ma (Bradshaw and Smith, 1994). The authors identified polycyclic and polygenetic volcanism in the Crater Flat area, indicating a magmatic plumbing system link between the two main centers of Black and Red cones, and suggested that volcanic activity in the vicinity of Crater Flat occurred at a number of sites across the magmatic feeder zone during a single eruptive phase. Bradshaw and Smith (1994) stated that this could have significant implications for volcanic hazard assessment in the vicinity of Yucca Mountain, and that the complexity of the area points to a high likelihood of future eruptions.

The Reveille Range is located in the north central part of the DV-PRBZ (Figure 1). Naumann et al. (1991) reported three episodes of volcanism in the Reveille Range; two episodes of basaltic volcanism (5.9 to 5.0 Ma and 4.6 to 3.0 Ma) were separated by an eruption of trachytic lavas and pyroclastic units.

Work in the Reveille Range on Pliocene age mafic rocks by Yogodzinski et al. (1996) indicate that incompatible element signatures from samples show an asthenospheric mantle source with three identified eruptive episodes linked to separate melting events in the mantle. Furthermore, the authors determined that the geochemical variations found were due to contamination of the basalt by older carbonate rocks.

Volcanism in the NLCVF occurred during the late Quaternary (Scott and Trask, 1971). The Black Rock flow in the northern part of the LCVF was dated at 38.1 ± 9.7 ka (K/Ar), and the Lunar Crater flow at 600 ka (Shepard et al., 1995). A more recent $^{40}\text{Ar}/^{39}\text{Ar}$ age for the Black Rock flow is 20 ± 9 ka (Dickson, 1998). The lava flows and cinder cones of the LCVF are mainly alkali basalt (Figure 3) (tephrite basanites, trachy-basalts and basalts). The presence of an OIB-type incompatible element signature in Pleistocene age basalts of the LCVF indicates that the mantle source of mafic volcanism in this part of central Nevada has remained largely unchanged for the past 5 to 6 Ma (Yogodzinski et al., 1996). Dickson (1998) determined that a transition from a lithospheric mantle source to an asthenospheric mantle source occurred between 21.79 Ma and 3.82 Ma after the major phase of Tertiary extension. Furthermore, work by Dickson (1998) on Citadel Mountain in the southern LCVF concluded that the area represents a simple magmatic system. Fractional crystallization and magma commingling/mixing may explain compositional diversity.

Studies on xenoliths in the northern areas of the DV-PRBZ (Lum et al., 1989) concluded that no lower crustal xenoliths occur in the LCVF, this implies that basaltic magma ascended rapidly from mantle depths, precluding significant crustal contamination. Mantle derived dunite and harzburgite xenoliths, along with amphibole megacrysts, also provide evidence that basalt magma was stored near the crust-mantle boundary and was erupted rapidly without significant crustal interaction (Yogodzinski et al., 1996).

Related Work

Previous work in the Great Basin on young basaltic fields is mainly restricted to relationships of basalt fields to regional tectonics and the morphometry of cinder cones. Studies that focus on the volcanology and geochemistry of these volcanic fields are rare.

Hoffer (1976) explored the stratigraphy of the Potrillo Basalt Field in south central New Mexico and examined the link of the development of young basalts and regional tectonics. Connor (1994) studied cycles of reoccurring volcanism in the Springerville Volcanic Field, Arizona. The Springerville Volcanic Field (2.0 to 0.3 Ma) contains 405 alkali basalt vents, covers 3000 sq. km, and is the third largest late Pliocene to Quaternary volcanic field in the United States (Condit et al., 1989). Dohrenwend et al. (1986) studied geomorphologic changes to Quaternary cinder cones in the Cima Volcanic Field of California. The authors developed an empirical model of the degradation of the cinder cones due to the arid climate of the Mojave Desert.

Downing et al. (2000) utilized basalt geochemistry, geochronology and Geographic Information Systems (GIS) to image the mantle beneath the Colorado Plateau-Basin and Range transition zone in southwestern Utah.

Using inverse distance weighted (IDW) surfaces in ArcView GIS, Downing et al. (2000) suggested that a boundary between the lithospheric and asthenospheric mantle source for alkali basalt magma formed during Tertiary extension but its position was controlled by an older (perhaps Precambrian) lithospheric boundary. Downing et al. (2000) found islands of high or low element concentration interrupting the gently sloping IDW surface and suggested that these islands may reflect interlayering of Basin and Range and Colorado Plateau mantle types or differing depths of magma generation.

Work by Smith et al. (1999) on the Hurricane Volcanic Field in Southern Utah examined chemical variability of the lithospheric mantle. The Hurricane Volcanic Field is a group of late Quaternary alkali basalt flows and cinder cones in the Colorado Plateau, Basin and Range transition zone (Smith et al., 1999). This study noted that all but two of the cone clusters had a different parent magma and evolved by fractional crystallization of different amounts and proportions of olivine and clinopyroxene, and that the parent magmas formed by 0.5 to 7% partial melting of lithospheric mantle (fertile lherzolite). The authors suggested that the melting of a heterogeneous lithospheric mantle is the most reasonable mechanism for production of chemical variability across the transition zone and may reflect a major lithospheric boundary that represents a structural and physiographic boundary between the Colorado Plateau and Basin and Range.

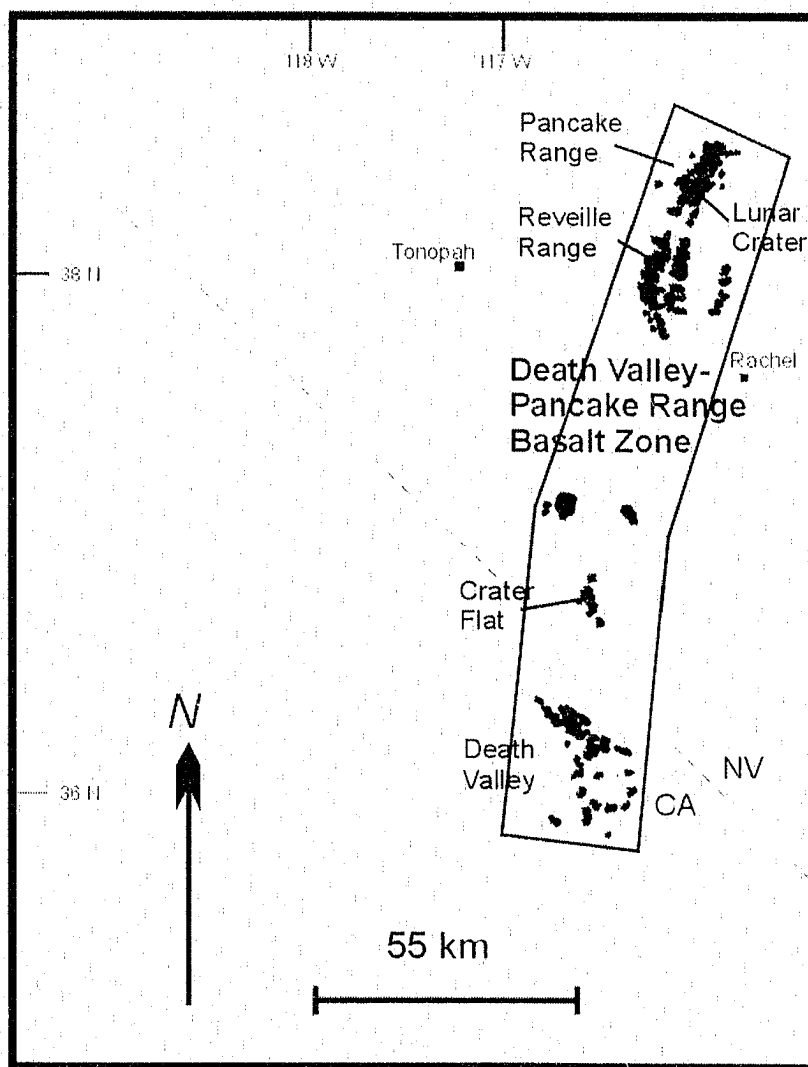


Figure 1: Map detailing the location of the Northern Lunar Crater Volcanic Field. Box represents the Death Valley-Pancake Range Basalt Zone. Mafic volcanic zones (< 8 Ma) are shown in black. Modified from Yogodzinski et al. (1996).

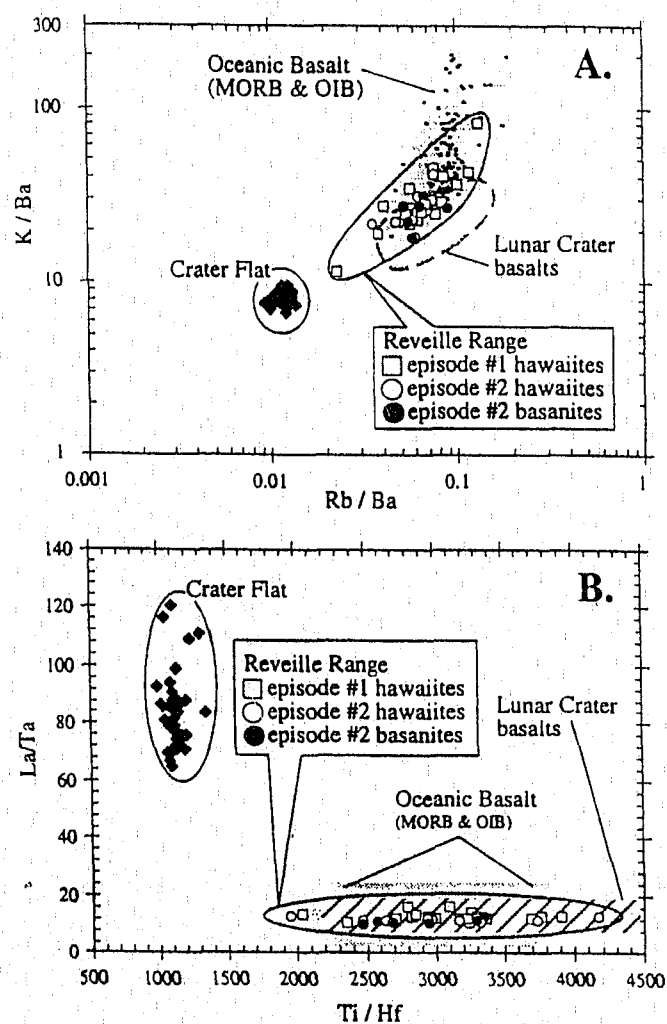


Figure 2: Incompatible element ratio-ratio plots comparing Pliocene Reville Range basalts to Pleistocene basalts from Crater Flat and the Lunar Crater Volcanic Field (from Yogodzinski et al., 1996).

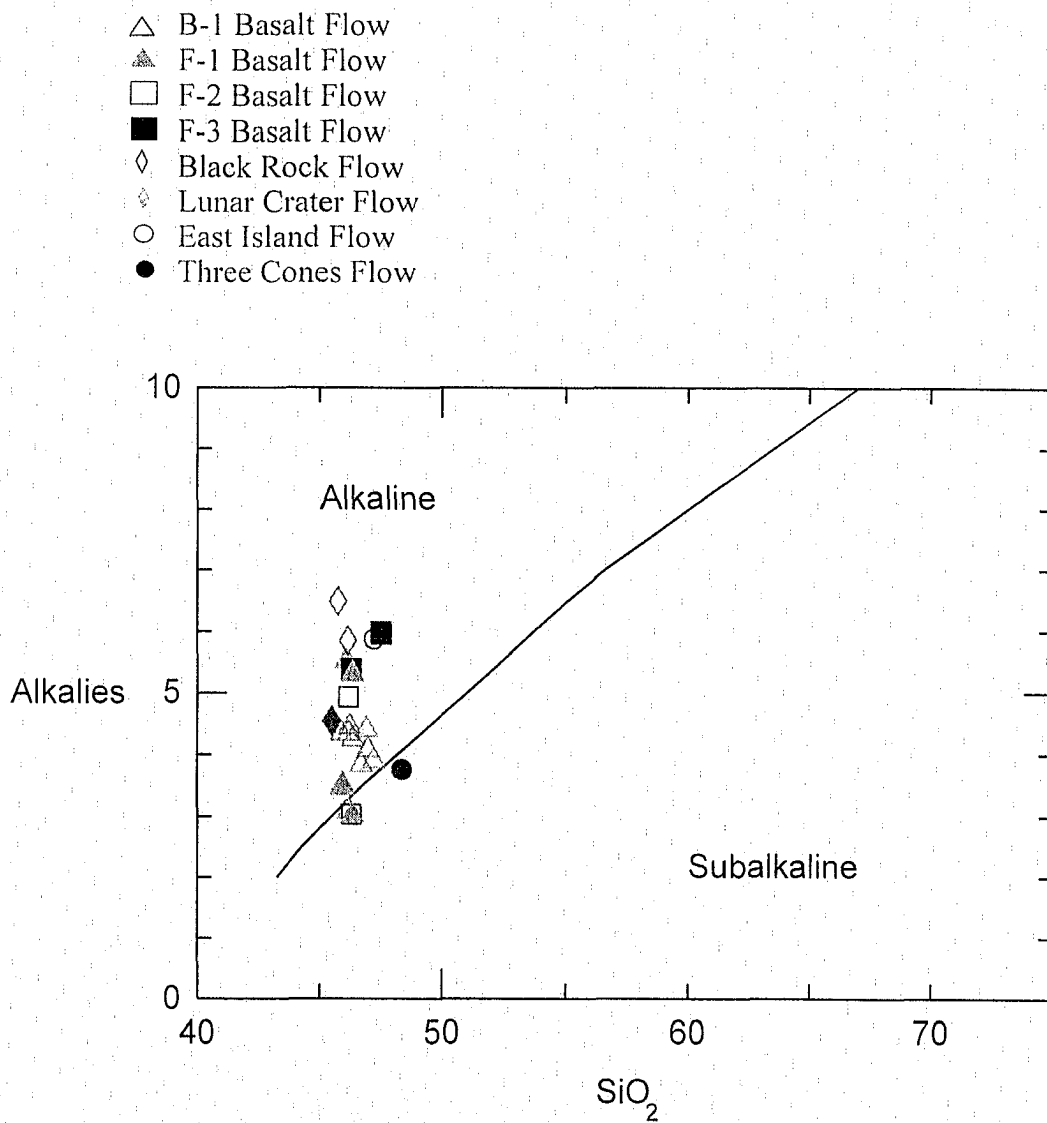


Figure 3: Classification of NLCVF mafic rocks alkalis diagram ($\text{Na}_2\text{O} + \text{K}_2\text{O}$ vs. SiO_2). The majority of samples are alkaline. Basalts from Three Cones, the interior of F-1 and edge of F-2 are marginally subalkaline.

CHAPTER 2

STRATIGRAPHY AND ERUPTIVE SEQUENCE

The volcanic stratigraphy and eruptive sequence of the NLCVF were developed using field observations and geochronology. Fieldwork, study of aerial photographs and satellite imagery provided detailed information as to the relative age of flows and cinder cones. Mineralogical and physical characteristics of the flows helped to group related flows and determine relative age. Geochemistry (see Chapter 3) and petrography (Appendix C; Table 4) were used to test field relationships. Geochronologic data important for determining eruptive sequence include four new $^{40}\text{Ar}/^{39}\text{Ar}$ dates (Table 1) as well as dates obtained from the previous work of Evernden et al. (1964), Dohrenwend et al. (1987), Kargel (1987), Foland and Bergman (1992), Shepard et al. (1995), and Dickson (1998).

A majority of cones and flows were previously unnamed, and where appropriate, names and locations are designated in the stratigraphic descriptions contained in this chapter. Cones and flows are described below from oldest to youngest. Stratigraphic details are summarized in Table 3. This work focused on the flows north of U.S. Highway 6. Previous work by Scott (1969), Scott and Trask (1971) and Dickson (1998) provided detailed descriptions of flows, cones and maars in the southern section of the Lunar Crater Volcanic Field.

Mineralogy described in this section is for hand sample only, as observed in the field. Petrographic information from thin sections is summarized in Appendix C and Table 4.

Oligocene Ignimbrite

The underlying rock, the Stone Canyon-Windous Butte Formation, is a rhyolitic to andesitic crystal vitric to vitric welded and nonwelded ash-flow tuff with minor air-fall tuffs and water-laid sedimentary rocks (Scott and Trask, 1971). This formation crops out in the east-central to north-central section of the field area (Plate 1). K-Ar dating by Evernden et al. (1964) indicate that tuffs of this formation erupted at 32.8 Ma.

Tower Road Cones and Basalt Flow

Located in the northeastern most section of the field area are a group of cinder cones and flows that crop out along the road to a group of microwave towers. These cones and flows are herein known as the Tower Road Cones and basalt flow (Plate 1). The Tower Road cinder cones and blocky to A'a flows directly overlie basement tuff. The three northernmost cinder cones are comprised of ash and lapilli sized red and black scoria, and welded agglutinated scoria containing cow-dung bombs and aerodynamically-sculpted ribbon bombs. The largest of the three cones is herein named Horseshoe Cone (see Table 2). The Tower Road basalt flow erupted from Horseshoe Cone and the two smaller cones and flowed 1.5 to 2 km south to southeast. The flows range in thickness from 0.5 to 3 meters.

The Tower Road basalt contains small, 1 to 3 mm olivine phenocrysts, anorthoclase phenocrysts and peridotite xenoliths. The flow is characterized by massive basalt overlain by highly vesiculated lava. Vesicles are elongated in the plane of flow. East of Tower Road the basalt displays columnar jointing. West of Tower Road, the flows have steep flow fronts and flowed down a pre-existing wash (Plate 1). In another locality, the flow cascaded through a gap between two basement tuff spires.

Central Flow Basalt

Located along U.S. Highway 6, in the central part of the field area, is a basalt flow hereafter referred to as the Central Flow basalt (Plate 1). The Central Flow basalt is approximately 6.5 km in length, oriented northeast and marked by gentle slopes of blocky, highly weathered basaltic lava. This flow ranges in thickness from 1 to 4 meters. The Central flow erupted at 3.1 ± 0.4 Ma (Table 1), and its source could not be determined. In hand sample the Central flow contains hornblende phenocrysts up to 1 cm, sparse anorthoclase phenocrysts up to 0.5 cm, and olivine phenocrysts up to 0.005 cm in size. In hand sample, greater than 60% of the olivine has been altered to iddingsite. Rare xenoliths of tuff occur in this flow. Alluvium and vegetation cover the majority of the flow.

Northeast Finger Basalt

In the east-central section of the field area, along U.S. Highway 6, is a linear flow hereafter named the Northeast Finger basalt flow (Plate 1).

The Northeast Finger flow (1.22 ± 0.2 Ma; Table 1) is approximately 6.3 km in length, oriented east-west and marked by very steep (greater than 40°) flow fronts of blocky A'a lava with some columnar jointing. Thickness of this flow ranges from approximately 2 to 20 meters. The source of the flow could not be identified. In hand sample, the flow contains large hornblende phenocrysts up to 1 cm in size, 3 mm spinel phenocrysts, rafted xenoliths of tuff 10.0 cm average size, and xenoliths of dunite.

G-Cone and G-Cone Basalt Flow

South of Huge Cone (described below) is a cone and flow herein named G-Cone and G-Cone basalt flow (Plate 1). The G-Cone is a large cinder cone with a diameter of 1037 meters and a height of 94 meters (Table 2). This cone is comprised of ash and lapilli sized red and black scoria, with some welded agglutinate. A breach on the east side of the cone exposes bedded lapilli and ash. Large bombs (30 cm in diameter) of agglutinate and basaltic scoria are found around the base of G-Cone. The blocky G-Cone basalt flowed about 1 km in a north, northeastward direction and has a flow front approximately 1.5 meters in height. In hand sample, the G-Cone basalt contains olivine phenocrysts (3 mm), with some anorthoclase phenocrysts up to 1 cm in size. Some scattered peridotite and dunite xenoliths are also present.

Huge Cone and Huge Cone Basalt Flow

The cone and associated flow located in the northernmost section of the field area, west of Horseshoe Cone is hereafter named Huge Cone and the Huge Cone basalt flow (Plate 1). Huge Cone is 193 meters in height and 1951 meters in diameter (Table 2).

Second in size to Black Rock Cone, this is the largest cinder cone in the northern part of the field area. At Huge Cone, both a debris apron and debris ring is clearly seen. These geomorphic features are produced by the accumulation of lapilli and ash at the base of the cone. The preservation of the debris ring and the overlap of the cone onto Horseshoe Cone indicate that Huge Cone is the younger of the two. Two smaller cones north of Huge Cone partially cover the cinder cone and are therefore younger than Huge Cone. The Huge Cone basalt is up to 1.5 meters in thickness and flowed from the base of the cone 1 km to the north. This blocky basalt flow has anorthoclase phenocrysts up to 1 cm in size, and a large (35%) amount of olivine phenocrysts 1 to 6 mm in size. Xenoliths of lherzolite and dunite are also present.

Three Cones and Three Cones Basalt Flow

Three Cones and their basalt flows (named in this study) are in the central region of the field north of U.S. Highway 6 (Plate 1). This group is the most geochemically evolved group in the NLCVF (See Chapter 3). The cones range in height from 69 to 100 meters and in diameter from 305 to 793 meters (Table 2). The cones consist of ash and lapilli sized material, mostly red in color. Bombs (10 to 30 cm in size) of welded agglutinate and basalt are found on and around the Three Cones cluster. The Three Cone flow is a blocky A'a flow that extends 1.8 km to the west of the cone cluster and ranges from 0.5 to 3 meters in thickness. The flow contains sparse anorthoclase phenocrysts up to 1 cm in size, and rare olivine phenocrysts. In hand specimen, the basalt flow has a very fine-grained matrix with <15% total phenocrysts.

North Black Rock Cluster Cones

A N. 25 E. aligned group of five cinder cones is herein named the North Black Rock Cluster Cones A-E (NBRCC) (Plate 1). Three basalt flows erupted from this group. They are named (from oldest to youngest) F-1, F-2 and F-3. The North Black Rock Cluster Cones range in height from 109 to 141 meters and vary from 976 to 1646 meters in diameter (Table 2). The basalt flow from these overlapping, clustered cones contain anorthoclase from 2 to 5 cm, hornblende up to 1.5 cm, and olivine up to 1 cm. This group of cones (A-E) has similar mineralogical compositions of ash and lapilli sized material. All cones are breached westward, and cones C-D have sections of bedded ash and lapilli exposed in the breach.

F-1 Basalt Flow

The blocky F-1 basalt flow extends 3 to 3.8 km west of the cones and ranges in thickness from 0.5 to 5 meters (Plate 1). An $^{40}\text{Ar}/^{39}\text{Ar}$ date for the F-1 basalt is 1.2 ± 0.6 Ma (Table 1). In hand sample, the F-1 basalt contains large olivine phenocrysts up to 5 cm in size and spinel phenocrysts up to 4 mm in size. Concentrations of rafted tuff occur along the margins of the F-1 flow. F-1 basalt is mainly scoriaceous but columnar jointing can be found near the central north margin of this flow. F-1 also contains elongated vesicles, which decrease in abundance near the base of the flow. The surface of the F-1 flow is characterized by approximately 200 tumuli (Walker, 1991), where underlying lava has caused swelling of the hardened crust of lava producing large bubbles. Almost all tumuli in the F-1 flow are hollow shells as all the lava which caused the initial formation of the structure was extruded outward, leaving the bubble wall partially intact. These tumuli are up to 3 m high and 10 m wide.

F-2 Basalt Flow

F-2 directly overlies F-1, and flowed about 2 km to the west of the North Black Rock Cluster Cones (Plate 1). This A'a flow is mostly blocky. Thickness of this flow is estimated to be 1 to 3 meters. F-2 is most easily distinguished by the presence of highly altered olivine (4 mm in size) where olivine is 60% iddingsite with an olivine core. This flow contains anorthoclase phenocrysts up to 1 cm in size, with some pieces of rafted tuff present. F-2 is more massive at the base, and vesiculated at the top, similar to F-1.

F-3 Basalt Flow

F-3 directly overlies F-2 (Plate 1). It is much smaller in area and volume than F-1 and F-2, flowing only about 1 km westward from the North Black Rock Cluster Cones. It has an average thickness of 2 meters. F-3 is composed of fresh blocky basalt containing olivine phenocrysts up to 4 cm, hornblende up to 1 cm and some anorthoclase phenocrysts up to 1 cm in size. An $^{40}\text{Ar}/^{39}\text{Ar}$ date for F-3 is 240 ± 340 ka (Table 1). Near the flow margin, lava is highly vesiculated and most of the vesicles are filled with carbonate. F-3 is covered by desert pavement with a light to moderate amount of desert varnish.

Black Rock Cone and Black Rock Basalt Flow

The Black Rock Cone is the largest cone in the NLCVF with a height of 242 meters and diameter of 1402 meters (Table 2). The cone consists of black ash and lapilli sized material. Black Rock Cone is deeply breached to the west with thick (0.5 m) bedding clearly visible in the crater wall.

Black Rock flow is the freshest lava flow in the NLCVF and is composed of black blocky A'a lava with steep (up to 45°) flow fronts. It flowed approximately 3 km west from Black Rock Cone and ranges from 4 to 10 meters in thickness. As the basalts were extruded, they were deflected around the base of a large cinder cone to form two coalescing lobes on the valley floor (Scott, 1969). Large sections (up to 3.5 m) of autobreccia are present. Autobreccia is not found in any of the other flows in the NLCVF (Scott, 1969). Over 100 breadcrust bombs up to 1.5 m in size were found on the west side of Black Rock Cinder Cone. Near the central depression on the east side of the breached cone, a bocca (Sigurdsson et al., 2000) was identified, and sections of rafted cone were noted on the flow near the cone. Shepard et al. (1995) obtained ^{36}Cl and ^{10}Be dates for Black Rock Flow of 38.1 ± 9.7 ka and Dickson (1998) obtained a $^{40}\text{Ar}/^{39}\text{Ar}$ date of 20 ± 9 ka. This flow contains large anorthoclase phenocrysts up to 3 cm in size, olivine up to 0.5 cm in size, and hornblende up to 1 cm in size. The Black Rock flow also contains xenoliths of lherzolite up to 5 cm and dunite up to 3 cm in size.

Table 1: Summary of $^{40}\text{Ar}/^{39}\text{Ar}$ Geochronology from this study.

<i>BASALT FLOW</i>	<i>AGE $\pm 1\sigma$</i>
Central	$3.10 \pm 0.4 \text{ Ma}$
Northeast Finger	$1.22 \pm 0.2 \text{ Ma}$
F-1	$1.20 \pm 0.6 \text{ Ma}$
F-3	$240 \pm 340 \text{ ka}$

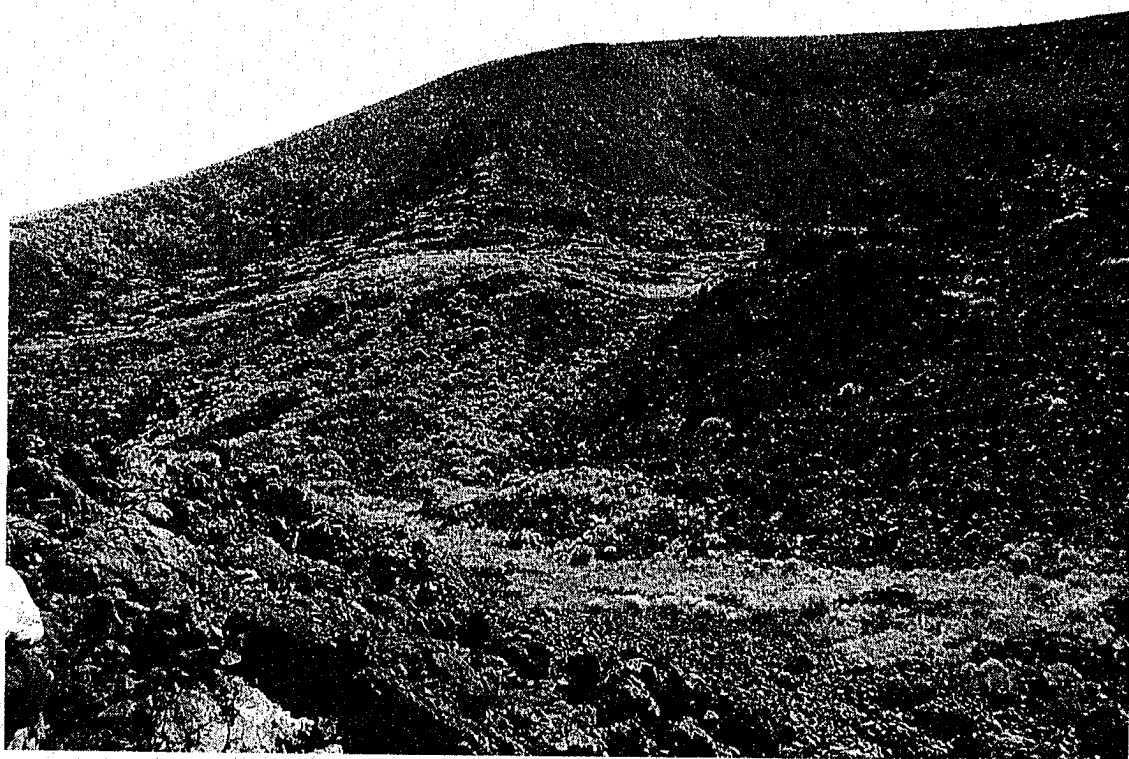
Table 2: Cone Diameter and Height of Flows North of U.S. Highway 6		
<i>Cone Name</i>	<i>Height (m)</i>	<i>Mean Diameter (m)</i>
Huge	193	1951
Horseshoe	123	1280
Dual Cluster	47	549
Tower Road	56	671
G	94	1037
Island A	41	366
Island B	26	244
Island C	24	244
Island D	75	549
Desolate	66	1159
Camp A	99	732
Camp B	98	793
Camp C	31	427
Black Rock	242	1402
Older	73	610
Three A	97	793
Three B	69	305
Three C	100	671
N Cluster A	114	976
N Cluster B	123	1341
N Cluster C	109	1220
N Cluster D	141	1646
N Cluster E	110	1280

Table 3: Distinguishing Characteristics of Basaltic Flows North of U.S. Highway 6						
<i>Flow</i>	<i>Extent (km)</i>	<i>Flow Direction</i>	<i>Thickness (m)</i>	<i>Xenoliths/Rafted Material</i>	<i>Flow type</i>	<i>Notable Characteristics</i>
Tower Road	1.5 - 2.0	S-SE	0.5-3.0	Ultramafic	Blocky, A'a	1.0-3.0mm ol. anorth
Central	6.5	NE-SW	1.0-4.0	Rafted Tuff	Blocky	1.0cm hrn. 0.5 cm anorth, olv. highly weathered/alterd
NE Finger	6.3	E-W	2.0-20.0	Dunite, Rafted Tuff	Blocky, A'a	1.0cm hrn. 3.0mm spinel, steep flow fronts
G-Cone	1.0	N-NW	1.5	Peridotite, Dunite	Blocky	3.0mm ol. 1.0cm anorth
Huge Cone	1.0	N	1.5	Lherzolite, Dunite	Blocky	35% 1.0-6.0mm olv. 1.0cm anorth
3-Cones	1.8	W	0.5-3.0	None noted	Blocky, A'a	20% pheno. 1.0cm anorth sparce. rare ol
F-1	3.0-3.8	W	0.5-5.0	Rafted Tuff	Blocky	5.0cm ol. 4.0mm spinel, mod-heavy desert varnish, tumuli
F-2	2.0	W	1.0-3.0	Rafted Tuff	Blocky, A'a	1.0cm anorth, highly altered ol, heavy desert varnish
F-3	1.0	W	2.0	None noted	Blocky	4.0cm ol. 1.0cm hrn. 1.0cm anorth, light-mod desert pavement
Black Rock	3.0	W	4.0-10.0	Lherzolite, Dunite	Blocky, A'a	3.0cm anorth, 0.5cm ol, 1.0cm hrn, autobreccia

Table 4: Petrographic Characteristics of the Northern Lunar Crater Volcanic Field							
<i>Basalt Flow</i>	<i>Total % Phenocrysts</i>	<i>Plagioclase %</i>	<i>Olivine %</i>	<i>Clinopyroxene %</i>	<i>Ilmenite %</i>	<i>Xenocrysts Xenoliths</i>	<i>Distinguishing Characteristics</i>
F-3	30	63	20	15	2	Anorthoclase	Fine Grained, Moderate % Phenocrysts
NE Finger	25	66	15	10	9	Anorthoclase	Coarse Grained, High % Ilm
Central	40	82	10	5	3	Olivine	Larger Phenocryst Size, Moderate % Ilm
Tower Road	50	72	20	5	3	None	Large Size and % Phenocrysts
Huge Cone	30	54	35	10	<1	Gabbro	Large Size Ol, Small % Ilm
F-2	25	56	3	40	1	None	Coarse Grained, Small Size Plag, Moderate Size Cpx, Small % Ol
F-1	30	68	30	0	2	None	Larger Sized Ilm, Plag and Ol, Absence of Cpx
Black Rock	10	68	10	20	2	Clinopyroxene	Very Fine Grained, Few Phenocrysts
3-Cones	20	74	5	15	6	Anorthoclase	Large Amount Ilm, Alteration of Grains, Exsolution Lamellae in Anorthoclase



Photograph showing the massive size of breadcrust bombs found in the Northern Lunar Crater Volcanic Field. This bomb is located to the east of Black Rock Cone.



Photograph showing features of Black Rock basalt flow. Note the fresh, black A'a lava, breach in cinder cone, and basalt flow paths.

CHAPTER 3

GEOCHEMISTRY

Analytical Techniques

Thirty-two samples were selected to best represent the various flows present in the field, provide a good spatial representation of data, and help understand chemical changes across individual flows. Samples were hand chipped and cleaned in the field, and locations were noted using a Trimble GeoExplorer II hand held GPS unit.

Samples for geochemistry were crushed to 1 cm with a Bico Chipmunk crusher and were then ground to 200-mesh powder in a Bico Shatter Box. Fused glass 1:5 (1 part sample to 5 parts flux) disks for X-ray fluorescence analysis (XRF) were prepared using $1.70 \text{ g} \pm 0.0002 \text{ g}$ of prepared powdered rock, $8.50 \text{ g} \pm 0.0002 \text{ g}$ of $\text{Li}_2\text{B}_4\text{O}_7$ and $0.2740 \pm 0.0002 \text{ g}$ NH_4NO_3 . Samples were heated in an 1100°C oven for 30 minutes in Au-Pt crucibles. After 30 minutes the molten sample was poured into an Au-Pt mold and left to cool. Samples were labeled, put in manila envelopes and placed in a dessicator until use.

Major and trace element (Zr, Ba, Nb, Y, Rb, Sr, Cr and Ni) analyses were performed on these disks using the Rigaku 3030 XRF at the University of Nevada, Las Vegas (Appendix A). Other trace elements (La, Ce, Pr, Nd, Sm, Eu, Gd, Tb, Dy, Ho, Er, Tm, Yb, Lu, Th, Hf, Ta, U, Pb, Cs, Ba, Nb, Y, Rb, Sr, Zr, W and Sc) were analyzed using an Inductively Coupled Plasma-Mass Spectrometer (ICP-MS) at Washington State University's Geoanalytical Laboratory (Appendix A).

Sr, Nd and Pb isotopic analyses were performed at the Isotope Geochemistry Laboratory at the University of Kansas (Appendix B). All precision and accuracy data for analyses are listed in Appendix G.

Geochemistry of Mafic Rocks

Major Elements

Most of the basalts in the NLCVF are alkaline, however basalt from Three Cones, one sample from the interior of F-1 and one sample from the edge of F-2 are marginally subalkaline (Figure 3). Using the LaBas et al. (1986) classification, rocks in the NLCVF are tephrite basanite, trachy-basalt and basalt (Figure 4). SiO_2 concentration ranges from 45.48 (Lunar Crater Flow) to 48.36 (Three Cones Flow). Magnesium numbers for the field range from 49 (Central Flow) to 58 (Huge Cone). Basalts in equilibrium with mantle olivine compositions have Magnesium numbers ranging from 68 to 75 for basalts (Wilson, 1989); therefore, the basalts in the NLCVF are moderately evolved.

Harker variation diagrams (Figure 5) show that P_2O_5 and TiO_2 vary little with increasing SiO_2 (P_2O_5 0.40 to 0.84 wt. % and TiO_2 2.30 to 2.88 wt. %) with MgO showing the largest variation with values ranging from 6.99 to 11.05 wt. %. Al_2O_3 and Na_2O concentrations range from 13.29 to 16.18 wt. % and 2.20 to 4.47 wt. % respectively, with Al_2O_3 as the only major element that increases in abundance with increasing SiO_2 . Other elements show little change with increasing SiO_2 . For example, K_2O ranges from 0.80 to 2.10 wt. %, CaO varies from 8.43 to 10.16 wt. % and FeO^* from 11.81 to 14.52 wt. %.

Trace Elements and Isotopes

Two magma groups are distinguishable using element distribution diagrams normalized to OIB (Figures 6a and 6b). Simply stated the enriched group shows a small enrichment in most trace elements relative to OIB (Figure 6a), and the depleted group is depleted in most trace elements relative to OIB (Figure 6b). Each group contains a range of compositions. Both groups show notable peaks at Ba, Nb and Nd with a Pb trough more pronounced in the depleted group. Northeast Finger basalt flow shows enrichment in Cs, but all other trace element values of this sample more closely correlate with the depleted group (Figure 6b). Flows F-1 and F-2 contain samples from both the depleted and enriched groups (Figure 7).

A plot of Ce/Yb vs. Rb (Figure 8) better distinguishes the two magma groups. The enriched group is high in Rb and Ce/Yb and the depleted group is low in Rb and Ce/Yb. The enriched group consists primarily of the Black Rock, F-3 and East Island flows and has a range of Rb values from 41 to 51.6 ppm. The depleted group contains the Lunar Crater, Three Cones, Central, Tower Road and Huge Cone flows with Rb values of 12.4 to 24.7 ppm. Samples from the F-1 and F-2 flows span a wide range of trace element values and plot in both the enriched and depleted groups. For example, the Rb values for the F-1 Flow range from 10.5 to 42.9 ppm and Rb values for the F-2 Flow from 12 to 32.6 ppm.

Samples of the enriched group have ϵ_{Nd} values that range from +4.97 to +5.56 and age corrected $^{87}Sr/^{86}Sr$ between 0.703355 and 0.703721; $^{207}Pb/^{204}Pb$ range between 15.584 and 15.702 (Figures 9 and 10).

Samples of the depleted group have ϵ_{Nd} values that range from +4.97 to +5.50 and age corrected $^{87}\text{Sr}/^{86}\text{Sr}$ between 0.703274 and 0.703535; $^{207}\text{Pb}/^{204}\text{Pb}$ range between 15.548 and 15.616 (Figures 9 and 10). Isotope values for both the depleted and enriched groups are very similar with noticeable overlaps (Figures 9 and 10).

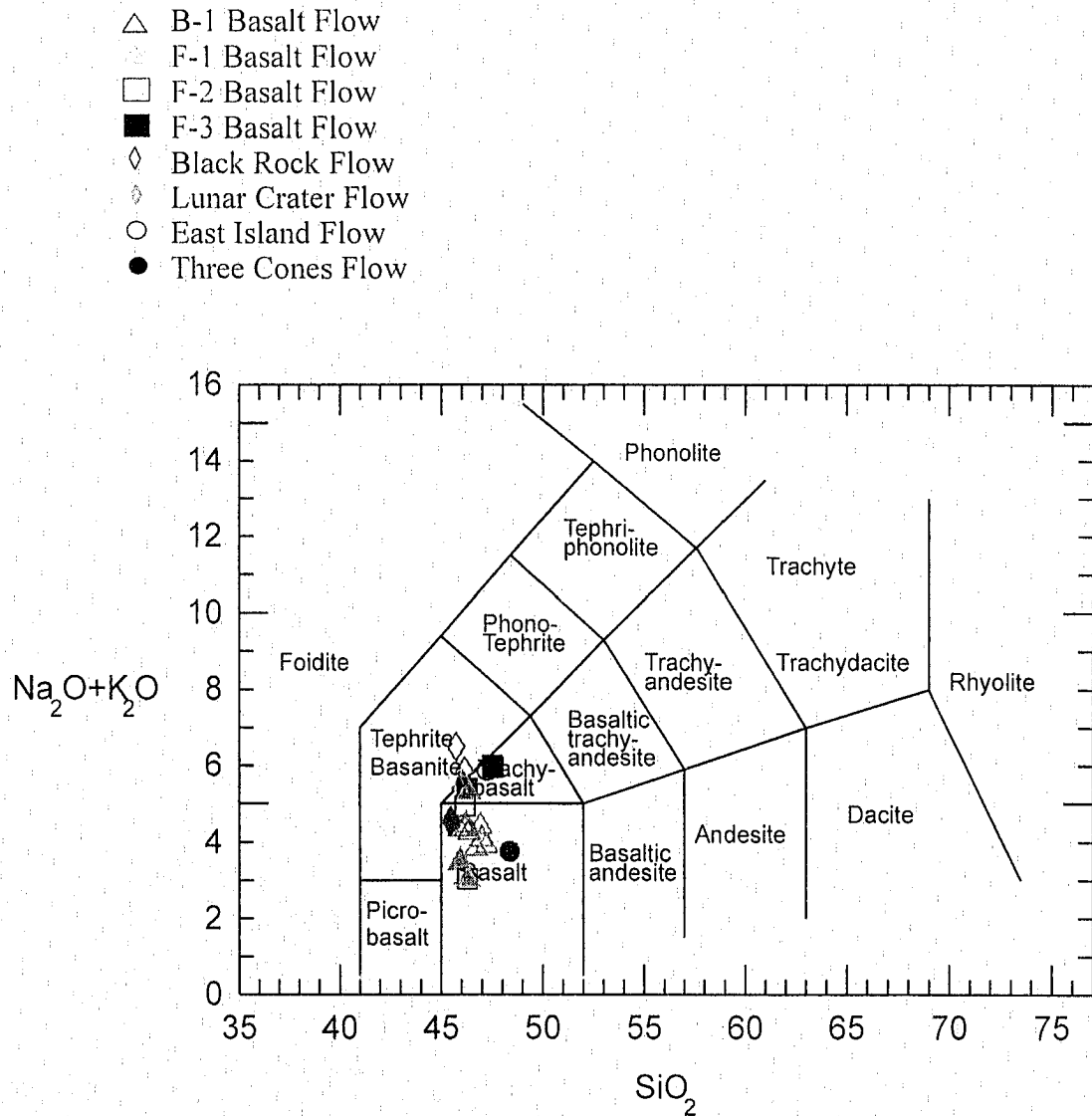


Figure 4: Classification of NLCVF mafic rocks using the LeBas (1986) classification system. Samples are tephrite basanite, trachy-basalt, and basalt.

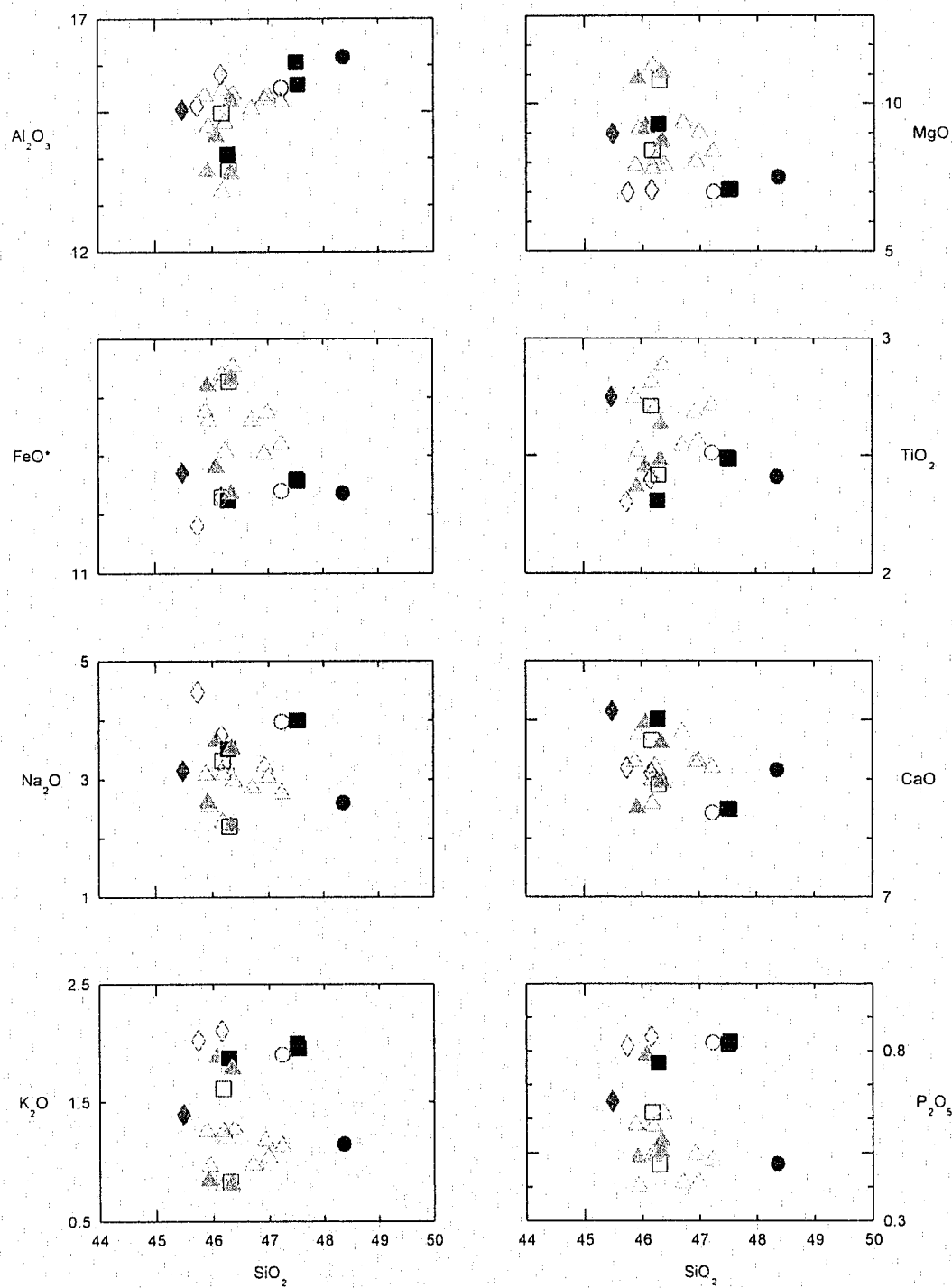


Figure 5: Major element Harker variation diagram for samples in the Northern Lunar Crater Volcanic Field. Symbols are defined in Figure 4.

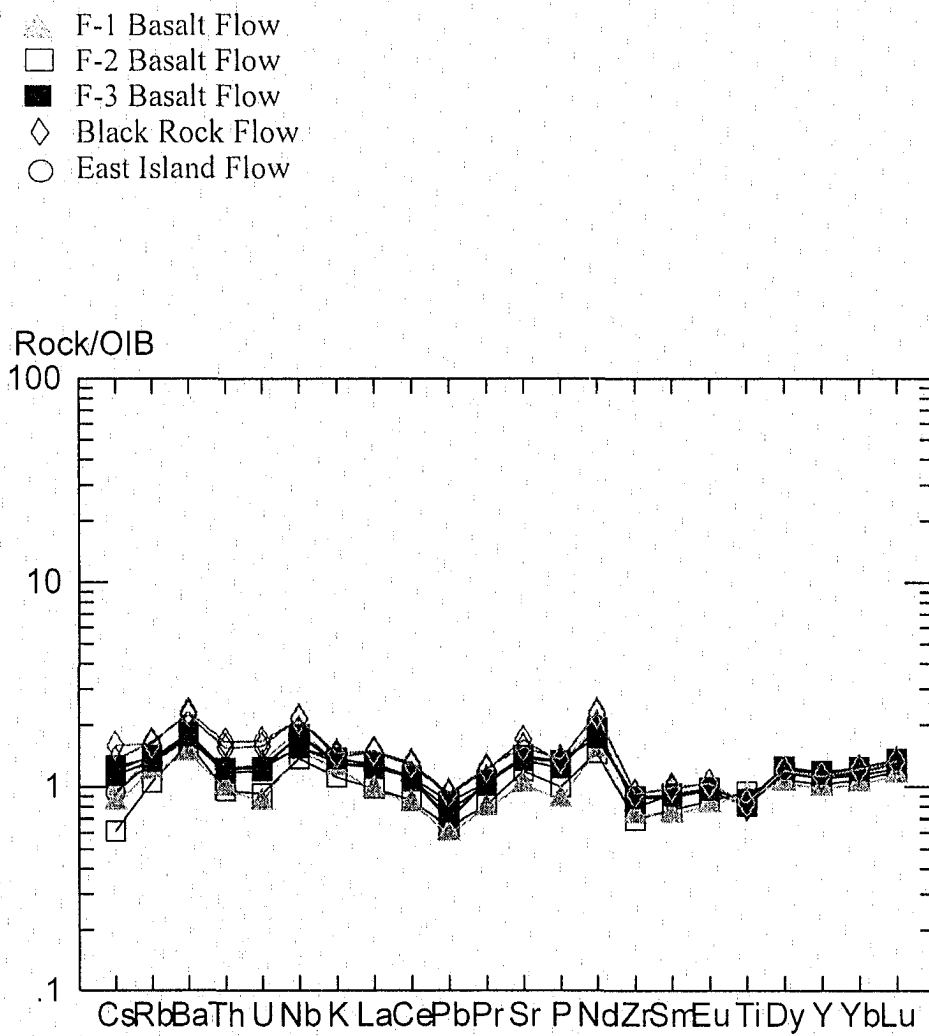


Figure 6a: OIB-normalized (Sun and McDonough, 1989) trace element distribution diagram for enriched group of samples from the NLCVF.

- △ B-1 Basalt Flow
- △ F-1 Basalt Flow
- F-2 Basalt Flow
- ◇ Lunar Crater Flow
- Three Cones Flow

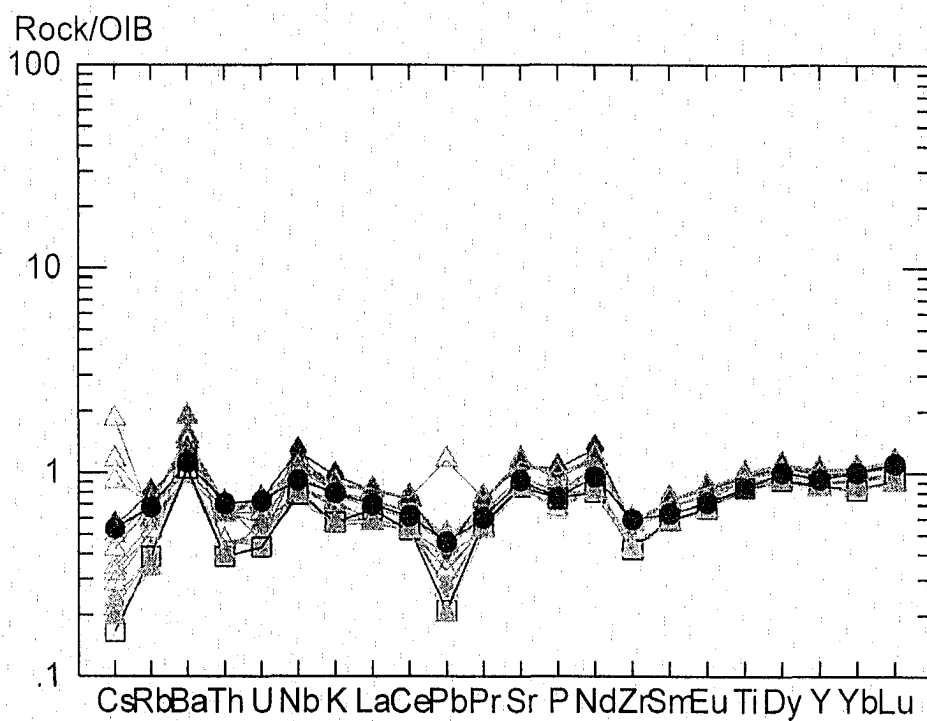


Figure 6b: OIB-normalized (Sun and McDonough, 1989) trace element distribution diagram for depleted group of samples in the NLCVF.

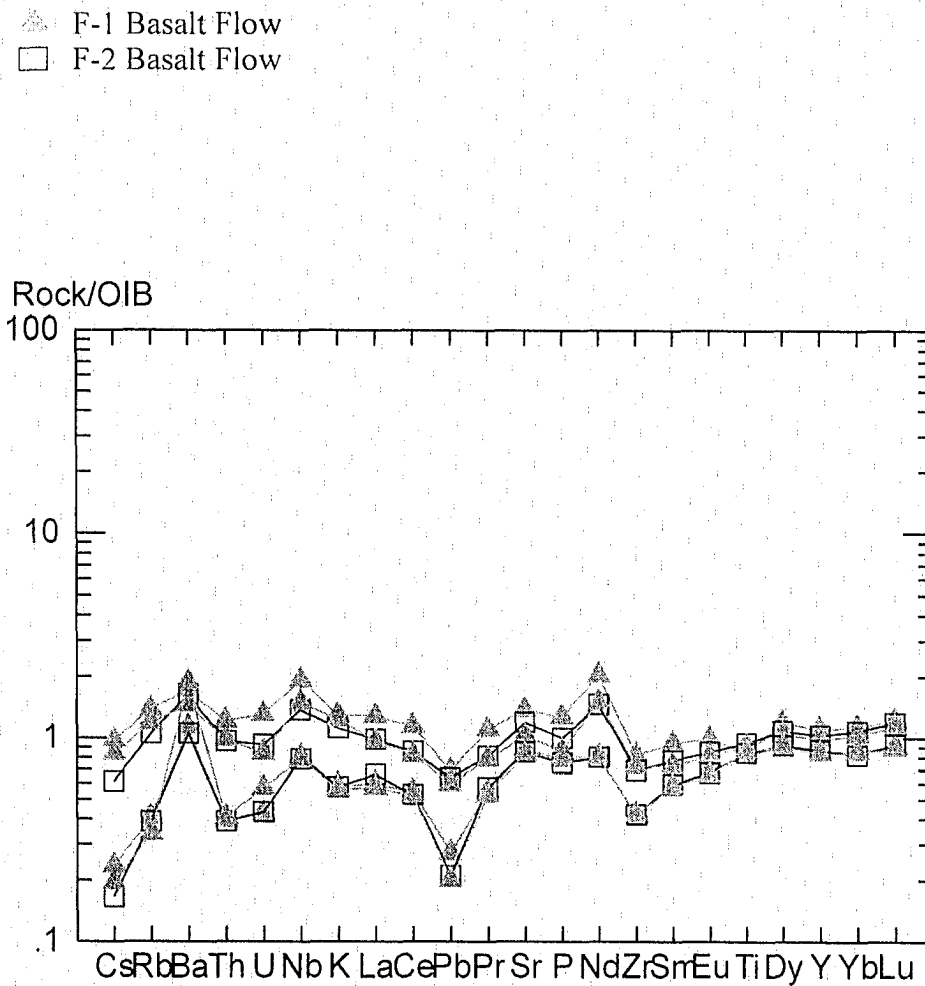


Figure 7: OIB-normalized (Sun and McDonough, 1989) trace element distribution diagram for samples from F-1 and F-2 basalt flows. Samples from F-1 and F-2 span both the depleted and enriched groups.

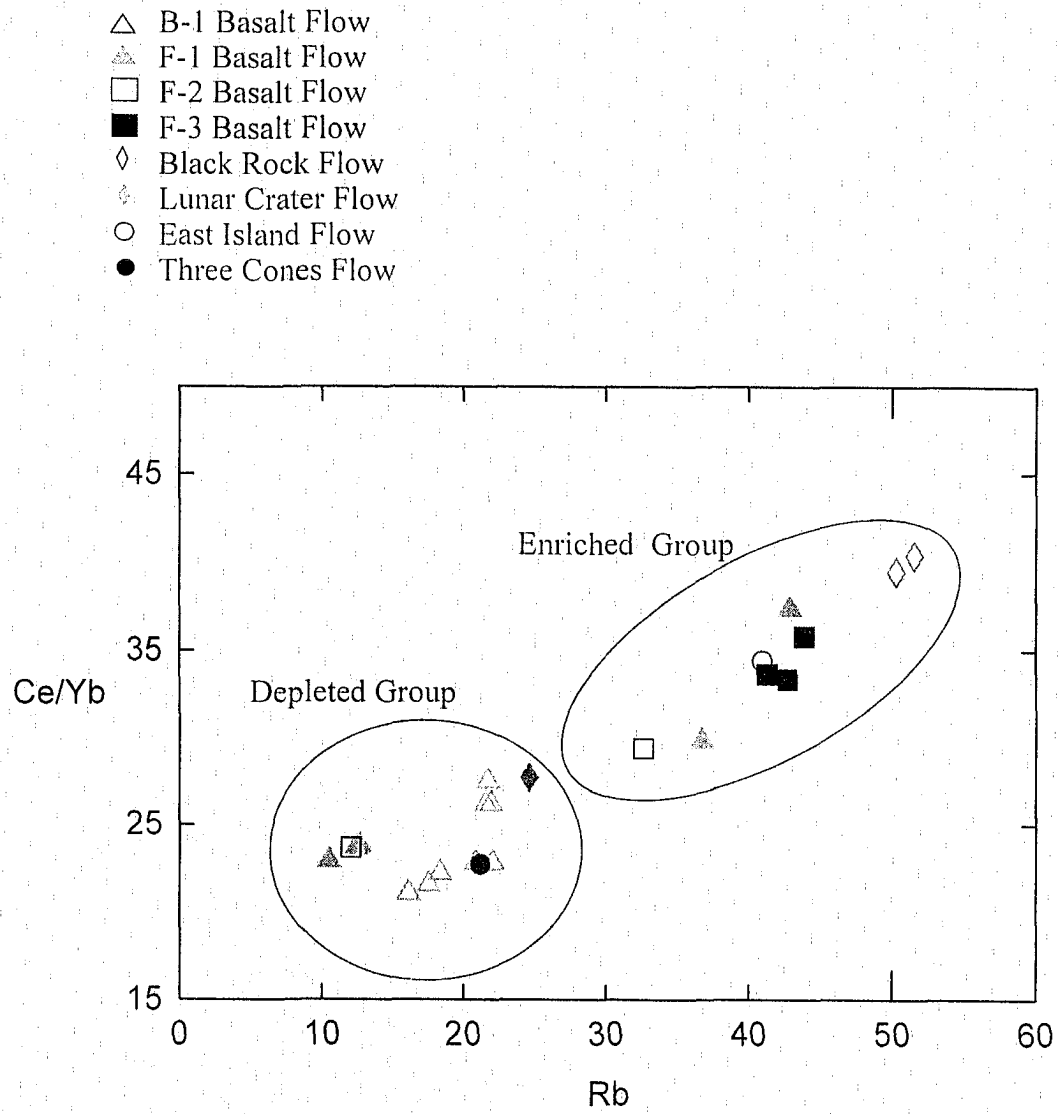


Figure 8: Ce/Yb vs. Rb diagram showing two distinct groups of mafic rocks in the NLCVF.

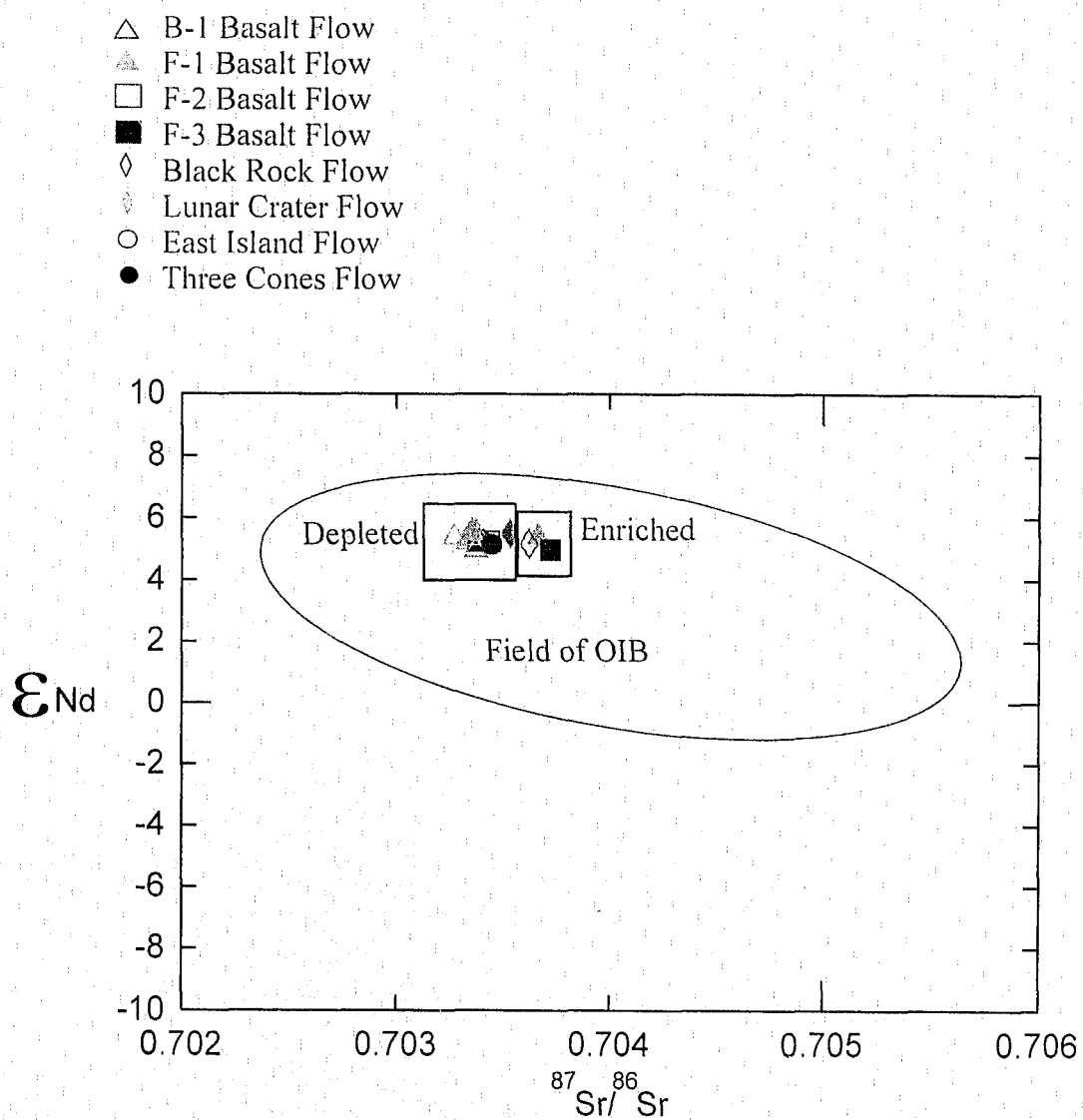


Figure 9: ϵ_{Nd} vs. $^{87}Sr/^{86}Sr$ for select samples in the NLCVF. Boxes indicate depleted and enriched groups. Field of Ocean Island Basalt is indicated by circle.

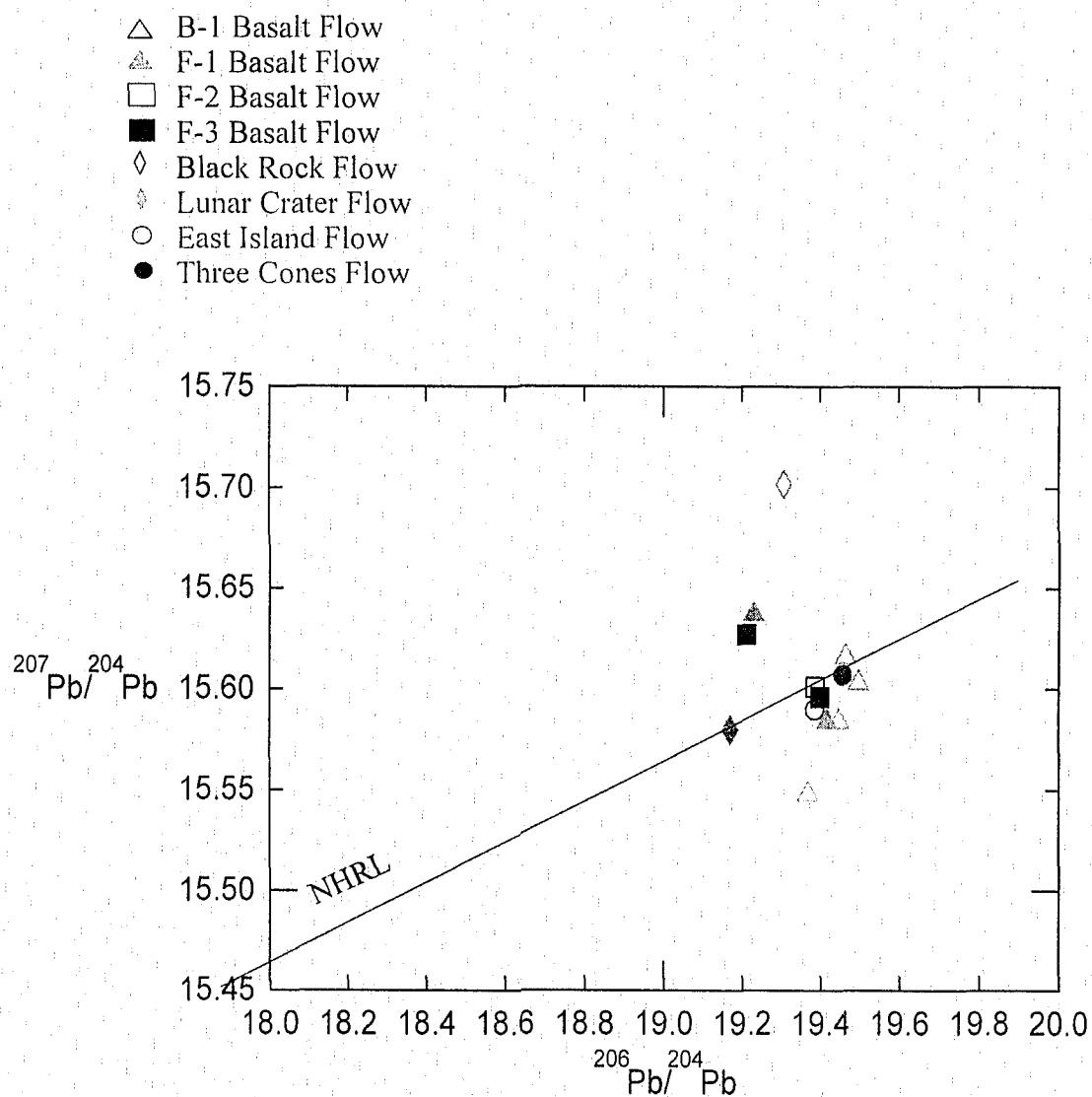


Figure 10: Pb isotopes for select samples in the NLCVF. NHRL is the North American Reference Line.

CHAPTER 4

INTERPRETATION

Geochemical models using fractional crystallization (FC), assimilation fractional crystallization (AFC) mixing and fractional melting were developed to model the petrogenesis of NLCVF basalts. Modeling included the use of the IGPETWIN computer program by Carr (1994) and fractional melting equations from Albarede (1995).

Models

Models were developed to explain the geochemical evolution of the field with emphasis on how the enriched and depleted groups (Chapter 3) are related.

The greatest success in modeling was achieved by examining in detail the F-1 and F-2 flows of the North Black Rock Cluster Cones. Specifically, the F-1 and F-2 flows were used because a large range of chemical variation from enriched to depleted groups is preserved within individual flows. Petrogenetic studies of individual flows, therefore, may serve as an analog to the evolution of the entire NLCVF. Interpretations were based on utilizing F-1 and F-2 as an analog to the field area.

Models of fractional crystallization, assimilation fractional crystallization and mixing use mafic rock specific distribution coefficient values compiled by the Center for Volcanic and Tectonic Studies over a five-year period (Table 5).

References for the distribution coefficients are Budahn et al. (1985); Lemarchand et al. (1987); Liotard et al. (1988); and Bradshaw (1991).

Observations and Assumptions

Models for the petrogenesis of NLCVF basalts must use the following constraints;

1. Element distribution diagrams normalized to OIB (Figures 6a, 6b and 7) as well as trace elements (Ce/Yb vs. Rb) define an enriched and depleted group of magmas (Chapter 3, Figure 8).
2. All samples group around a $^{87}\text{Sr}/^{86}\text{Sr}$ value of 0.7033 and ϵ_{Nd} of +5.5 and show an OIB-type signature.
3. Olivine, clinopyroxene and plagioclase are the most common phenocryst phases in the flows of the NLCVF. Oxides occur as minor phases.
4. New $^{40}\text{Ar}/^{39}\text{Ar}$ dates for the NLCVF show Central Flow basalt to be the oldest flow and F-3 basalt flow to be the youngest. The Central Flow basalt is 3.10 ± 0.4 Ma, Northeast Finger basalt 1.22 ± 0.2 Ma, F-1 basalt 1.20 ± 0.6 Ma and F-3 basalt 240 ± 340 ka (Table 1).

Geochemical modeling for F-1 and F-2 uses the following assumptions;

1. NLCVF basalts are cogenetic. Basalts in the NLCVF have similar chemistry, and a similar magma source. These basalts were erupted in a span of about 1 m.y. in a restricted area.
2. Basalt lava of an individual flow is comagmatic. This assumption infers that enriched and depleted group magmas present in both the F-1 and F-2 flows are comagmatic.

Fractional Melting Model

The first model tested the possibility that F-1, F-2 and F-3 evolved by fractional melting of a single mantle source.

A two-stage melting model was developed using data from F-1, as it provided the largest data set, and represented both the enriched and depleted groups. This model was tested using fractional melting equations from Albarede (1995), trace element values for OIB peridotite (Smith et al., 1999), and trace element information from the F-1 flow (See Appendix D- Model Data- Fractional Melting for calculations). Specifically, this model tests whether the enriched part of the F-1 flow can be produced by partial melting of OIB mantle peridotite and the depleted part of F-1 by the partial melting of the residual phases of the first melting event. The two-stage melting model begins with partial melting (4.19%) of the mantle source (OIB peridotite) to produce the enriched part of the F-1 flow (Sample LC-01-05-01). Calculated values of the trace element concentration in aggregate liquid agree with the actual acquired trace element values for the sample. The second stage of the model involves the fractional melting of the residuum of the first melting event. The residual mantle must be melted by very small amounts to enrich the liquid in incompatible elements, but it still fails to produce sufficient concentrations to match the composition of the depleted part of the F-1 flow (Sample LC-30-08-01) (See Appendix D-Model Data-Fractional Melting for calculations). Figure 11 graphically summarizes this model. This model must be discounted because the second stage of melting does not produce the observed trace element concentrations in the depleted group. Therefore, fractional melting of a single mantle source and subsequent melting of the residuum did not produce the chemical variations found in the F-1 flow.

An alternative model is to partially melt the mantle source by varying degrees to produce both the enriched and depleted groups.

This model again begins with fractional melting of an OIB peridotite mantle source by 4.19% to produce the enriched group (See Appendix D- Model Data- Fractional Melting for calculations). Next, the same OIB peridotite mantle source is melted by 9.9% to produce the depleted group. This model yields results which agree with the actual obtained values for the enriched and depleted group (Figure 12). The independent partial melting of the mantle source (OIB peridotite) by different degrees produced the observed depleted and enriched compositions in the F-1 flow, and is therefore noted as a plausible model to explain the relationship between the enriched and depleted groups.

Assimilation Fractional Crystallization

Another potential process for the evolution of the NLCVF is assimilation fractional crystallization (AFC). The identification of an appropriate assimilant is important for this model. The assimilant would need to have Rb concentrations (>80 ppm), with 2.3 to 2.5 ppm Yb. In order to be applicable to this model, the assimilant must not be felsic or intermediate in composition, as the addition of small amounts of these assimilants would cause the rocks to no longer be basalts. The petrologic model would need parameters of $R \approx 0.3$ (ratio of mass of assimilated material to mass of fractioned crystals) and $f_c \approx 10-15\%$ (amount of fractional crystallization) to be able to match the composition of the evolved rock. Options for this assimilant included xenoliths (mafic contaminants) or older basalts in the Reveille Range, or high Rb basalts located in the southern section of the LCVF. Unfortunately, none of these potential assimilants have the appropriate trace-element chemistry. Therefore, they must be ruled out as assimilants.

Because no appropriate contaminant could be identified, assimilation fractional crystallization using locally occurring mafic rocks is ruled out as the process responsible for the enriched and depleted chemical groups observed in the Northern Black Rock Cluster Cones F-1 and F-2 flows. Furthermore, no petrographic evidence for assimilation was identified in the NLCVF.

Fractional Crystallization within Individual Magma Batch

Another model tested was that of fractional crystallization within the individual magma batches. Models were developed using IGPETWIN (Carr, 1994) for flows F-1 and F-2 (Figure 13). For the F-1 flow, 68% plagioclase and 30% olivine were used in the model. For the F-2 flow, 56% plagioclase, 3% olivine and 40% clinopyroxene were used in the model. Multiple combinations of phases and elements were used in the attempted models. No reasonable results could be obtained by using this model, and therefore pure fractional crystallization within the individual flow is ruled out as a possible process for the observed chemical trends.

Magma Mixing

A final model tested to explain the chemical signatures of the depleted and enriched groups within F-1 and F-2 is magma mixing (Figure 14). Mixing of end member samples of F-1 and F-2 compositions of each flow were constructed. The data falls close to the end member of the mixing model, therefore mixing of two basaltic magmas is unlikely.

Furthermore, no basaltic rocks of intermediate composition exist within each flow.

Simple magma mixing is also ruled out as a possible process for the observed chemical trends.

Summary

Various models were developed in an effort to accurately describe the petrogenesis of the NLCVF. Of these models, the best fit to the data is the fractional melting model with independent partial melting of an OIB peridotite mantle source by varying degrees. A 4.19% fractional melting of an OIB peridotite source yields values similar to the enriched group, and 9.9% partial melting of the same OIB peridotite source yields values similar to those of the depleted group.

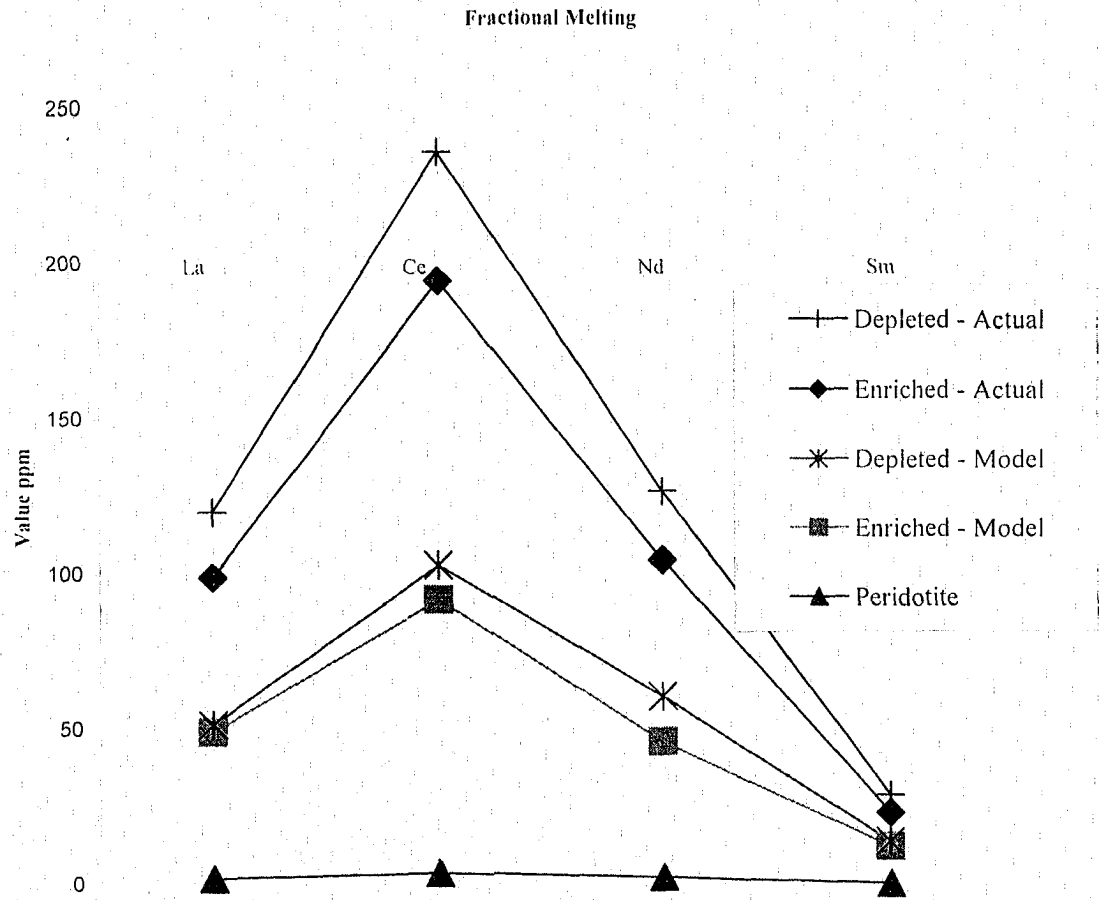


Figure 11: Two stage melting model. Stage one melt OIB peridotite to product enriched group. Stage two melt residue to produce depleted group. Model does not yield observed trends for depleted group.

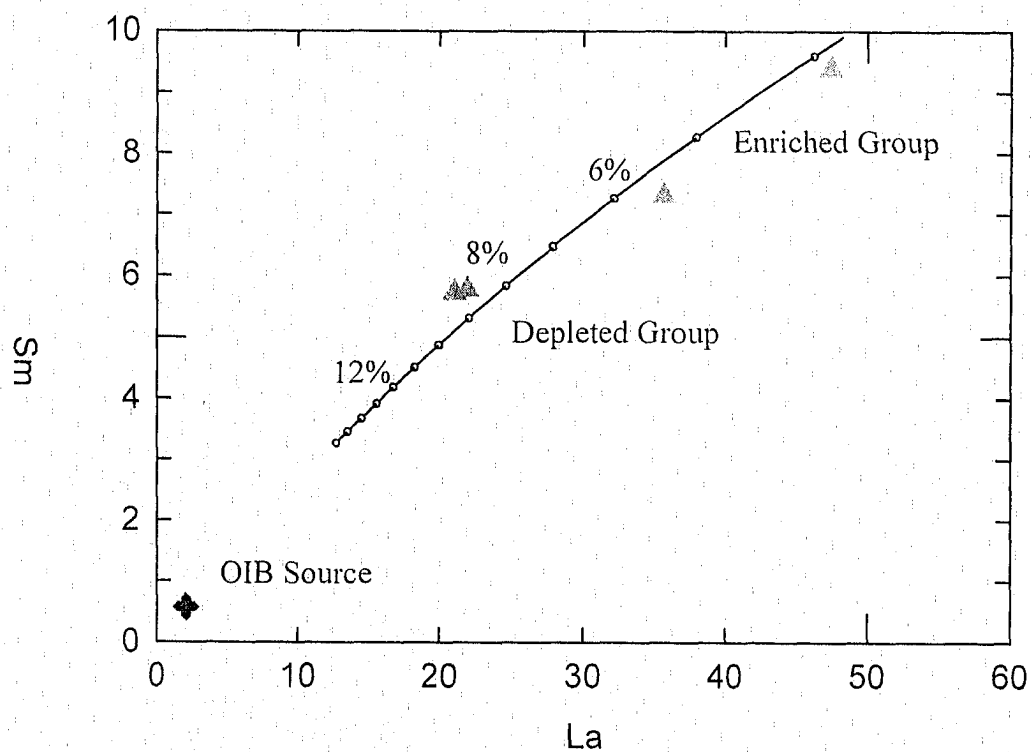


Figure 12: Fractional melting model of F-1 basalt flow. Partial melting of OIB peridotite (4.19%) yields enriched group, and partial melting of same OIB peridotite (9.9%) yields depleted group.

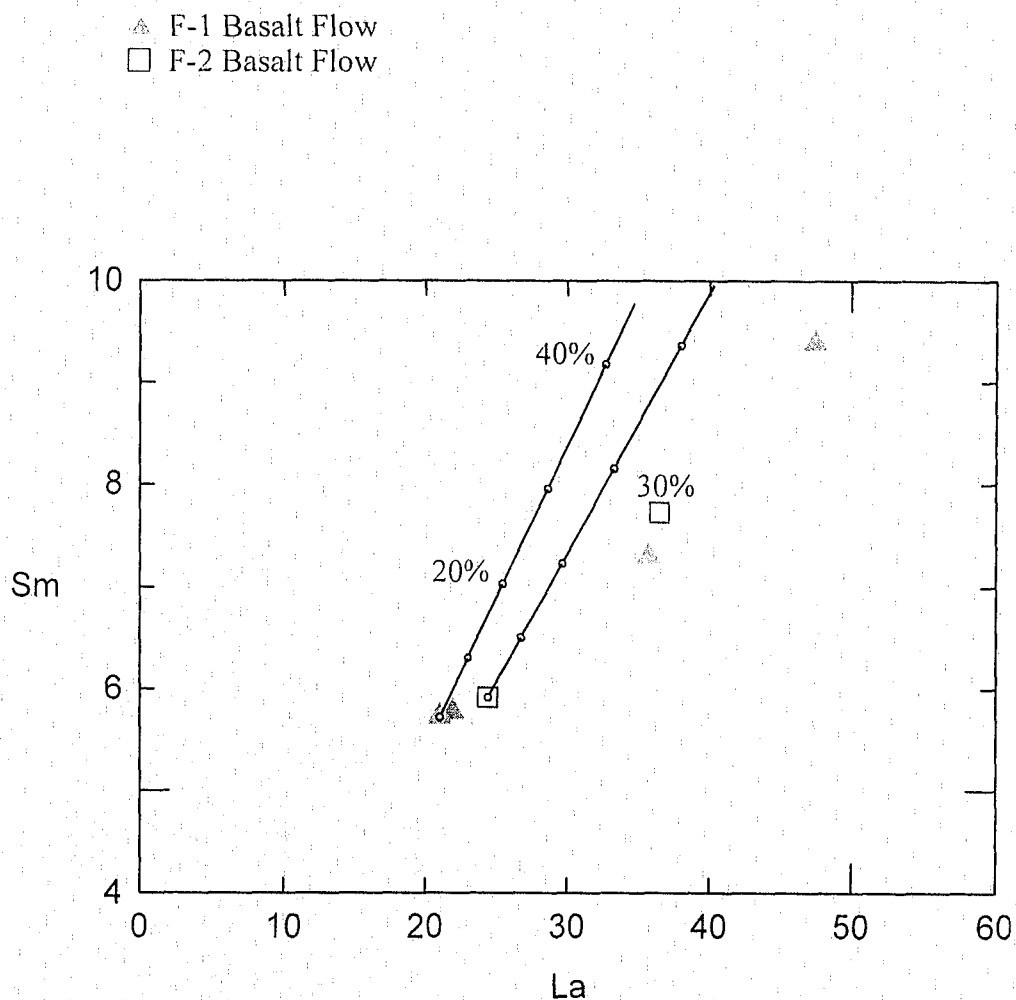


Figure 13: Fractional Crystallization Model for F-1 and F-2 flows. Model for the F-1 flow was constructed using 68% plagioclase and 30% olivine. Model for the F-2 flow was constructed using 56% plagioclase, 3% olivine and 40% clinopyroxene. Tick marks represent 10% increments of fractional crystallization. No appropriate model could be produced to explain observed geochemical trends.

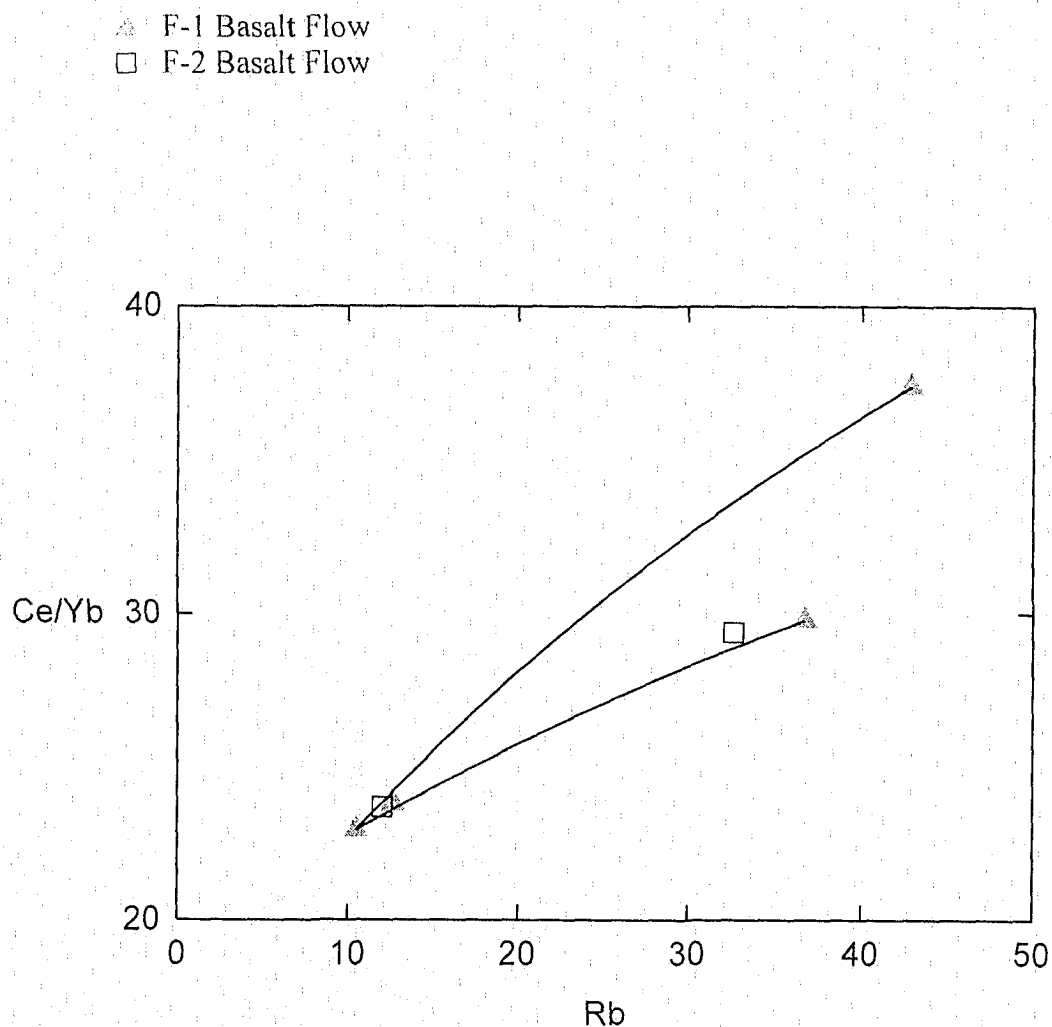


Figure 14 : Magma Mixing Model for the F-1 and F-2 Basalt Flows. Mixing was between end member compositions of flows. Model produces two-point solution and is discounted as process to explain observed geochemical trends.

Table 5: Distribution Coefficients			
Element	Plagioclase	Clinopyroxene	Olivine
La	0.20	0.069	0.002
Ce	0.18	0.098	0.0005
Nd	0.14	0.180	0.001
Sm	0.11	0.100	0.0013
Yb	0.03	0.300	0.100
Rb	0.07	0.030	0.010

CHAPTER 5

MANTLE MELTING MODEL

Introduction

Basalts of the NLCVF were produced by varying degrees of fractional melting of an OIB-mantle source (See Chapter 4). An important, but separate question is the depth of melting. In order to answer this question, a mantle melting model based on the methods of Wang et al. (2001) was produced. Major element analysis was used to construct a mantle melting column. The base of the melting column represents the initiation of melting, and is a function of mantle temperature. The top of the column represents the point at which magma ceases to rise adiabatically, and melting is therefore terminated. The total length of the melting column determines the total melt fraction. FeO is a depth indicator, and is used to indicate depth of melting. FeO becomes less compatible in olivine with depth (greater pressures) and its concentration is thus higher in higher-pressure melts. Melts from deep and hot mantle have higher FeO than those from relatively shallower mantle (Langmuir et al., 1992; Wang et al., 2001). Na₂O is used to determine the top of the melting column, as Na₂O content is a function of increasing melt fraction (concentration decreases with increasing melt fraction), and varies with clinopyroxene content. Na₂O content is controlled by pressure and amount of melting. With high pressure, the clinopyroxene melts quickly, enriching the initial liquid in Na₂O.

Because Na_2O is incompatible, the initial partial melt is greatly enriched in Na_2O , and since melting is fractional, each subsequent melting interval will have less Na_2O because Na_2O is depleted by previous melting episodes. Models are calculated with a H_2O free system, and corrected for effects on major elements due to fractional crystallization.

The mantle melting model uses accumulated fractional melting, resulting in melt compositions between batch and fractional melts (Langmuir et al., 1992), with melt pooled after each 1 kb of pressure release, and a simple one dimensional upwelling path (melting column) (Wang et al., 2001). This model is based on compositional changes of FeO , MgO and Na_2O in mantle melts assuming olivine-melt equilibrium and trace element behavior for Na (Wang et al., 2001). Based on the Langmuir et al. (1992) model, the mantle melting model utilizes the partition coefficients (K_d) for Mg and Fe in olivine (a function of pressure, temperature and alkali content) with MgO and FeO concentrations imposed by olivine saturation (Wang et al., 2001). Na_2O is calculated from K_d in clinopyroxene (a function of pressure and temperature) (Wang et al., 2001) using non-modal trace element equations (Langmuir et al., 1992). Additional parameters for the mantle melting model include an initial mantle composition of fertile lherzolite (with $\text{MgO} = 39.5\%$, $\text{FeO} = 8.2\%$, $\text{Na}_2\text{O} = 0.29\%$ and 15% clinopyroxene), the position of the mantle solidus (at pressure = 5.5 GPa with $T = 1150^\circ \text{C}$), and the relationship between temperature and percent of melting during isobaric and adiabatic melting.

Methods

To compare the samples from the NLCVF to those of primary melt compositions, samples are first reduced to a primary composition (similar to those of average Basin and Range xenolith olivine) by correcting for fractional crystallization, followed by using the addition of olivine to primitive compositions (Fe_{89}).

When correcting for fractional crystallization, Wang et al. (2001) suggest projection of basalt data to a high MgO value closer to primary compositions. Because a majority of Basin and Range basalts fall between 6 and 9 wt % MgO, the value of 8 wt. % MgO was selected. Next basalt geochemical data for each element is plotted against MgO and a regression line calculated. The concentration of each element is then determined at a MgO value of 8 wt. % (Figure 15). For example, the intersection of this regression line with the MgO=8 wt. % yields the $Fe_{8.0}$ value, and the highest FeO^* value along the regression line is designated as the Fe_{prim} value (most primitive sample) (Figure 15).

In order to calculate the Fe_{89} value, equilibrium olivine is added in 1% increments until the resulting basaltic magma is in equilibrium with Fe_{89} olivine (Wang et al., 2001). In order to assess how the varying amounts of fractional crystallization or contamination play into the calculations, comparisons of both $Fe_{8.0}$ and Fe_{prim} are used. Figure 15 graphically represents this process.

Accumulated fractional melting paths are calculated from the Langmuir et al. (1992) model. The curve generated represents a pressure of intersection with the mantle solidus (P_0), and the point at which the mantle ceases to rise adiabatically (P_f).

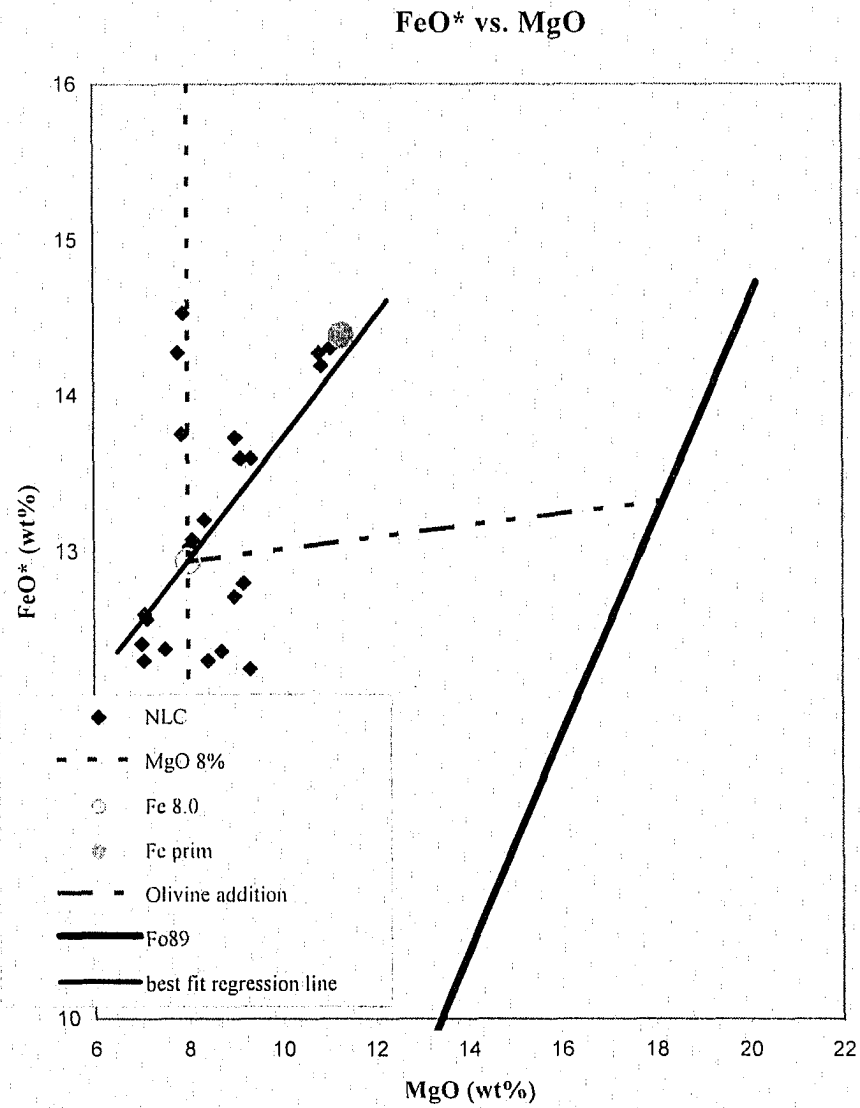
The total melting column length ($P_0 - P_f$) determines the total melt fraction (F). This mantle melting model is shown graphically in Figure 16. Final Na_2O and FeO contents of the mantle melt provide the initial depth of melting (FeO indicating P_0) and final depth of melting (Na_2O indicating F). All calculations were completed in Excel worksheets.

Conclusions

Using these methods, the mantle melting column was calculated for samples in the NLCVF. A Fe_{prim} value of 14.39 (calculated from Figure 15) was used and the model predicts initial melting at 5.4 GPa (depth of 175 km) and final melting at 4.3 GPa (depth of 130 km) (Figure 16). These results indicate very deep, hot ($>1500^\circ\text{C}$) melting in the asthenospheric mantle. Wang et al. (2001) applied these methods to samples across the Great Basin, to create a mantle melting profile. Using this information, their model predicts a profile that ‘follows’ the asthenosphere/lithosphere boundary and this boundary location is supported by other geophysical and geological studies. Wang et al. (2001) suggested that melting occurs largely in the asthenosphere, and that melting ceases at the base of the lithosphere. Their evidence supports deep hot melting along the axis of the Great Basin with mantle temperatures an average of 200°C hotter than average asthenosphere. Wang et al. (2001) suggests that this is evidence of a mantle hot spot or plume. Findings from this study support the conclusions of Wang et al. (2001) and indicate that deep hot melting of asthenospheric mantle occurred in this area. Thus, the possibility exists for the presence of a mantle melting anomaly under the NLCVF.

Evidence for a mantle anomaly, possibly a mantle plume exists, however the area of magmatism is of small volume, not typical of the large volume volcanism that accompanies plume melting, and furthermore there is no plume track or clear cut progression in age. One possibility of a mantle anomaly is that of a mantle roll, or eddy. The eddy or roll may preferentially occur near where the lithosphere-asthenosphere contact has a significant relief. As the lithosphere travels through the asthenosphere, a wake (such as that of a boat) is produced which moves with the lithosphere, typically at major lithospheric boundaries (Smith, in press). Figure 17 is a cartoon representation of this mantle roll hypothesis. A lithospheric keel may exist in this area, because the DV-PRBZ is near the western edge of the Precambrian craton (Farmer and DePaolo, 1983), and this area is also marked by a section of lithospheric thickening related to the Sonoran, Antler and Sevier Orogenies (Rogers, 1993; Taylor et al., 2000). If a keel exists, its movement through the asthenosphere might produce a mantle roll and explain the source of the mantle melting anomaly.

Conclusions from the mantle melting model (this study and Wang et al., 2001) suggest that the possibility exists for a link in the volcanic fields along the DV-PRBZ / Basin and Range by a common deep mantle source. This could explain the unique location of the NLCVF along the axis of the Great Basin. This mantle anomaly under the NLCVF would produce the deep, hot melting observed in the calculations, and even though the mantle material is hotter than average, the relatively short column length contributes to the small volume of the NLCVF.



Mantle Melting Model

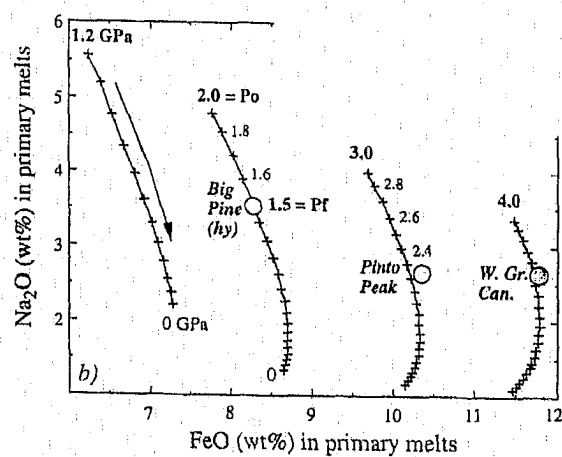
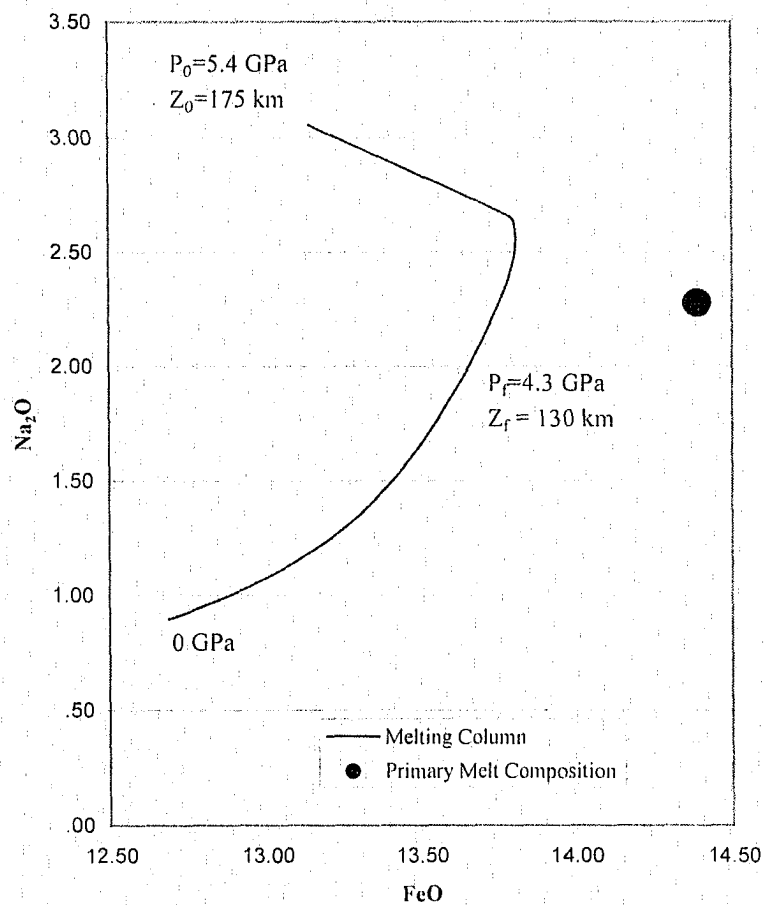


Figure 16: Mantle melting model showing initial pressure/depth of melting and final pressure/depth of melting. Insert details melting paths from Great Basin area (From Wang et al., 2000).

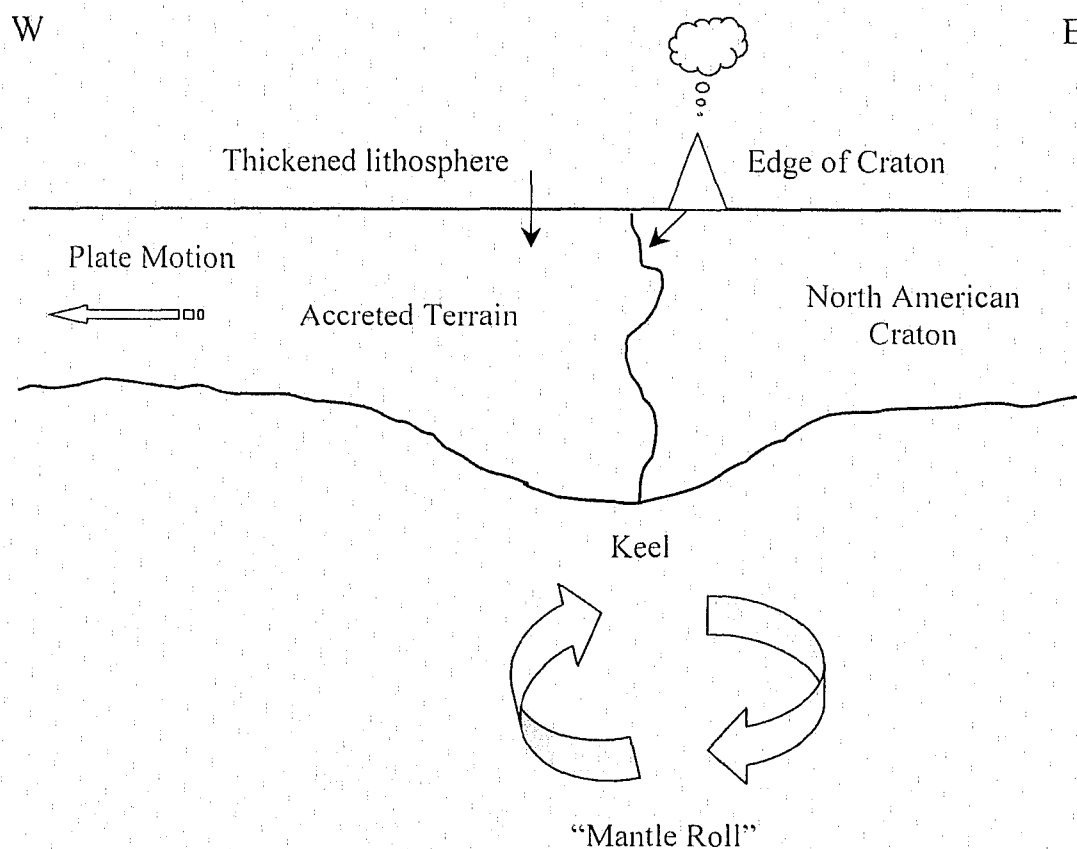


Figure 17: Cartoon representation of mantle roll hypothesis. The Precambrian boundary is located to the west of the NLCVF, and sections of thicker lithosphere due to orogenic episodes occurs in the field area. Lithospheric keel creates a wake in the mantle. Lunar Crater Volcanic Field indicated by volcano.

CHAPTER 6

FUTURE ERUPTIONS

There is a high likelihood of future volcanic eruptions at the northern terminus of the DV-PRBZ. Previous work in the DV-PRBZ by Crowe et al. (1992) concluded that new volcanic events will occur every 22 to 100 ka. Models by Crowe et al. (1992) use uniform temporal distribution and homogenous Poisson models, yielding a simplified assessment of recurrence rates. Additional models by Ho et al. (1991) and Ho and Smith (1998) use non-homogeneous models that are sensitive to waning, steady or increasing frequency of volcanism (Smith and Keenan, 2001), and suggest that recurrence rates of >15 events per million years, or an event approximately every 67 ka. The youngest flow (Black Rock) was previously dated at 20 ± 9 ka ($^{40}\text{Ar}/^{39}\text{Ar}$) by Dickson (1998). Based on this date and the recurrence rate of Crowe et al. (1992), a future eruption can be expected within the next 60-70 ka. Based on this date, and utilizing the methods of Ho et al. (1991) and Ho and Smith (1998) an eruption can be expected in the next 37,667 to 55,667 years. This eruption would most likely occur in the vicinity of the Black Rock or Northern Black Rock Cluster Cones area. Disruption of U.S. Highway 6 would occur in the event of a future eruption. This is particularly relevant, as the D.O.E. has indicated intent to transport medium-level nuclear waste to the Yucca Mountain Nuclear Repository along U.S. Highway 6 (Tetreault, 2003).

CHAPTER 7

SUMMARY AND CONCLUSIONS

Based on field observations, geochemistry and new $^{40}\text{Ar}/^{39}\text{Ar}$ dates for the NLCVF, this area of relatively young, small volume, basalt represents a simple volcanic system. Basaltic flows can be grouped into those of trace element enrichment, and those of trace element depletion with a deep (175 to 130 km) asthenospheric mantle source. Asthenospheric melting is further supported by Sr and Nd isotopic ratios. Flows in the NLCVF developed by differing degrees of partial melting, independent of one another with little evidence of crustal contamination, or commingling. In the case of the North Black Rock Cluster Cones multiple eruptions occurred from the same volcanic vents between 1.20 ± 0.55 Ma (F-1, Table 1) and 0.24 ± 0.34 Ma (F-3, Table 1). Even though the F-1, F-2 and F-3 basalt flows erupted from the same volcanic vent, the F-1 and F-2 flows represents different magma groups (Chapter 3). The basalts of the NLCVF were erupted over a short period of time in a well-defined area along the DV-PRBZ. The depth of melting (175 to 130 km), as determined by the mantle melting model, indicates that this particular volcanic field might be controlled by a deep, hot mantle source. This may be attributed to a mantle melting anomaly such as a mantle roll. Although this hotter than average mantle exists, its depth indicates that basaltic magma would have to rise a great distance to reach the surface. Considered along with a thicker lithosphere in the area under the NLCVF, and a relatively short calculated melting column of 40 km, these three factors could explain why the volcanic field is small in volume.

In addition, this mantle anomaly might contribute to the unique location of the NLCVF in the DV-PRBZ along the axis of the Great Basin at the edge of the Precambrian boundary. The likelihood of volcanic hazards exists in the northernmost section of this field in the vicinity of Black Rock and the Northern Black Rock Cluster Cones within the next 38-56 ka. Future eruptions in this area would disrupt transportation along U.S. Highway 6.

REFERENCES CITED

- Albarede, F., 1995, *Introduction to Geochemical Modeling*: Cambridge University Press: p. 497- 498.
- Best, M.J. and Brimhall, W.H., 1974, Late Cenozoic alkali basaltic magmas in the western Colorado Plateau and the Basin and Range transition zone, USA and their bearing on mantle dynamics: *GSA Bulletin*, v. 85, p. 1677-1690.
- Bradshaw, T.K., 1991, *Tectonics and magmatism in the Basin and Range Province of the Western United States [Ph.D. thesis]*: Milton Keynes, Open University, 247 p.
- Bradshaw, T.K. and Smith, E.I., 1994, Polygenetic Quaternary volcanism at Crater Flat, Nevada: *Journal of Volcanology and Geothermal Research*, v. 63, p. 165-182.
- Budahn, J.R. and Schmitt, R.A., 1985, Petrogenetic modeling of Hawaiian tholeiitic basalts: A geochemical approach: *Geochimica et Cosmo Acta*, v. 49, p. 67-87.
- Byers, F.M., Carr, W.J., Orkild, P.P., Quinivan, W.D. and Sargent, K.A., 1976, Volcanic suites and related cauldrons of the Timber Mountain-Oasis Valley caldera complex, southern Nevada: *USGS Professional Paper 919*, 70 p.
- Carr, M.J., 1994, *IGPETWIN: Igpert for Windows petrology software*: Somerset, Terra Softa, Inc.
- Cebula, G.T., Kunk, M.J., Mehnert, H.H., Naeser, C.W., Obradovich, J.D. and Sutter, J.F., 1986, The Fish Canyon Tuff, a potential standard for the ^{40}Ar - ^{39}Ar and fission-track dating methods (abstract), *Terra Cognita (6th International Conference on Geochronology, Cosmochronology and Isotope Geology)*, v. 6, 139 p.
- Christiansen, R.L. and Lipman, P.W., 1972, Cenozoic volcanism and plate tectonic evolution of the western United States, II, Late Cenozoic: *Philosophical Transactions by the Royal Society of London*, v. 271, p. 249-284.
- Christiansen, R.L., Lipman, P.W., Carr, W.J., Byers, F.M., Orkild, P.P. and Sargent, K.A., 1977, Timber Mountain-Oasis Valley caldera complex of southern Nevada: *Geological Society of America Bulletin*, v. 88, p. 943-956.

- Conduit, C.D., Crumpler, L.S., Aubele, J.C. and Elston, W.E., 1989, Patterns of volcanism along the south margin of the Colorado Plateau: The Springerville Field: *Journal of Geophysical Research*, v. 94, p. 7975-7986.
- Connor, C.B., 1994, Estimating recurrence rate of volcanism in the Springerville Volcanic Field, Arizona: *GSA Abstracts with Programs*, v. 26, no. 7.
- Crowe, B.M., Picard, R., Valentine, G. and Perry, F.V., 1992, Recurrence models of volcanic events: applications to volcanic risk assessment: *Proceedings of the International Nuclear Waste Symposium*, v. 2, American Nuclear Society and American Society of Civil Engineers, p. 2344-2355.
- Dickson, L.R., 1998, *Volcanology and Geochemistry of Pliocene and Quaternary basalts on Citadel Mountain, Lunar Crater Volcanic Field, Pancake Range, Nevada: [Master's Thesis]*, Las Vegas, University of Nevada, 146 p.
- Dohrenwend, J.C., Wells, S.G. and Turrin, B.D., 1986, Degradation of Quaternary cinder cones in the Cima volcanic field, Mojave Desert, California: *Geological Society of America Bulletin*, v. 97, p. 421-427.
- Dohrenwend, J.C., Abrahams, A.D. and Turrin, B.D., 1987, Drainage development on basaltic lava flows, Cima volcanic field, southeast California, and Lunar Crater volcanic field, south-central Nevada: *GSA Bulletin*, v. 99, p. 405-413.
- Downing, R.F., Smith, E.I., Orndorff, R.L., Spell, T.L. and Zanetti, K.A., 2000, Imaging the Colorado Plateau-Basin and Range Transition Zone Using Basalt Geochemistry, Geochronology and Geographical Information Systems: *Utah Geological Survey and American Association of Petroleum Geologists, Special Volume on Colorado Plateau-Basin and Range Transition Zone*, 31 p.
- Eaton, G.P., 1982, The Basin and Range Province: Origin and tectonic significance: *Annual Review of Earth and Planetary Sciences*, v. 10, p. 409-440.
- Farmer, G.L. and DePaolo, D.J., 1983, Origin of Mesozoic and Tertiary granite in the Western United States and implications for pre-Mesozoic Crustal Structure 1. Nd and Sr isotopic studies in the geocline of the northern Great Basin: *Journal of Geophysical Research*, v. 88, no. B4, p. 3379-3401.
- Farmer, G.L., Perry, F.V., Semken, S., Crowe, B., Curtis, D. and DePaolo, D.J., 1989, Isotopic evidence on the structure of origin of subcontinental lithospheric mantle in southern Nevada: *Journal of Geophysical Research*, v. 94, no. B6, p. 7885-7898.

- Fitton, J.G., James, D., Kempton, P.D., Ormerod, D.S. and Leeman, W.P., 1988, The role of lithospheric mantle in the generation of late Cenozoic basic magmas in the western United States: *Journal of Petrology*, Special Lithosphere Issue, p. 331-349.
- Fitton, J. G., James, D. and Leeman, W.P., 1991, Basic magmatism associated with Late Cenozoic extension in the western United States: Compositional variations in space and time: *Journal of Geophysical Research*, v. 96, n. B8, p. 13,693-13,711.
- Foland, K.A., Kargel, J.S., Lum, C.L. and Bergman, S.C., 1987, Time-spatial-compositional relationships among alkali basalts in the vicinity of the Lunar Crater, south-central Nevada: *Geological Society of America, Abstracts with Programs*, v.19, p. 666.
- Foland, K.A. and Bergman, S.C., 1992, Temporal and spatial distribution of basaltic volcanism in the Pancake and Reville Ranges north of Yucca Mountain: in *Proceedings of the International Nuclear Waste Symposium*, v. 2, American Nuclear Society and American Society of Civil Engineers, p. 2366-2371.
- Ho, C.H., and Smith, E.I., 1998, A Spatial-Temporal/3-D Model for Volcanic Hazard Assessment: Application to the Yucca Mountain Region, Nevada: *Mathematical Geology*, v. 30, p. 497-510.
- Ho, C.H., Smith, E.I., Feuerbach, D.L. and Naumann, T.R., 1991, Eruptive probability calculation for the Yucca Mountain site, USA: statistical estimation of recurrence rates: *Bulletin of Volcanology*, v. 53.
- Hoffer, J.M., 1976, *Geology of Potrillo Basalt Field, South-central New Mexico*: New Mexico Bureau of Mines & Mineral Resources, v. 149, 30 p.
- Kargel, J.S., 1987, The geochemistry of basalts and mantle inclusions from the Lunar Crater Volcanic Field, Nevada; petrogenetic and geodynamic implications [Master's Thesis]: Ohio State University, Columbus, Ohio, 369 p.
- Langmuir, C.H., Klein, E.M. and Plank, T., 1992, Petrological systematics of mid-ocean ridge basalts: constraints on melt generation beneath ocean ridges, in *Mantle Flow and Melt Generation at Mid-Ocean Ridges: Geophysics Monthly*, v. 71, p. 183-280.
- LeBas, M.J., LeMaitre, R.W., Streckeisen, A. and Zanettin, B., 1986, A chemical classification of volcanic rocks based on the total alkali silica diagram: *Journal of Petrology*, v. 27, p. 745-750.
- Lemarchand, F., Villemant, B. and Calas, G., 1987, Trace element distribution coefficients in alkaline series: *Geochimica et Cosmo Acta*, v. 51, p. 1071-1081.

- Liotard, J.M., Briot, D. and Biovin P., 1988, Petrological and geochemical relationships between pyroxene megacrysts and associated alkali-basalts from Massif Central (France): *Contributions to Mineralogy and Petrology*, v. 98, p. 81-90.
- Livaccari, R.F. and Perry, F.V., 1993, Isotopic evidence for preservation of Cordilleran lithospheric mantle during the Sevier-Laramide orogeny, western United States: *Geology*, v. 21, p. 719-722.
- Lum, C.C.L., Leeman, W.P., Foland, K.A., Kargel, J.A. and Fitton, J.G., 1989, Isotopic variations in continental basaltic lavas as indicators of mantle heterogeneity: examples from the western U.S. Cordillera: *Journal of Geophysical Research*, v. 94, no. B6, p. 7871-7884.
- Naumann, T.R., Smith, E.I., Shafiqullah, M. and Damon, P.E., 1991, New K-Ar ages for mafic to intermediate volcanic rocks in the Reville Range, Nevada: *Isochron West*, p. 12-16.
- Rogers, J.W., 1993, *A History of the Earth*, Cambridge University Press, 312p.
- Scott, D.H., 1969, *The Geology of the Southern Pancake Range and Lunar Crater volcanic field Nye County, Nevada* [Ph.D. thesis]: Los Angeles, University of California, 122 p.
- Scott, D.H. and Trask, N.J., 1971, *Geology of the Lunar Crater Volcanic Field, Nye County, Nevada*: U.S. Geological Survey Professional Paper 599-I, p. 1-22.
- Severinghaus, J. and Atwater, T., 1990, Cenozoic geometry and thermal state of the subducting slabs beneath western North America, in Werncke, B.P., ed., *Basin and Range extensional tectonics near the latitude of Las Vegas, Nevada*: Boulder, Colorado, Geological Society of America Memoir 176, p.1-22.
- Shepard, M.K., Arvidson, R.E., Caffee, M., Finkel, R. and Harris, L., 1995, Cosmogenic exposure ages of basalt flows: Lunar Crater volcanic field, Nevada: *Geology*, v. 23, no. 1, p. 21-24.
- Sigurdsson, H., Houghton, B.F., McNutt, S.R., Rymer, H. and Stix, J., 2000, *Encyclopedia of Volcanoes*: Academic Press, 1417 p.
- Smith, A.D., 2003, A re-appraisal of stress field and convective roll models for the origin and distribution of Cretaceous to Recent intraplate volcanism in the Pacific Basin, *International Geology Review*, v. 45, in press.
- Smith, E.I., Sanchez, A., Walker, J.D. and Wang, K., 1999, Geochemistry of Mafic Magmas in the Hurricane Volcanic Field, Utah: Implications for Small- and Large-Scale Chemical Variability of the Lithospheric Mantle: *The Journal of Geology*, v. 107, p. 433-448.

- Smith, E.I. and Keenan, D.L., 2001, Some new observations about basaltic volcanism near Yucca Mountain: Implications for volcanic hazard studies: Agency for Nuclear Projects, State of Nevada special report, 41 p.
- Staudacher, T.H., Jessberger, E.K., Dorflinger, D. and Kiko, J., 1978, A refined ultrahigh-vacuum furnace for rare gas analysis: *Journal of Physics E: Science Instruments*, v. 11, p. 781-784.
- Steven, T.A., Mehnert, H.H. and Obradovich, J.D., 1967, Age of volcanic activity in the San Juan Mountains, Colorado: *United States Geological Survey Professional Paper*, v. 575-D, p. 47-55.
- Sun, S., and McDonough, W.F., 1989, Chemical and isotopic systematics of oceanic basalts: Implications for mantle composition and processes, in Sanders, A.D., and Norry, M.J. eds., *Magmatism in the oceanic basins: Geological Society [London] Special Publication 41*, p. 313-314.
- Taylor, W.J., Bartley, J.M., Martin, M.W., Geissman, J.W., Walker, J.D., Armstrong, P.A., and Fryxell, J.E., 2000, Relations between hinterland and foreland shortening, Sevier orogeny, Central North American Cordillera: *Tectonics*, v. 19, p. 1124-1143.
- Tetreault, S., 2003, Waste route stirs debate: *Las Vegas Review Journal*, Tue Aug 19.
- Vaniman, D.T., Crowe, B.M. and Gladney, E.S., 1982, Petrology and geochemistry of Hawaiiite lavas from Crater Flat, Nevada: *Contributions to Mineralogy and Petrology*, v. 80, p. 341-357.
- Walker, G.P.L., 1991, Structure and origin by injection of lava under surface crust, of tumuli, "lava rises," "lava-rise pits," and "lava inflation clefts" in Hawaii, *Bulletin of Volcanology*, v. 53, p. 546-558.
- Wang, K., Plank, T., Walker, J.D. and Smith, E.I., 2001, A Mantle Melting Profile Across the Basin and Range, SW USA, *Journal of Geophysical Research*, in press.
- Wells, S.G., McFadden, L.D., Renault, C.E. and Crowe, B.M., 1990, Geomorphic assessment of Late Quaternary volcanism in the Yucca Mountain area, southern Nevada: Implications for the high-level radioactive waste repository: *Geology*, v. 18, p. 549-553.
- Wendt, I. And Carl, C., 1991, The statistical distribution of the mean squared weighted deviation, *Chemical Geology*, v. 86, p. 275-285.
- Wilson, M., 1989, *Igneous Petrogenesis*: London, Unwin Hyman, 466p.

Yogodinski, G.M., Naumann, T.R., Smith, E.I., Bradshaw, T.K. and Walker, J.D., 1996, Evolution of a mafic volcanic field in the central Great Basin, south central Nevada: *Journal of Geophysical Research*, v. 101, no. B8, p. 17,425-17,445.

APPENDIX A: GEOCHEMICAL ANALYSES

Sample	LC-01-05-01	LC-02-06-01	LC-03-06-01	LC-04-07-01	LC-05-07-01
<i>X-Ray Fluorescence Analyses, wt %</i>					
SiO ₂	46.07	46.24	45.74	47.24	46.17
Al ₂ O ₃	14.48	14.76	15.13	15.51	14.98
TiO ₂	2.45	2.70	2.30	2.51	2.71
FeO	12.80	13.08	11.81	12.41	12.30
MgO	9.18	8.10	6.99	7.01	8.42
CaO	9.94	9.20	9.19	8.43	9.65
Na ₂ O	3.64	3.25	4.47	3.98	3.32
K ₂ O	1.87	1.20	2.02	1.90	1.61
MnO	0.20	0.17	0.20	0.19	0.17
P ₂ O ₅	0.79	0.49	0.81	0.83	0.62
Total	101.42	99.18	98.67	100.01	99.95
<i>X-Ray Fluorescence Analyses, ppm</i>					
Zr	214.41	161.51	259.41	234.91	188.39
Sr	707.86	495.02	896.08	750.45	619.78
Nb	92.25	51.66	103.91	74.42	65.94
Y	20.16	19.47	20.73	20.31	19.89
Rb	32.11	17.69	40.32	29.83	24.95
Cr	449.62	198.97	260.58	196.41	233.00
Ni	213.10	177.42	113.72	108.79	148.09
<i>Inductively Coupled Plasma Mass Spectrometry (REE) Analyses, ppm</i>					
La	47.46	26.57	54.48	46.93	36.45
Ce	91.44	52.11	101.61	87.82	68.63
Pr	10.68	6.19	11.69	9.96	7.9
Nd	43.97	27.08	46.9	40.44	33.12
Sm	9.39	6.85	9.75	8.84	7.73
Eu	2.98	2.32	3.15	2.9	2.57
Gd	8.06	6.73	8.03	7.96	7.12
Tb	1.2	1.04	1.2	1.19	1.06
Dy	6.667	6.03	6.63	6.67	6.07
Ho	1.24	1.16	1.24	1.25	1.15
Er	3.08	2.79	3.12	3.18	2.87
Tm	0.42	0.39	0.44	0.44	0.39
Yb	2.45	2.29	2.52	2.55	2.34
Lu	0.37	0.34	0.39	0.39	0.36
Ba	604	353	785	598	573
Th	4.84	2.64	6.2	5	3.85
Nb	78.7	41.7	89.3	67.04	56.4
Y	32.05	29.37	32.76	32.75	29.95
Hf	5.5	4.29	5.85	5.73	4.68
Ta	4.9	2.72	5.63	4.28	3.57
U	1.33	0.75	1.61	1.29	0.94
Pb	2.2	1.61	2.91	2.28	2.03
Rb	42.9	22.1	51.6	41	32.6
Cs	0.38	0.35	0.52	0.36	0.24
Sr	910	634	1119	931	790
Sc	26.3	28.3	22.9	22	29.2
Zr	231	168	261	246	194
W	48.9	41.5	50.3	34.5	31.9

APPENDIX A: GEOCHEMICAL ANALYSES

Sample	LC-06-07-01	LC-07-07-01	LC-09-08-01	LC-10-08-01	LC-12-08-01
<i>X-Ray Fluorescence Analyses, wt %</i>					
SiO ₂	46.28	47.54	46.93	46.19	45.88
Al ₂ O ₃	14.09	15.58	15.27	15.47	15.35
TiO ₂	2.31	2.48	2.68	2.81	2.75
FeO	12.24	12.57	13.03	14.28	13.75
MgO	9.31	7.12	8.03	7.80	7.88
CaO	10.02	8.49	9.28	8.98	9.29
Na ₂ O	3.52	4.00	3.23	3.08	3.08
K ₂ O	1.87	1.96	1.17	1.25	1.26
MnO	0.20	0.19	0.17	0.17	0.17
P ₂ O ₅	0.76	0.83	0.50	0.58	0.58
Total	100.60	100.75	100.30	100.61	100.00
<i>X-Ray Fluorescence Analyses, ppm</i>					
Zr	215.20	248.93	184.41	178.10	174.20
Sr	700.38	773.96	555.52	624.47	624.05
Nb	85.84	85.92	49.51	52.77	56.44
Y	20.27	20.91	19.96	19.58	19.74
Rb	34.58	33.51	16.94	19.07	18.21
Cr	573.16	219.27	221.89	179.24	167.11
Ni	217.82	194.21	156.79	121.75	116.35
<i>Inductively Coupled Plasma Mass Spectrometry (REE) Analyses, ppm</i>					
La	46.01	48.1	26.96	30.75	30.28
Ce	88.45	89.38	52.12	60.24	58.97
Pr	10.37	10.18	6.25	7.19	7.03
Nd	42.58	41.54	27.01	31.14	30.49
Sm	9.23	9.15	6.84	7.41	7.2
Eu	2.89	2.96	2.39	2.6	2.55
Gd	8.04	8.07	6.72	7.06	6.88
Tb	1.17	1.24	1.06	1.11	1.08
Dy	6.57	7	6	6.19	6.18
Ho	1.22	1.32	1.13	1.15	1.15
Er	3.03	3.31	2.92	2.97	2.82
Tm	0.42	0.47	0.39	0.39	0.39
Yb	2.47	2.68	2.29	2.3	2.25
Lu	0.37	0.41	0.34	0.35	0.33
Ba	600	640	361	522	532
Th	4.69	4.86	2.66	2.83	2.56
Nb	74.84	67.69	40.76	46.01	44.92
Y	31.68	34.45	29.6	30.27	29.81
Hf	5.33	5.89	4.22	4.26	4.07
Ta	4.72	4.35	2.65	2.94	2.79
U	1.23	1.26	0.72	0.49	0.65
Pb	2.16	2.69	1.49	1.45	1.52
Rb	43.9	42.7	20.9	22	21.6
Cs	0.46	0.49	0.45	0.19	0.21
Sr	888	933	639	773	742
Sc	27.7	23.2	25.4	25.7	25
Zr	223	251	166	166	161
W	71.1	52.7	37.7	54.6	30.2

APPENDIX A: GEOCHEMICAL ANALYSES

Sample	LC-13-08-01	LC-14-08-01	LC-19-08-01	LC-20-08-01	LC-23-08-01
<i>X-Ray Fluorescence Analyses, wt %</i>					
SiO ₂	46.99	46.71	45.92	46.34	45.48
Al ₂ O ₃	15.35	15.07	13.72	15.22	15.05
TiO ₂	2.56	2.54	2.37	2.63	2.75
FeO	13.73	13.60	14.19	12.36	12.71
MgO	9.01	9.34	10.86	8.71	8.99
CaO	9.29	9.79	8.51	9.60	10.16
Na ₂ O	3.04	2.86	2.61	3.52	3.15
K ₂ O	1.04	0.97	0.84	1.78	1.39
MnO	0.17	0.17	0.17	0.17	0.17
P ₂ O ₅	0.41	0.41	0.49	0.54	0.65
Total	101.60	101.45	99.67	100.87	100.51
<i>X-Ray Fluorescence Analyses, ppm</i>					
Zr	223.80	143.72	132.81	210.28	163.52
Sr	471.17	491.56	481.92	564.23	599.18
Nb	40.93	40.67	38.84	71.70	61.09
Y	19.36	19.42	19.21	20.08	19.77
Rb	14.54	14.56	10.53	29.01	20.18
Cr	276.35	297.22	258.15	296.20	304.44
Ni					
<i>Inductively Coupled Plasma Mass Spectrometry (REE) Analyses, ppm</i>					
La	21.9	20.98	21.96	35.7	30.26
Ce	43.56	41.94	43.79	66.23	60.36
Pr	5.29	5.1	5.31	7.62	7.3
Nd	23.35	22.54	23.32	31.69	31.74
Sm	5.84	5.71	5.77	7.3	7.46
Eu	2.01	2.01	2.09	2.44	2.49
Gd	5.9	5.77	5.65	6.73	6.89
Tb	0.94	0.9	0.9	1.04	1.06
Dy	5.46	5.24	5.12	5.87	5.99
Ho	1.03	0.98	0.97	1.12	1.11
Er	2.57	2.47	2.35	2.79	2.72
Tm	0.34	0.34	0.31	0.37	0.37
Yb	2.02	1.99	1.84	2.22	2.18
Lu	0.3	0.3	0.27	0.34	0.32
Ba	339	361	396	510	433
Th	1.85	1.82	1.57	3.93	2.81
Nb	33.63	32.54	31.28	58.05	50.73
Y	26.42	25.62	24.7	28.51	28.6
Hf	3.4	3.25	3.09	4.98	4.02
Ta	2.14	2.1	1.96	3.6	3.14
U	45	0.48	0.44	0.86	0.76
Pb	1.06	1.07	0.87	1.9	1.37
Rb	17.6	16.1	12.7	36.7	24.7
Cs	0.13	0.12	0.09	0.32	0.21
Sr	568	569	583	676	717
Sc	28.2	27.7	23.4	30	28.8
Zr	128	125	117	204	157
W	37.3	45.1	34.8	34.1	42.8

APPENDIX A: GEOCHEMICAL ANALYSES

Sample	LC-24-08-01	LC-25-08-01	LC-26-08-01	LC-27-08-01	LC-28-08-01
<i>X-Ray Fluorescence Analyses, wt %</i>					
SiO ₂	47.51	47.23	46.38	45.95	46.18
Al ₂ O ₃	16.06	15.21	15.37	14.68	13.29
TiO ₂	2.49	2.71	2.88	2.52	2.41
FeO	12.60	13.20	14.53	13.60	14.39
MgO	7.08	8.36	7.90	9.12	11.29
CaO	8.50	9.19	8.94	9.75	8.58
Na ₂ O	4.00	2.77	2.97	2.54	2.28
K ₂ O	1.99	1.13	1.27	0.97	0.80
MnO	0.19	0.17	0.18	0.17	0.18
P ₂ O ₅	0.82	0.48	0.61	0.40	0.50
Total	101.24	100.46	101.04	99.69	99.90
<i>X-Ray Fluorescence Analyses, ppm</i>					
Zr	233.53	160.45	161.00	132.84	124.54
Sr	757.63	498.16	593.90	458.32	452.45
Nb	74.48	46.44	50.00	41.54	35.59
Y	20.69	19.74	19.60	19.01	19.00
Rb	34.17	17.05	17.76	13.11	10.19
Cr	187.35	221.76	181.67	260.96	259.04
Ni	128.85	151.25	131.41	167.36	339.86
<i>Inductively Coupled Plasma Mass Spectrometry (REE) Analyses, ppm</i>					
La	47.29	24.83	30.82	21.18	21.18
Ce	88.09	48.18	60.48	41.78	42.34
Pr	10.03	5.77	7.26	5.06	5.17
Nd	41.07	25.19	31.15	22.7	22.83
Sm	9.04	6.32	7.41	5.67	5.83
Eu	2.91	2.16	2.55	2	1.99
Gd	7.97	6.2	7.14	5.66	5.61
Tb	1.21	0.97	1.09	0.92	0.87
Dy	6.87	5.7	6.27	5.23	5.09
Ho	1.3	1.06	1.14	0.98	0.93
Er	3.21	2.67	2.84	2.5	2.33
Tm	0.44	0.37	0.39	0.34	0.32
Yb	2.62	2.17	2.2	1.99	1.79
Lu	0.41	0.33	0.34	0.29	0.27
Ba	620	337	497	358	342
Th	4.92	2.5	2.59	1.85	1.5
Nb	66.84	39.1	45.75	32.77	30.9
Y	33.69	27.64	30.2	25.56	24.33
Hf	5.71	4.01	4.1	3.3	3.07
Ta	4.24	2.56	2.93	2.08	1.9
U	1.26	0.75	0.58	0.49	0.47
Pb	2.45	1.41	3.71	1.28	0.85
Rb	41.3	18.4	21.8	16.1	12.4
Cs	0.44	0.71	0.16	0.11	0.08
Sr	908	586	752	565	568
Sc	22.5	26.9	24.4	27.7	22.9
Zr	247	158	161	126	116
W	51.1	48.3	56.4	45	36.8

APPENDIX A: GEOCHEMICAL ANALYSES

Sample	LC-29-08-01	LC-30-08-01	LC-31-08-01	LC-32-08-01
<i>X-Ray Fluorescence Analyses, wt %</i>				
SiO ₂	46.30	46.33	46.16	48.36
Al ₂ O ₃	13.75	13.69	15.81	16.18
TiO ₂	2.42	2.48	2.40	2.41
FeO	14.28	14.31	12.30	12.37
MgO	10.80	11.05	7.06	7.51
CaO	8.90	8.97	9.11	9.16
Na ₂ O	2.20	2.21	3.75	2.61
K ₂ O	0.83	0.81	2.10	1.15
MnO	0.17	0.18	0.21	0.17
P ₂ O ₅	0.47	0.50	0.84	0.47
Total	100.11	100.52	99.74	100.39
<i>X-Ray Fluorescence Analyses, ppm</i>				
Zr	157.16	127.05	256.84	167.67
Sr	460.57	449.95	917.96	507.95
Nb	37.73	37.68	102.66	44.14
Y	19.02	18.98	20.77	19.47
Rb	9.66	7.51	42.35	16.65
Cr	274.11	247.62	264.98	233.89
Ni	320.55	309.65	123.48	165.95
<i>Inductively Coupled Plasma Mass Spectrometry (REE) Analyses, ppm</i>				
La	24.46	21.03	55.46	25.96
Ce	42.15	41.81	104.41	49.43
Pr	5.55	5.08	11.98	5.87
Nd	24.32	22.28	47.71	25.16
Sm	5.92	5.72	9.97	6.34
Eu	2.02	1.97	3.13	2.16
Gd	5.76	5.54	8.43	6.18
Tb	0.91	0.88	1.22	0.98
Dy	5.15	5.07	6.75	5.65
Ho	0.95	0.96	1.25	1.08
Er	2.37	2.34	3.16	2.7
Tm	0.31	0.32	0.43	0.36
Yb	1.78	1.83	2.65	2.18
Lu	0.28	0.27	0.4	0.33
Ba	368	658	814	396
Th	1.55	1.62	6.63	2.84
Nb	30.93	31.06	87.14	36.81
Y	25.32	24.26	32.68	27.05
Hf	3.03	3.08	5.91	4.19
Ta	1.96	1.96	5.68	2.5
U	0.44	0.58	1.71	0.74
Pb	0.67	0.64	2.98	1.47
Rb	12	10.5	50.3	21.2
Cs	0.06	0.07	0.62	0.21
Sr	563	552	1029	608
Sc	22.6	22.7	17.9	21.4
Zr	118	118	258	167
W	34.6	37.6	53.7	38.8

APPENDIX B: ISOTOPE DATA

Sample	LC-01-05-01	LC-02-06-01	LC-03-06-01	LC-04-07-01	LC-05-07-01
<i>Isotope Analyses</i>					
ϵ_{Nd}	5.38	5.2	5.17	5.32	5.24
$^{143}Nd/^{144}Nd$	0.512914	0.512905	0.512903	0.512911	0.512907
$^{87}Sr/^{86}Sr$	0.703666	0.703332	0.703622	0.703338	0.703438
$^{206}Pb/^{204}Pb$	19.23	19.466	19.309	19.387	19.388
$^{207}Pb/^{204}Pb$	15.637	15.616	15.702	15.59	15.601
$^{208}Pb/^{204}Pb$	38.703	38.952	38.846	38.845	38.851

Sample	LC-06-07-01	LC-07-07-01	LC-09-08-01	LC-10-08-01	LC-12-08-01
<i>Isotope Analyses</i>					
ϵ_{Nd}	4.97	5.24		4.97	
$^{143}Nd/^{144}Nd$	0.512893	0.512907		0.512893	
$^{87}Sr/^{86}Sr$	0.703721	0.70338		0.703372	
$^{206}Pb/^{204}Pb$	19.212	19.4		19.449	
$^{207}Pb/^{204}Pb$	15.627	15.596		15.584	
$^{208}Pb/^{204}Pb$	38.668	38.825		38.866	

Sample	LC-13-08-01	LC-14-08-01	LC-19-08-01	LC-20-08-01	LC-23-08-01
<i>Isotope Analyses</i>					
ϵ_{Nd}	5.38	5.34		5.56	5.5
$^{143}Nd/^{144}Nd$	0.512914	0.512912		0.512923	0.51292
$^{87}Sr/^{86}Sr$	0.703274	0.703337		0.703355	0.703535
$^{206}Pb/^{204}Pb$	19.369			19.418	19.171
$^{207}Pb/^{204}Pb$	15.548			15.584	15.58
$^{208}Pb/^{204}Pb$	38.735			38.749	38.543

Sample	LC-24-08-01	LC-25-08-01	LC-26-08-01	LC-27-08-01	LC-28-08-01
<i>Isotope Analyses</i>					
ϵ_{Nd}					5.5
$^{143}Nd/^{144}Nd$					0.51292
$^{87}Sr/^{86}Sr$					0.703374
$^{206}Pb/^{204}Pb$					19.499
$^{207}Pb/^{204}Pb$					15.603
$^{208}Pb/^{204}Pb$					38.876

Sample	LC-29-08-01	LC-30-08-01	LC-31-08-01	LC-32-08-01
<i>Isotope Analyses</i>				
ϵ_{Nd}				5.15
$^{143}Nd/^{144}Nd$				0.512902
$^{87}Sr/^{86}Sr$				0.703446
$^{206}Pb/^{204}Pb$				19.458
$^{207}Pb/^{204}Pb$				15.607
$^{208}Pb/^{204}Pb$				38.925

APPENDIX C

PETROGRAPHY

All descriptions are from visual estimates.

F-3 Basalt Flow: The F-3 basalt flow is characterized by a fine grained matrix with a moderate (30%) abundance of phenocrysts. The F-3 basalt flow contains 63% plagioclase, 20% olivine, 15% clinopyroxene and 2% ilmenite. Plagioclase consists of euhedral to subhedral laths. Plagioclase laths are euhedral to subhedral and exhibit albite twinning with no noticeable zoning. Some laths have slightly resorbed rims. Olivine phenocrysts are subhedral moderately to highly fractured. Most olivine phenocrysts have resorbed rims and some phenocrysts are heavily pitted. Clinopyroxene occurs as twinned and zoned subhedral grains. Clinopyroxene phenocrysts are light yellow-brown in color under plain polarized light and some are highly fractured. Clinopyroxene and olivine glomerocrysts also occur in the F-3 flow. A large (4.3 mm) highly resorbed anorthoclase xenocryst exhibiting carlsbad twinning is also present. The matrix of the F-3 flow contains euhedral plagioclase laths with subhedral olivine, glass and ilmenite.

Northeast Finger Basalt Flow: The Northeast Finger basalt flow is characterized by the large abundance of ilmenite (9%), and a coarser grained matrix than the other basalt flows (see Table 4). This flow contains 25% phenocrysts of 66% plagioclase, 15% olivine, 10% clinopyroxene and 9% ilmenite. The plagioclase consists of subhedral to anhedral zoned laths. The plagioclase laths have highly resorbed rims, and sieve texture.

The olivine phenocrysts are anhedral, highly fractured with resorbed rims with iddingsite occurring along fractures and replacing the rims of olivine phenocrysts. The thin section contains some rare olivine-plagioclase glomerocrysts. Clinopyroxene occurs as anhedral phenocrysts with mottled, fractured grains, light yellow-brown in color under plain polarized light and highly altered rims. A large (2.5 mm) xenocryst of anorthoclase is present in the thin section. This anorthoclase xenocryst is highly resorbed and has pronounced sieve texture. The matrix consists mainly of ilmenite, subhedral laths of plagioclase and highly altered anhedral phenocrysts of olivine.

Central Basalt Flow: The Central basalt flow is characterized by 40% phenocrysts of large (0.5-1.3 mm) plagioclase phenocrysts (82%), 10% olivine, 5% clinopyroxene, and a moderate amount of ilmenite (3%). The plagioclase consists of two distinct types of grains. The first plagioclase group is large (0.6-0.9 mm) euhedral laths with albite twinning and zoning. Plagioclase is commonly dusted with ilmenite. The second group contains euhedral to subhedral phenocrysts showing sieve texture and zoning. Most plagioclase have resorbed rims with some phenocrysts having highly resorbed rims. Olivine phenocrysts are subhedral, and moderately to highly fractured with rims and fractures altered to iddingsite. One olivine xenocryst, 5.0 mm in size, is highly fractured, highly resorbed, and has ilmenite inclusions. The clinopyroxene grains are anhedral to subhedral, light yellow in color under plain polarized light, with some phenocrysts twinned. The clinopyroxene grains have resorbed rims and mottled textures. Scattered anorthoclase and olivine xenocrysts occur in the Central Flow Basalt. The matrix consists of mainly oxides with some glass.

Tower Road Basalt Flow: Tower Road basalt flow is characterized by the large size (0.5-1.8 mm) and great abundance (50%) of phenocrysts of plagioclase (72%), olivine (20%) and clinopyroxene (5%). There are two types of plagioclase in the Tower Road basalt flow. The first are euhedral to subhedral laths with albite twinning and zoning. Some of these laths are fractured. The second group consists of subhedral phenocrysts with twinning, compositional zoning and resorbed rims. Olivine is subhedral to anhedral phenocrysts and highly fractured. The olivine rims and fractures are mostly altered to iddingsite. The clinopyroxene phenocrysts are subhedral, fractured and have resorbed rims. The matrix of this flow contains ilmenite, euhedral plagioclase laths, anhedral clinopyroxene and subhedral olivine.

Huge Cone Basalt Flow: The Huge Cone basalt flow is characterized by 30% phenocrysts with large (1.8-2.3 mm) olivine phenocrysts (35%), a small amount of ilmenite (<1%) with 54% plagioclase and 10% clinopyroxene. The plagioclase consists of euhedral laths with albite twinning and zoning. Another plagioclase group is composed of euhedral to subhedral phenocrysts, some very large in size (1.8-2.3 mm megacrysts). These plagioclase phenocrysts have resorbed rims and slight sieve texture. The olivines in the Huge Cone basalt flow are subhedral megacrysts (2.5-5.0 mm), moderately to highly fractured, with resorbed rims altered to iddingsite. The clinopyroxene in this flow are subhedral to anhedral, moderately fractured with resorbed rims. A gabbro xenolith (3.0 x 4.0 mm) contains intergrown clinopyroxene and plagioclase. The matrix is made of euhedral to subhedral plagioclase laths, anhedral olivine and subhedral to anhedral clinopyroxene grains.

F-2 Basalt Flow: The F-2 basalt flow has 25% phenocrysts and is characterized by a more coarse grained matrix than all the other thin sections (see Table 4), small (0.3-0.8 mm) plagioclase phenocrysts (56%), moderate sized (0.8-1.5 mm) clinopyroxene phenocrysts (40%), ilmenite (1%) and a small amount (3%) of olivine. There are three types of plagioclase in the flow. The first are small 0.3-0.8 mm euhedral to subhedral plagioclase laths with albite twinning and zoning and some swallowtailed grains. The second group is also small in size (0.3-0.8 mm), euhedral to subhedral phenocrysts with twinning and zoning. The third group consists of larger 0.8-1.3 mm subhedral phenocrysts with twinning and zoning. This group has resorbed rims, sieve texture and slightly altered rims. Olivine is rare (3%), and are small 0.1-0.4 mm subhedral to anhedral highly fractured grains with resorbed rims and altered edges and fractures. The clinopyroxene are anhedral megacrysts (1.3-2.3 mm) highly fractured, resorbed and altered rims and mostly resorbed cores. The matrix consists of glass, euhedral plagioclase microlaths, and subhedral to anhedral clinopyroxene with highly fractured and resorbed rims. The matrix also contains some ilmenite and traces of subhedral to anhedral olivine with highly fractured surfaces and resorbed rims.

F-1 Basalt Flow: The F-1 basalt flow has 30% phenocrysts and is characterized by (0.1 mm) ilmenite grains (2%) larger than the other thin sections, larger (1.3 mm) plagioclase (68%) and olivine (1.3-3.8 mm) pheno/megacrysts (30%) as well as the absence of clinopyroxene. Most phenocrysts are highly fractured. The plagioclase consists of two groups. The first is euhedral to subhedral laths with albite twinning and zoning. Some resorbed rims were observed. The second group is subhedral phenocrysts with compositional zoning.

Some phenocrysts are twinned with moderately to highly resorbed rims and sieve texture. The olivine is large 1.3-3.8 mm subhedral to anhedral phenocrysts with moderately to highly fractured surfaces, resorbed rims and iddingsite on rims and fractures. The matrix is composed of subhedral plagioclase laths, ilmenite, and subhedral to anhedral olivine.

Black Rock Basalt Flow: The Black Rock basalt flow is characterized by very fine grained matrix and few phenocrysts (10%). Of the total phenocrysts the flow contains 68% plagioclase, 10% olivine, 20% clinopyroxene and 2% ilmenite. The plagioclase grains are small (0.1-0.3 mm) subhedral to anhedral phenocrysts with resorbed rims and moderately fractured surfaces. The olivine in this flow is also small (0.3-0.8 mm).

Olivine is subhedral to anhedral, highly fractured with resorbed rims. The rims and fractures are altered to iddingsite. The clinopyroxene are also small (0.3-0.8 mm) anhedral phenocrysts, highly fractured with resorbed rims. One large 5.0 mm megacryst is present and also has highly fractured surfaces and resorbed rims. The matrix of this flow is primarily glass with euhedral plagioclase laths and subhedral clinopyroxene.

Three Cones Basalt Flow: The Three Cones basalt flow has 20% phenocrysts and is characterized by the large amount of ilmenite (6%), the alteration of most grains, and exsolution lamellae in anorthoclase xenocrysts (see Table 4). Of the total phenocrysts the flow contains 74% plagioclase, 5% olivine, 15% clinopyroxene and 6% ilmenite. The plagioclase is primarily small 0.3-0.8 mm subhedral phenocrysts with twinning and some small 0.3-0.5 mm twinned euhedral laths. The larger (0.8-1.3 mm) plagioclase phenocrysts are subhedral, highly twinned, with fractured surfaces and resorbed rims. Olivines are small (0.3-0.8 mm) subhedral to anhedral phenocrysts, moderately fractured with resorbed rims and altered edges.

The clinopyroxene are subhedral to anhedral phenocrysts, moderately to highly fractured with resorbed rims. Anorthoclase xenocrysts are present and are highly resorbed, twinned and have exsolution lamellae present. The matrix is intensely permeated with ilmenite. The matrix contains small euhedral plagioclase phenocrysts, anhedral clinopyroxene, euhedral to subhedral olivine, ilmenite and 5% glass. Most matrix grains are highly fractured and have resorbed rims.

APPENDIX D - MODEL DATA - FRACTIONAL MELTING WITH PARTIAL MELTING OF RESIDUUM

Fractional Melting

Starting Material = <i>OIB Peridotite</i>				Amount Partial Melting = 0.0419					
Element	ppm	Mineral	Norm	Mineral	Norm				
La	2.076	Ol	0.8	Ol	0.8				
Ce	4.175	Cpx	0.2	Cpx	0.2				
Nd	2.667								
Sm	0.577								

Bulk solid-liquid distribution coefficients

D ⁰	La	0.01396
D ⁰	Ce	0.02
D ⁰	Nd	0.0368
D ⁰	Sm	0.02104

Distribution Coefficient of melt mode

P	La	0.01396
P	Ce	0.02
P	Nd	0.0368
P	Sm	0.02104

Concentration in residual solid

C _{sol}	La	0.101
C _{sol}	Ce	0.5126107
C _{sol}	Nd	0.8699053
C _{sol}	Sm	0.0787499

Concentration in aggregated liquid

C _{liq}	La	47.237605	<i>Actual Values</i>	47.46
C _{liq}	Ce	87.92047		91.44
C _{liq}	Nd	43.759994		43.97
C _{liq}	Sm	11.970161		9.39

To Represent Sample LC-01-05-01 (Enriched)

Fractional Melting

Starting Material = LC-01-05-01				Amount Partial Melting = 0.04					
<u>Element ppm</u>		<u>Mineral Norm</u>		<u>Mineral Norm</u>					
La	0.101	Ol	0.8	Ol	0.8				
Ce	0.5126107	Cpx	0.2	Cpx	0.2				
Nd	0.8699053								
Sm	0.0787499								
				<u>Mineral</u>	<u>Element</u>	<u>DC</u>	<u>Mineral</u>	<u>Element</u>	<u>DC</u>
				Ol	La	0.0002	Cpx	La	0.069
				Ol	Ce	0.0005	Cpx	Ce	0.098
				Ol	Nd	0.001	Cpx	Nd	0.18
				Ol	Sm	0.0013	Cpx	Sm	0.1

Bulk solid-liquid distribution coefficients

D ⁰	La	0.01396
D ⁰	Ce	0.02
D ⁰	Nd	0.0368
D ⁰	Sm	0.02104

Distribution Coefficient of melt mode

P	La	0.01396
P	Ce	0.02
P	Nd	0.0368
P	Sm	0.02104

Concentration in residual solid

C _{sol}	La	0.006
C _{sol}	Ce	0.069355
C _{sol}	Nd	0.2988414
C _{sol}	Sm	0.0117857

Concentration in aggregated liquid

C _{liq}	La	2.3888035	<i>Actual Values</i>	21.03
C _{liq}	Ce	11.150746		41.81
C _{liq}	Nd	14.575438		22.28
C _{liq}	Sm	1.6858889		5.72

To Represent Sample LC-30-08-01 (Depleted)

APPENDIX D - MODEL DATA - FRACTIONAL MELTING OF OIB PERIDOTITE TO YIELD ENRICHED AND DEPLETED GROUPS

Fractional Melting

Starting Material = OIB Peridotite				Amount Partial Melting = 0.0419							
<u>Element</u> <u>ppm</u>		<u>Mineral</u> <u>Norm</u>		<u>Mineral</u> <u>Norm</u>							
La	2.076	Ol	0.8	Ol	0.8						
Ce	4.175	Cpx	0.2	Cpx	0.2						
Nd	2.667										
Sm	0.577										
						<u>Mineral</u>	<u>Element</u>	<u>DC</u>	<u>Mineral</u>	<u>Element</u>	<u>DC</u>
						Ol	La	0.0002	Cpx	La	0.069
						Ol	Ce	0.0005	Cpx	Ce	0.098
						Ol	Nd	0.001	Cpx	Nd	0.18
						Ol	Sm	0.0013	Cpx	Sm	0.1

Bulk solid-liquid distribution coefficients

D^0	La	0.01396
D^0	Ce	0.02
D^0	Nd	0.0368
D^0	Sm	0.02104

Distribution Coefficient of melt mode

P	La	0.01396
P	Ce	0.02
P	Nd	0.0368
P	Sm	0.02104

Concentration in residual solid

C_{sol}	La	0.101
C_{sol}	Ce	0.5126107
C_{sol}	Nd	0.8699053
C_{sol}	Sm	0.0787499

Concentration in aggregated liquid

C_{liq}	La	47.237605	Actual Values	47.46
C_{liq}	Ce	87.92047		91.44
C_{liq}	Nd	43.759994		43.97
C_{liq}	Sm	11.970161		9.39

To Represent Sample LC-01-05-01 (Enriched)

Fractional Melting

Starting Material = OIB Peridotite				Amount Partial Melting = 0.099							
Element	ppm	Mineral	Norm	Mineral	Norm						
La	2.076	Ol	0.8	Ol	0.8						
Ce	4.175	Cpx	0.2	Cpx	0.2						
Nd	2.667										
Sm	0.577										
				Mineral	Element	DC	Mineral	Element	DC		
				Ol	La	0.0002	Cpx	La	0.069		
				Ol	Ce	0.0005	Cpx	Ce	0.098		
				Ol	Nd	0.001	Cpx	Nd	0.18		
				Ol	Sm	0.0013	Cpx	Sm	0.1		

Bulk solid-liquid distribution coefficients

D^0	La	0.01396
D^0	Ce	0.02
D^0	Nd	0.0368
D^0	Sm	0.02104

Distribution Coefficient of melt mode

P	La	0.01396
P	Ce	0.02
P	Nd	0.0368
P	Sm	0.02104

Concentration in residual solid

C_{sol}	La	0.001
C_{sol}	Ce	0.0252448
C_{sol}	Nd	0.1741781
C_{sol}	Sm	0.0045143

Concentration in aggregated liquid

C_{liq}	La	20.957719	Actual Values	21.03
C_{liq}	Ce	41.941964		41.81
C_{liq}	Nd	25.354197		22.28
C_{liq}	Sm	5.7871984		5.72

To Represent Sample LC-30-08-01 (Depleted)

APPENDIX E: SAMPLE LOCATION

Sample	LC-01-05-01	LC-02-06-01	LC-03-06-01	LC-04-07-01	LC-05-07-01
Latitude	N 38 33.15	N 38 30.42	N 38 29.20	N 38 27.32	N 38 33.27
Longitude	W 115 58.85	W 115 53.40	W 116 0.82	W 115 58.44	W 115 56.55
Elevation	1838 m	1784 m	1746 m	1781 m	1902 m
Description	F-1	NE Finger B1	Black Rock	East Island	F-2
Sample	LC-06-07-01	LC-07-07-01	LC-08-08-01	LC-9-08-01	LC-10-08-01
Latitude	N 38 32.97	N 38 33.16	N 38 30.42	N 38 30.39	N 38 29.95
Longitude	W 115 56.19	W 115 56.21	W 115 53.40	W 115 53.02	W 115 55.26
Elevation	1920 m	1876 m	1784 m	1751 m	1849 m
Description	F-3	F-3	NE Finger B1	NE Finger B1	Central B1
Sample	LC-11-08-01	LC-12-08-01	LC-13-08-01	LC-14-08-01	LC-15-08-01
Latitude	N 38 29.95	N 38 30.00	N 38 32.07	N 38 31.95	N 38 33.06
Longitude	W 115 55.26	W 115 55.57	W 115 54.58	W 115 54.78	W 115 55.75
Elevation	1849 m	1848 m	1915 m	1938 m	1925 m
Description	Central B1	Central B1	B1	B1	Huge Cone B1
Sample	LC-16-08-01	LC-17-08-01	LC-18-08-01	LC-19-08-01	LC-20-08-01
Latitude	N 38 33.27	N 38 32.97	N 38 33.31	N 38 33.31	N 38 31.54
Longitude	W 115 56.55	W 115 56.19	W 115 56.19	W 115 56.19	W 115 59.69
Elevation	1902 m	1920 m	1897 m	1897 m	1780 m
Description	F-2	F-3	F-1	F-1	F-1
Sample	LC-21-08-01	LC-22-08-01	LC-23-08-01	LC-24-08-01	LC-25-08-01
Latitude	N 38 29.20	N 38 27.69	N 38 24.07	N 38 33.35	N 38 30.35
Longitude	W 116 0.82	W 115 59.33	W 116 4.16	W 115 56.41	W 115 52.66
Elevation	1746 m	1451 m	1747 m	1865 m	1649 m
Description	Black Rock	3-Cones	Lunar Crater	F-3	NE Finger B1
Sample	LC-26-08-01	LC-27-08-01	LC-28-08-01	LC-29-08-01	LC-30-08-01
Latitude	N 38 30.13	N 38 31.77	N 38 33.02	N 38 33.26	N 38 32.77
Longitude	W 115 55.79	W 115 54.98	W 115 56.04	W 115 57.13	W 115 59.23
Elevation	1844 m	1969 m	1951 m	1844 m	1807 m
Description	Central B1	B1	Huge Cone B1	F-2	F-1
Sample	LC-31-08-01	LC-32-08-01			
Latitude	N 38 29.39	N 38 28.00			
Longitude	W 116 0.30	W 115 59.50			
Elevation	1780 m	1852 m			
Description	Black Rock	3-Cones			

APPENDIX F: GEOCHRONOLOGY

Nevada Isotope Geochronology Laboratory – Description and Procedures

Samples analyzed by the $^{40}\text{Ar}/^{39}\text{Ar}$ method at the University of Nevada Las Vegas were wrapped in Al foil and stacked in 6 mm inside diameter sealed fused silica tubes. Individual packets averaged 3 mm thick and neutron fluence monitors (FC-2, Fish Canyon Tuff sanidine) were placed every 5 to 10 mm along the tube. Synthetic K-glass and optical grade CaF_2 were included in the irradiation packages to monitor neutron induced argon interferences from K and Ca. Loaded tubes were packed in an Al container for irradiation. Samples irradiated at the Oregon State University Radiation Center were in-core for 7 hours in the Cadmium-Lined, In-Core Irradiation Tube (CLICIT) of the 1 MW TRIGA type reactor. Correction factors for interfering neutron reactions on K and Ca were determined by repeated analysis of K-glass and CaF_2 fragments. Measures $(^{40}\text{Ar}/^{39}\text{Ar})_{\text{K}}$ values were $1.32 (\pm 89 \%)$. Ca correction factors were $(^{36}\text{Ar}/^{37}\text{Ar})_{\text{Ca}} = 2.77 (\pm 2.28 \%)$ and $(^{39}\text{Ar}/^{37}\text{Ar})_{\text{Ca}} = 7.44 (\pm 0.37 \%)$. J factors were determined by fusion of 4 to 5 individual crystals of neutron fluence monitors which gave reproducibility's of 0.03% to 0.19% at each standard position. Variation in neutron flux along the 100 mm length of the irradiation tubes was $<4\%$. An error of J of 0.5% was used in age calculations. No significant neutron flux gradients were present within individual packets of crystals as indicated by the excellent reproducibility of the single crystal flux monitor fusions.

Irradiated crystals together with CaF_2 and K-glass fragments were placed in a Cu sample tray in an high vacuum extraction line and were fused using a 20 W CO_2 laser. Sample viewing during laser fusion was by a video camera system and positioning was via a motorized sample stage. Samples analyzed by the furnace step heating method utilized a double vacuum resistance furnace similar to the Staudacher et al. (1978) design. Reactive gases were removed by a single MAP and two GP-50 SAES getters prior to being admitted to a MAP 215-50 mass spectrometer by expansion. The relative volumes of the extraction line and mass spectrometer allow 80% of the gas to be admitted to the mass spectrometer for laser fusion analyses and 76% for furnace heating analysis. Peak intensities were measured using a Balzers electron multiplier by peak hopping through 7 cycles; initial peak heights were determined by linear regression to the time of gas admission. Mass spectrometer discrimination and sensitivity was monitored by repeated analysis of atmospheric argon aliquots from an on-line pipette system. Measured $^{40}\text{Ar}/^{39}\text{Ar}$ ratios were $292.94 \pm 0.77\%$ during this work, thus a discrimination correction of 1.00876 (4 AMU) was applied to measured isotope ratios. The sensitivity of the mass spectrometer was $\sim 6 \times 10^{-17} \text{ mol mV}^{-1}$ with the multiplier operated at a gain of 30 over the Faraday. Line blanks averaged 1.98 mV for mass 40 and 0.01 mV for mass 36 for laser fusion analyses and 10.86 mV for mass 40 and 0.04 mV for mass 36 for furnace heating analyses. Discrimination, sensitivity, and blanks were relatively constant over the period of data collection. Computer automated operation of the sample stage, laser, extraction line and mass spectrometer as well as final data reduction and age calculations were done using LabSPEC software written by B. Idleman (Lehigh University). An age of 27.9 Ma (Steven et al., 1967; Cebula et al., 1986) was used for the Fish Canyon Tuff sanidine flux monitor in calculating ages for samples.

For $^{40}\text{Ar}/^{39}\text{Ar}$ analyses a plateau segment consists of 3 or more contiguous gas fractions having analytically indistinguishable ages (i.e. all plateau steps overlap in age at $\pm 2\sigma$ analytical error) and comprising a significant portion of the total gas released (typically $>50\%$). Total gas (integrated) ages are calculated by weighting the amount of ^{39}Ar released, whereas plateau ages are weighted by the inverse of the variance. For each sample inverse isochron diagrams are examined to check for the effects of excess argon. Reliable isochrons are based on the MSWD criteria of Wendt and Carl (1991) and, as for plateaus, must comprise contiguous steps and a significant fraction of the total gas released. All analytical data are reported at the confidence level of 1σ (standard deviation)

APPENDIX F: GEOCHRONOLOGY

Stickney-UNLV, LC190801, basalt, 22.42 mg, J = 0.0019015 ± 0.05%

E-I Flow

4 amu discrimination = 1.00876 ± 0.77%, 40/39K = 0.0132 ± 89.00%, 36/37Ca = 0.0002770 ± 2.28%, 39/37Ca = 0.0007435 ± 0.37%

step	T (°C)	t (min)	36Ar	37Ar	38Ar	39Ar	40Ar	%40Ar*	%39Ar rlsd	Ca/K	40Ar*/39ArK	Age (Ma)	1σ d
1	550	12	3.666	19.599	1.748	65.492	1108.386	3.5	12.2	2.233837671	0.5825	2.00	0.45
2	600	12	1.19	20.395	0.706	35.749	363.624	5.4	6.7	4.261184818	0.5340	1.83	0.33
3	650	12	1.01	31.523	0.80	46.334	308.22	6.4	8.6	5.08282903	0.4147	1.42	0.18
4	700	12	0.828	41.736	0.72	42.228	248.419	6.5	7.9	7.38905335	0.3666	1.26	0.18
5	755	12	0.769	29.936	0.588	32.481	240.276	9.4	6.1	6.889341677	0.6665	2.29	0.30
6	810	12	0.492	19.834	0.477	27.385	158.05	12.0	5.1	5.411506579	0.6543	2.24	0.24
7	905	12	0.882	26.739	0.637	33.051	271.565	7.2	6.2	6.045941333	0.5740	1.97	0.26
8	1000	12	0.515	25.811	0.442	23.216	155.628	7.1	4.3	8.314124052	0.4471	1.53	0.24
9	1085	12	1.955	113.906	2.369	137.776	599.902	9.3	25.7	6.178651603	0.3989	1.37	0.13
10	1190	12	1.625	404.785	1.623	86.025	420.608	12.7	16.0	35.47513869	0.6157	2.11	0.18
11	1400	12	0.258	34.44	0.143	6.506	72.704	10.8	1.2	39.96254568	0.9827	3.37	0.33
Cumulative %39Ar rlsd=										100	Total gas age =	1.76	0.13
											no plateau		

note: isotope beams in mV rlsd = released, error in age includes 0.5% J error, all errors 1 sigma
(36Ar - 40Ar are measured beam intensities, corrected for decay in age calculations)

Stickney-UNLV, LC170801, basalt, 26.70 mg, J = 0.001904 ± 0.5%

E-I Flow

4 amu discrimination = 1.00876 ± 0.77%, 40/39K = 0.0132 ± 89.00%, 36/37Ca = 0.0002770 ± 2.28%, 39/37Ca = 0.0007435 ± 0.37%

step	T (°C)	t (min)	36Ar	37Ar	38Ar	39Ar	40Ar	%40Ar*	%39Ar rlsd	Ca/K	40Ar*/39ArK	Age (Ma)	1σ d
1	550	12	9.438	30.217	3.767	135.817	2875.07	4.0	10.0	1.621190848	0.8563	2.94	0.65
2	600	12	3.293	26.131	2.164	107.151	990.387	3.1	7.9	1.777121393	0.2836	0.974	0.34
3	650	12	2.623	28.145	1.95	107.742	813.843	6.3	8.0	1.903662858	0.4698	1.61	0.31
4	700	12	1.414	20.471	1.486	91.383	453.947	9.7	6.7	1.632345309	0.4707	1.62	0.19
5	750	12	0.99	17.979	1.262	78.719	305.593	6.2	5.8	1.664288161	0.2327	0.799	0.14
6	800	12	0.683	16.83	1.087	68.971	212.285	7.3	5.1	1.778177148	0.2134	0.733	0.11
7	900	12	1.04	24.217	1.575	95.589	311.023	3.5	7.1	1.846199959	0.1095	0.376	0.09
8	1000	12	3.938	45.681	2.928	149.573	1203.409	4.9	11.0	2.225862245	0.1952	1.36	0.22
9	1100	12	8.623	304.498	8.022	433.958	2551.756	3.9	32.0	5.118351516	0.2277	0.782	0.17
10	1250	12	1.699	486.935	1.577	83.741	441.264	16.3	6.2	42.89696242	0.8493	2.92	0.24
11	1400	12	0.128	11.286	0.044	1.457	44.038	32.4	0.1	57.39044353	6.7334	22.98	0.66
Cumulative %39Ar rlsd=										100	Total gas age =	1.33	0.10
											no plateau		

note: isotope beams in mV rlsd = released, error in age includes 0.5% J error, all errors 1 sigma
(36Ar - 40Ar are measured beam intensities, corrected for decay in age calculations)

Stickney-UNLV, LC120801, basalt, 19.64 mg, J = 0.001898 ± 0.5%

Central Flow

4 amu discrimination = 1.00876 ± 0.77%, 40/39K = 0.0132 ± 89.00%, 36/37Ca = 0.0002770 ± 2.28%, 39/37Ca = 0.0007435 ± 0.37%

step	T (°C)	t (min)	36Ar	37Ar	38Ar	39Ar	40Ar	%40Ar*	%39Ar rlsd	Ca/K	40Ar*/39ArK	Age (Ma)	1σ d
1	550	12	5.521	18.208	2.077	63.96	1673.723	3.6	9.5	2.15169683	0.9380	3.21	0.77
2	615	12	2.261	24.444	1.128	44.985	706.69	7.1	6.7	4.109484808	1.1033	3.77	0.53
3	680	12	1.854	28.749	1.09	53.378	566.996	5.4	7.9	4.073226338	0.5642	1.93	0.29
4	745	12	1.572	27.183	0.902	42.983	468.905	3.1	6.4	4.783782963	0.3322	1.14	0.30
5	815	12	1.508	19.086	0.812	35.857	464.523	5.8	5.3	4.025435107	0.7420	2.54	0.41
6	885	12	1.987	16.871	0.915	34.296	614.783	5.9	5.1	3.719883541	1.0509	3.6	0.54
7	955	12	2.629	20.12	1.09	38.689	797.175	4.0	5.7	3.93278535	0.8070	2.76	0.69
8	1020	12	8.252	40.27	2.954	90.834	2531.76	4.9	13.5	3.352101654	1.3653	4.67	0.74
9	1080	12	10.028	76.842	3.835	128.621	3020.817	3.1	19.1	4.518798891	0.7318	2.50	0.69
10	1190	12	6.939	362.661	3.429	134.143	2060.793	6.1	19.9	20.5473252	0.9441	3.23	0.43
11	1400	12	0.366	33.321	0.159	5.816	111.832	14.0	0.9	43.84608399	2.3820	8.14	0.52
Cumulative %39Ar rlsd=										100	Total gas age =	3.08	0.44
											plateau age =	3.10	0.44
											(steps 5-10)		

note: isotope beams in mV rlsd = released, error in age includes 0.5% J error, all errors 1 sigma
(36Ar - 40Ar are measured beam intensities, corrected for decay in age calculations)

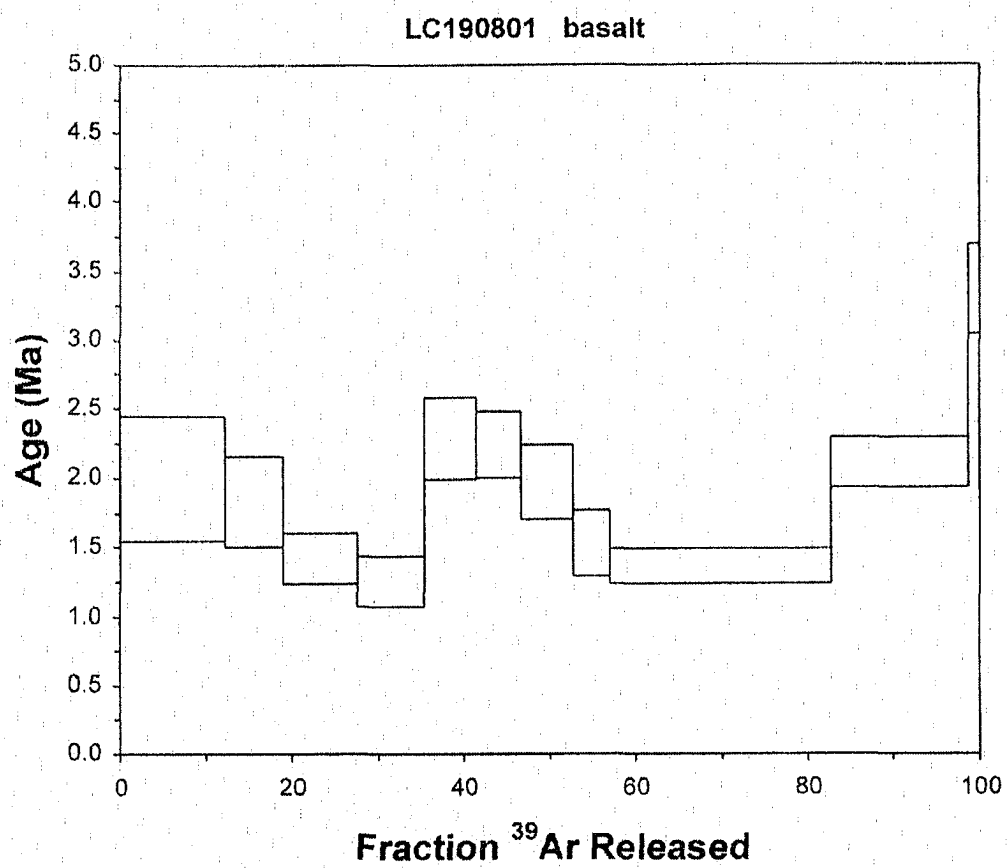
Stickney-UNLV, LC090801, basalt, 19.49 mg, J = 0.0019045 ± 0.5%

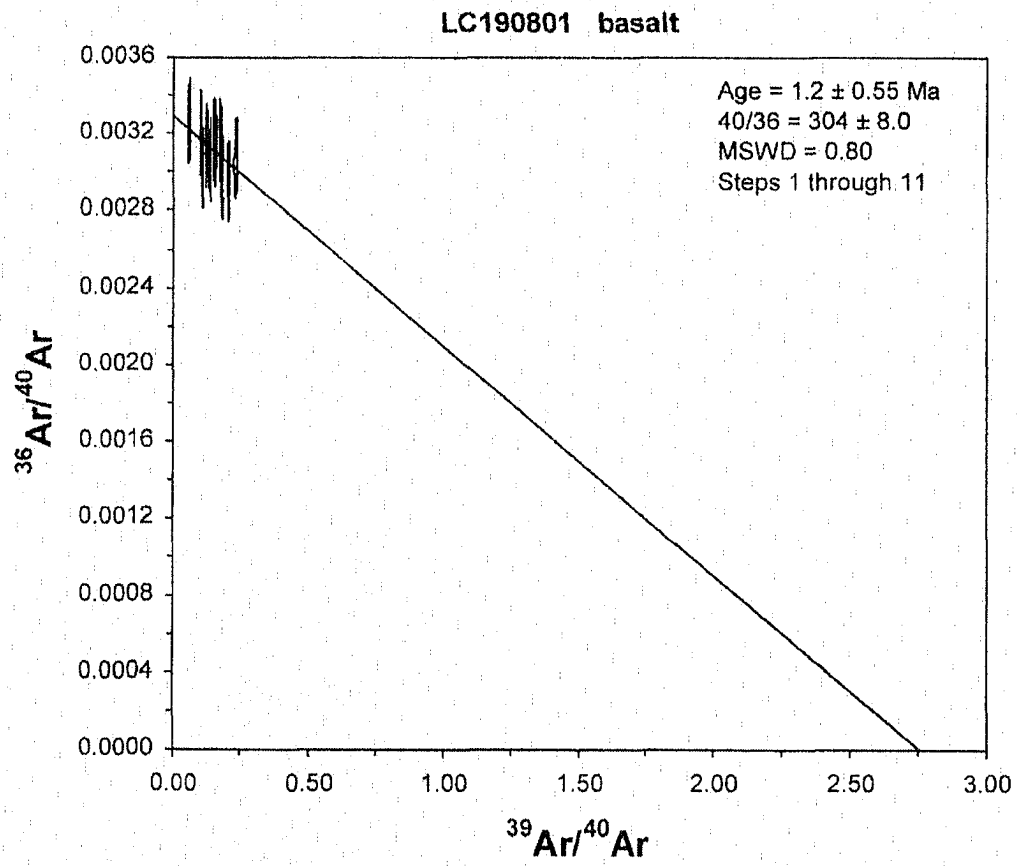
NE Finger

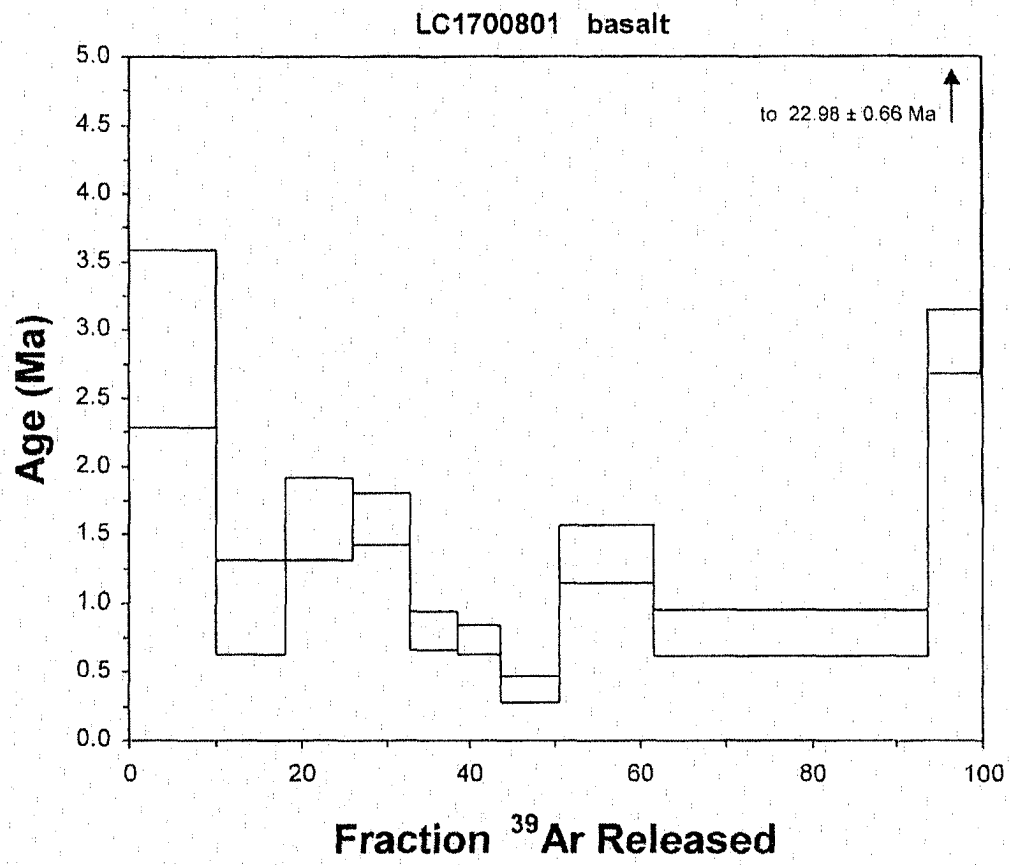
4 amu discrimination = 1.00876 ± 0.77%, 40/39K = 0.0132 ± 89.00%, 36/37Ca = 0.0002770 ± 2.28%, 39/37Ca = 0.0007435 ± 0.37%

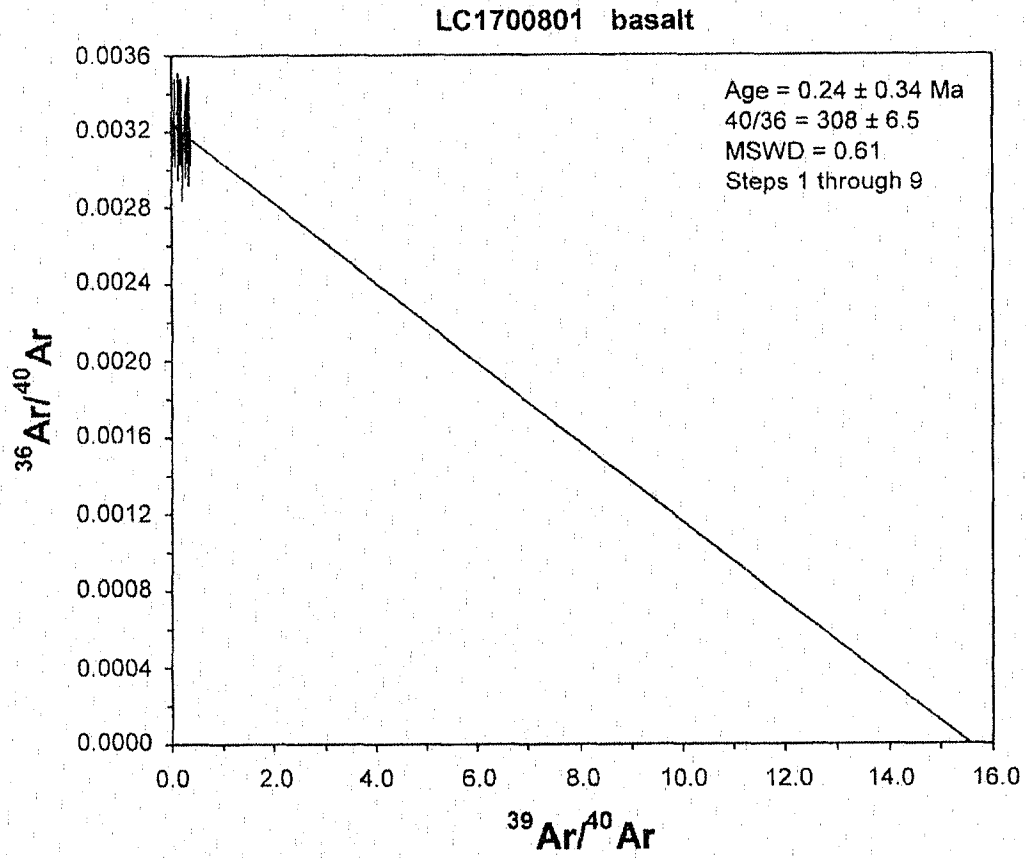
step	T (°C)	t (min)	36Ar	37Ar	38Ar	39Ar	40Ar	%40Ar*	%39Ar rlsd	Ca/K	40Ar*/39ArK	Age (Ma)	1σ d
1	550	12	1.856	17.021	1.134	43.105	598.034	9.8	7.3	2.927363415	1.3344	4.58	0.49
2	600	12	0.528	20.597	0.847	42.644	170.684	12.4	7.2	3.58138174	0.4676	1.61	0.12
3	650	12	0.574	30.042	1.17	70.34	187.677	14.4	11.9	3.166481156	0.3639	1.25	0.13
4	700	12	0.473	30.391	1.31	92.368	174.211	25.2	15.7	2.4388152	0.4499	1.55	0.07
5	755	12	0.435	23.753	1.099	76.371	160.526	24.8	13.0	3.05302937	0.4904	1.68	0.08
6	810	12	0.429	18.237	0.692	46.496	143.493	15.7	7.9	2.907732574	0.4534	1.56	0.11
7	905	12	0.531	22.459	0.72	46.007	172.419	13.0	7.8	3.619729235	0.4621	1.59	0.11
8	1000	12	0.484	20.983	0.61	36.083	157.70	13.5	6.1	4.312856166	0.5559	1.91	0.16
9	1085	12	0.875	36.085	0.841	46.037	280.111	11.7	7.8	5.815884787	0.6920	2.38	0.17
10	1195	12	2.40	391.656	1.501	74.403	637.656	6.1	12.6	39.45256913	0.5221	1.79	0.27
11	1400	12	0.387	67.46	0.263	15.249	112.295	17.0	2.6	33.09360754	1.1042	3.79	0.40
Cumulative %39Ar rlsd=										100	Total gas age =	1.94	0.08
											plateau age =	1.62	0.08
											(steps 4-8)		

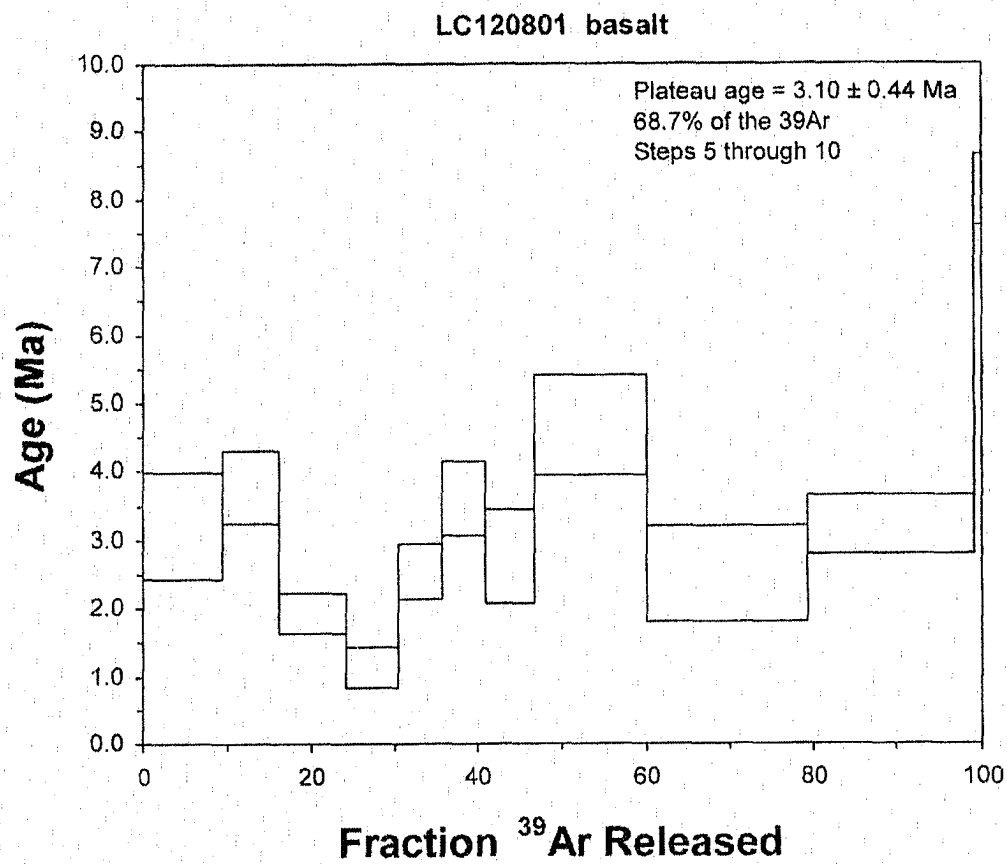
note: isotope beams in mV rlsd = released, error in age includes 0.5% J error, all errors 1 sigma
(36Ar - 40Ar are measured beam intensities, corrected for decay in age calculations)

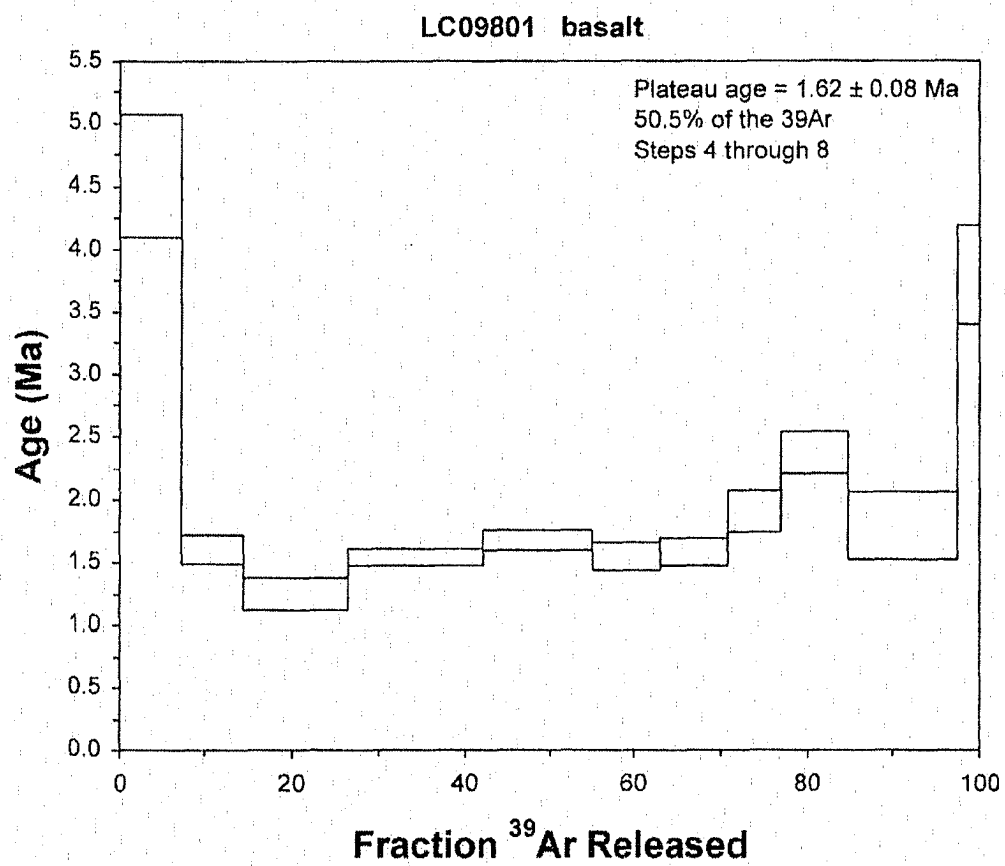


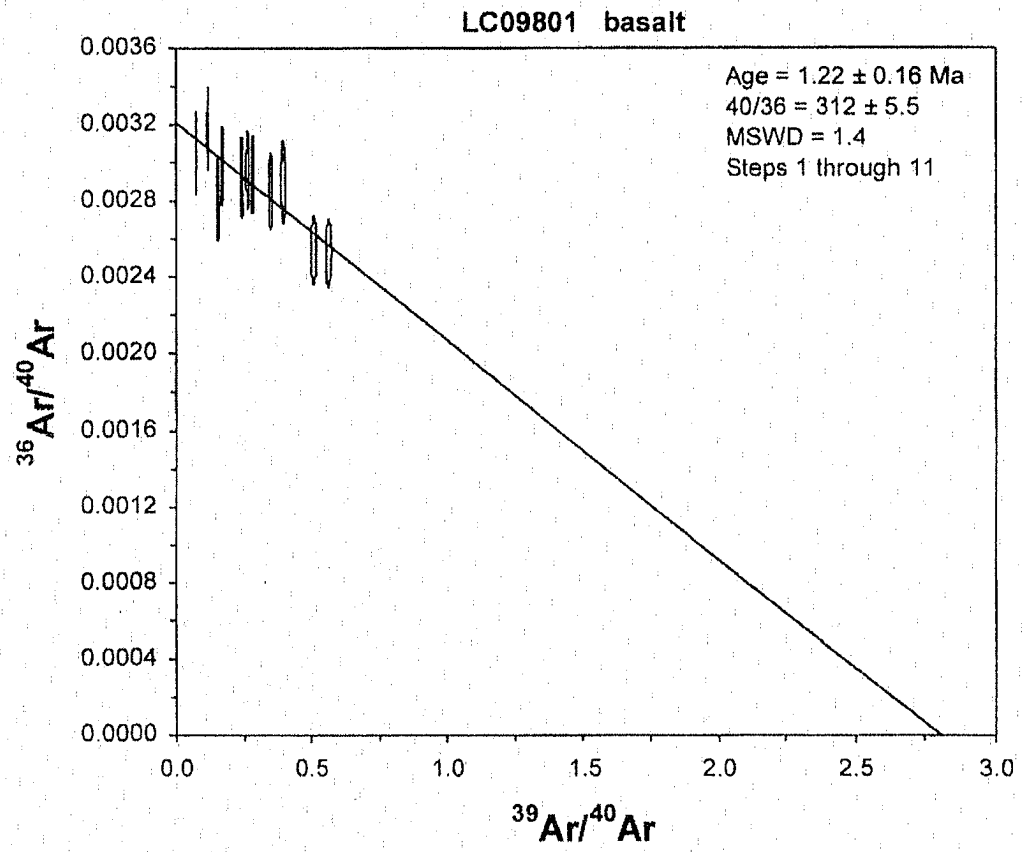












APPENDIX G: ACCURACY AND PRECISION

Primary calibration standards for the Rigaku 3030 X-ray Fluorescence Spectrometer. Standards are United States Geological Survey, National Bureau of Standards and French standards.

Major Elements	Trace Elements
DNC-1	G-2
BHVO-1	W-2
PCC-1	BIR-1
AGV-1	BHVO-1
GS-N	DNC-1
GA	RGM-1
W-2	QLO-1
BR	PCC-1
Sco-1	Sco-1
STM-1	AGV-1
GSP-1	GSP-1
RGM-1	AN-G
QLO-1	DR-N
AL-1	GS-N
	MAG-1
	Mica Mg
	NBS-688

Accuracy for the Rigaku 3030 X-ray Fluorescence Spectrometer using NBS standard NBS-688 (major elements), USGS standard MAG-1 (trace elements) and Rh X-ray tube installed August 1994.

Element	% error
SiO ₂	0.7
Al ₂ O ₃	0.5
TiO ₂	0.7
Fe ₂ O ₃	2.6
MgO	2.4
CaO	1.5
Na ₂ O	0.9
K ₂ O	2.3
MnO	8.2
P ₂ O ₅	18.6
Rb	0.9
Sr	2.1
Zr	1.8
Y	11.2
Nb	13.3
Cr	27.5
Ni	3.5

APPENDIX G : ACCURACY AND PRECISION

Precision for the Rigaku 3030 X-ray Fluorescence Spectrometer. Precision is determined using NBS standard NBS-688 (major elements), USGS standard MAG-1 (trace elements) and Rh X-ray tube installed August 1994.

Element	Published concentration	Mean of 4 replicate analyses	Standard Deviation	uncertainty
SiO ₂	50.36	47.99	0.45	0.9
Al ₂ O ₃	16.37	17.44	0.2	1.2
TiO ₂	0.751	1.16	0.02	1.8
Fe ₂ O ₃	6.8	10.07	0.14	1.3
MgO	3.0	8.66	0.15	1.7
CaO	1.37	11.99	0.11	0.9
Na ₂ O	3.83	2.14	0.06	2.6
K ₂ O	3.55	0.186	0.003	1.4
MnO	0.098	0.153	0.005	3.2
P ₂ O ₅	0.163	0.158	0.018	11.4
Rb	149	150.4	4.33	2.9
Sr	146	143	3.11	2.2
Zr	126	128.3	2.22	1.7
Y	28	31.14	2.65	8.5
Nb	12	13.6	2.44	17.9
Cr	97	70.3	4.57	6.5
Ni	53	51.1	2.39	4.7

APPENDIX G : ACCURACY AND PRECISION

Accuracy for the Inductively Coupled Plasma - Mass Spectrometer (ICP-MS).
USGS standard BHVO-1 was used as a reference.

Element ppm	Published value	WSU ICP- MS value	% error
Ba	139	133	4.32
La	15.8	15.65	0.95
Ce	39	37.07	4.95
Sm	6.2	6.2	0
Eu	2.06	2.12	2.91
Tb	0.96	0.96	0
Yb	2.02	2.02	0
Lu	0.29	0.28	3.45
Hf	4.38	4.34	0.91
Ta	1.23	1.25	1.63
Th	1.08	1.25	15.74

Precision for the Inductively Coupled Plasma - Mass Spectrometer (ICP-MS).

Data reported is from twenty-four replicate analysis of Washington State in-house standards BCR-P.

Element ppm	Mean of 24 rep- licate analysis	Standard deviation	Mean relative % error
Ba	670	13	1.89
La	26.26	0.49	1.86
Ce	51.67	0.62	1.2
Sm	7.03	0.15	2.07
Eu	2.13	0.05	2.48
Tb	1.17	0.01	1.12
Yb	3.36	0.03	0.94
Lu	0.52	0.01	1.9
Hf	4.67	0.07	1.47
Ta	0.82	0.02	2.7
Th	5.13	0.49	9.5

VITA

Graduate College
University of Nevada, Las Vegas

Elizabeth Kay Stickney

Home Address:

9104 Sunnyfield Drive
Las Vegas, NV 89134

Degrees:

Bachelor of Science, Earth Sciences, 1997
University of California at Santa Cruz

Special Awards:

Bernada E. French Scholarship in Geology, 2000

Thesis Title:

The Volcanology and Petrogenesis of the Northern Lunar Crater Volcanic Field,
Nye County, Nevada

Thesis Examination Committee:

Chairperson, Dr. Eugene Smith, Ph. D.
Committee Member, Dr. Michael Wells, Ph. D.
Committee Member, Dr. Terry Spell, Ph. D.
Graduate Faculty Representative, Dr. Chih-Hsiang Ho, Ph. D.

NOTE TO USERS

Oversize maps and charts are microfilmed in sections in the following manner:

LEFT TO RIGHT, TOP TO BOTTOM, WITH SMALL OVERLAPS

This reproduction is the best copy available.

UMI

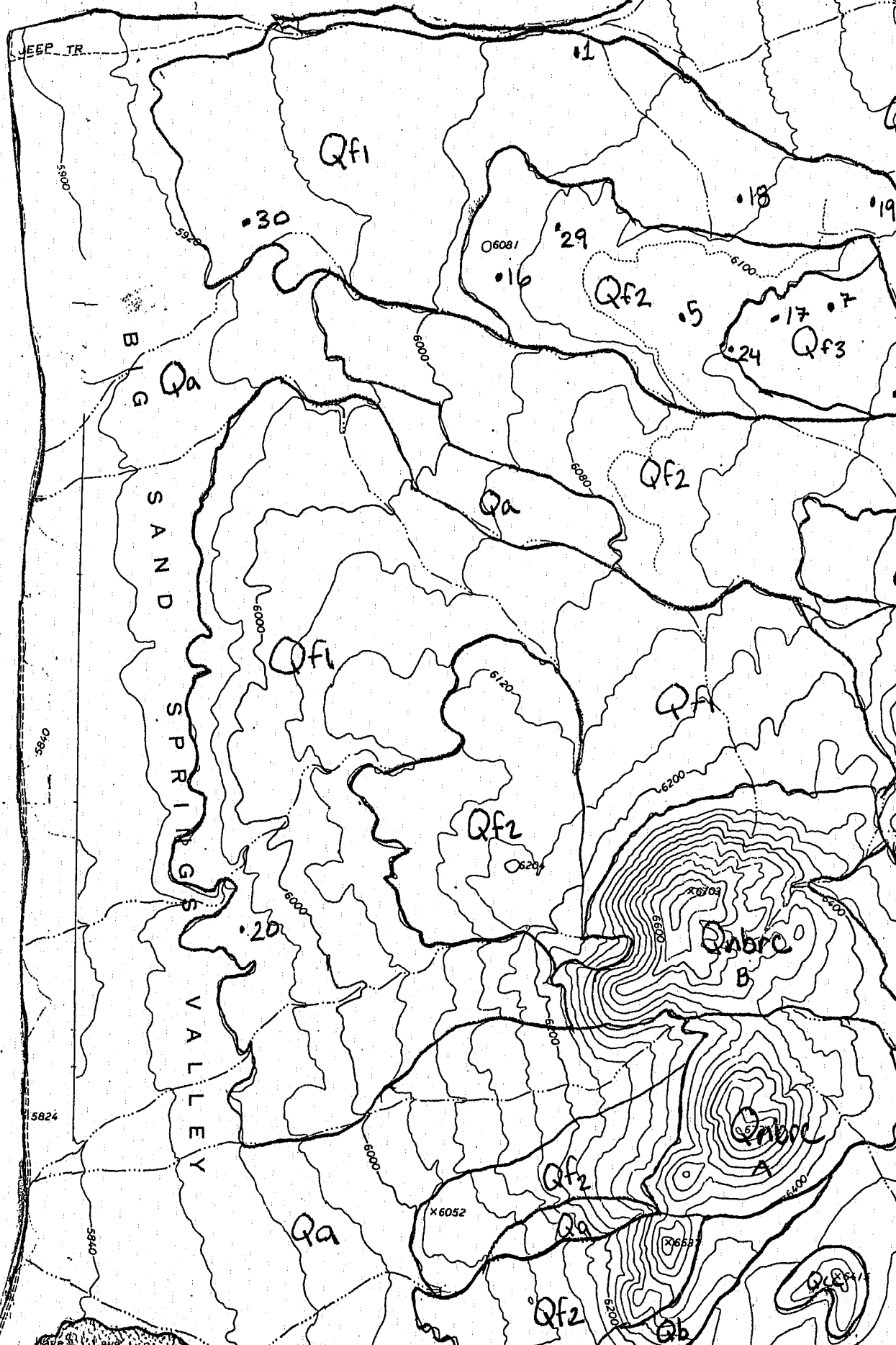
EXPLANATION

Contact

DESCRIPTION OF UNITS

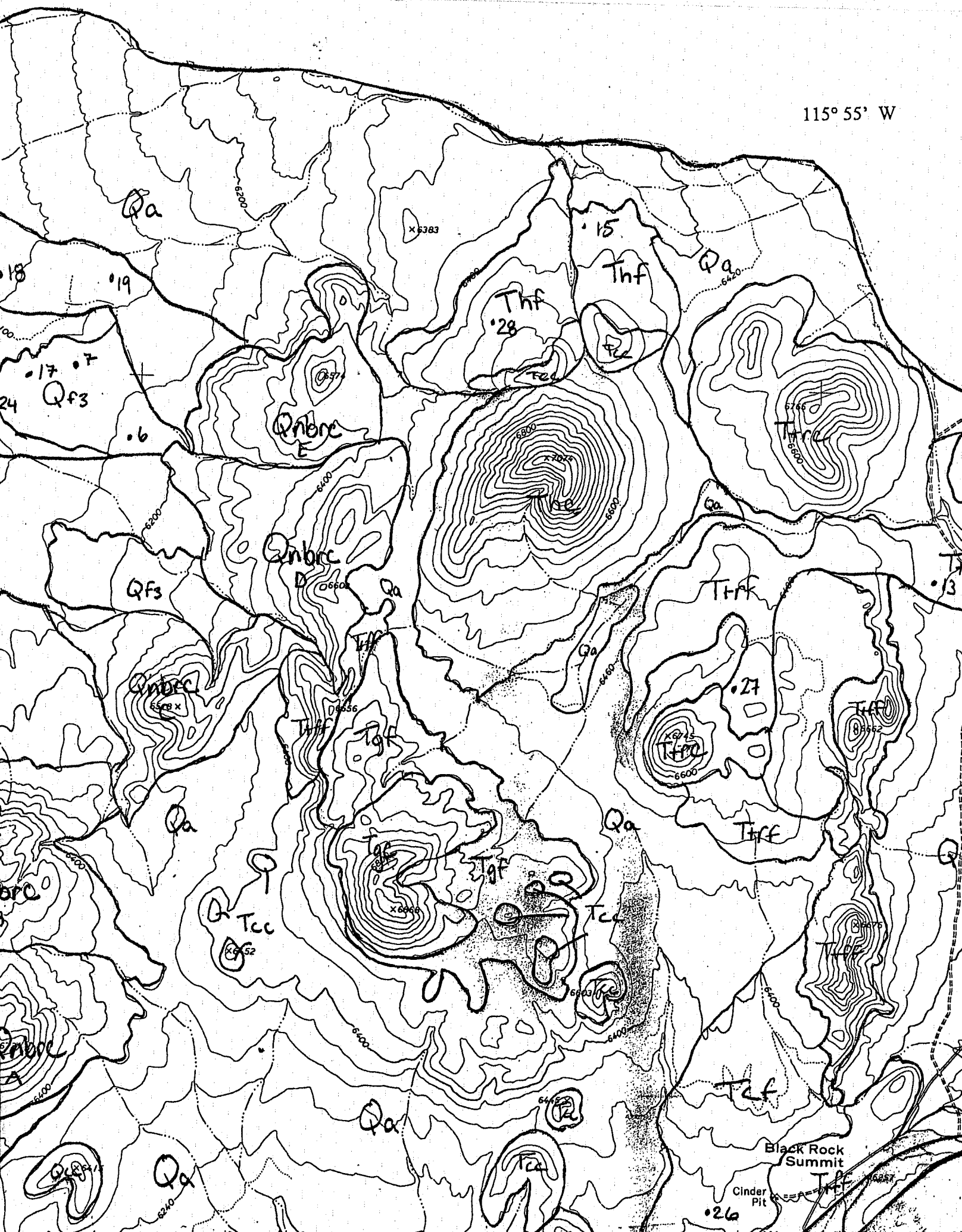
Qa	Alluvium – up to 300 m thick, can include incorporated ash, lappili, agglutinate, Blocks and bombs
Qbf	Basalt – thickness varies
Qcc	Cinder Cone
Qbrc/Qbrf	Black Rock Cone and Black Rock Basalt Flow - 20 ± 9 ka – 4 to 10 m thickness- A'a – xenoliths of lherzolite and dunite – fresh appearance
Qnbrc	North Black Rock Cluster Cones
Qf3	F-3 Basalt Flow - 240 ± 340 ka – 2 m thickness – blocky – desert varnish
Qf2	F-2 Basalt Flow – 1 to 3 m thickness – blocky A'a – xenoliths of rafted tuff – highly altered olivine
Qf1	F-1 Flow Basalt - 1.2 ± 0.6 Ma – 0.5 to 5 m thickness – blocky – xenoliths of rafted tuff – columnar jointing, tumuli
Tbf	Basalt – thickness varies
Tcc	Cinder Cone
Ttc/Ttf	Three-Cones and Three-Cones Basalt Flow – 0.5 to 3 m thickness – blocky A'a
Thc/Thf	Huge Cone and Huge Cone Basalt Flow – 1.5 m thickness – blocky – xenoliths of lherzolite and dunite
Tgc/Tgf	G-Cone and G-Cone Basalt Flow – 1.5 m thickness – blocky – xenoliths of peridotite and dunite
Tnef	Northeast Finger Basalt Flow - 1.22 ± 0.2 Ma – 2 to 20 m thickness – blocky A'a – xenoliths of rafted tuff and dunite – steep $> 40^\circ$ flow fronts , columnar jointing
Tcf	Central Basalt Flow - 3.1 ± 0.4 Ma – 1 to 4 m thickness – blocky - xenoliths of rafted tuff – highly weathered
Ttrc/Ttrf	Tower Road Cone and Tower Road Basalt Flow – 0.5 to 3 m thickness – Blocky to A'a – xenoliths of peridotite – massive overlain by highly vesiculated lava

116° W

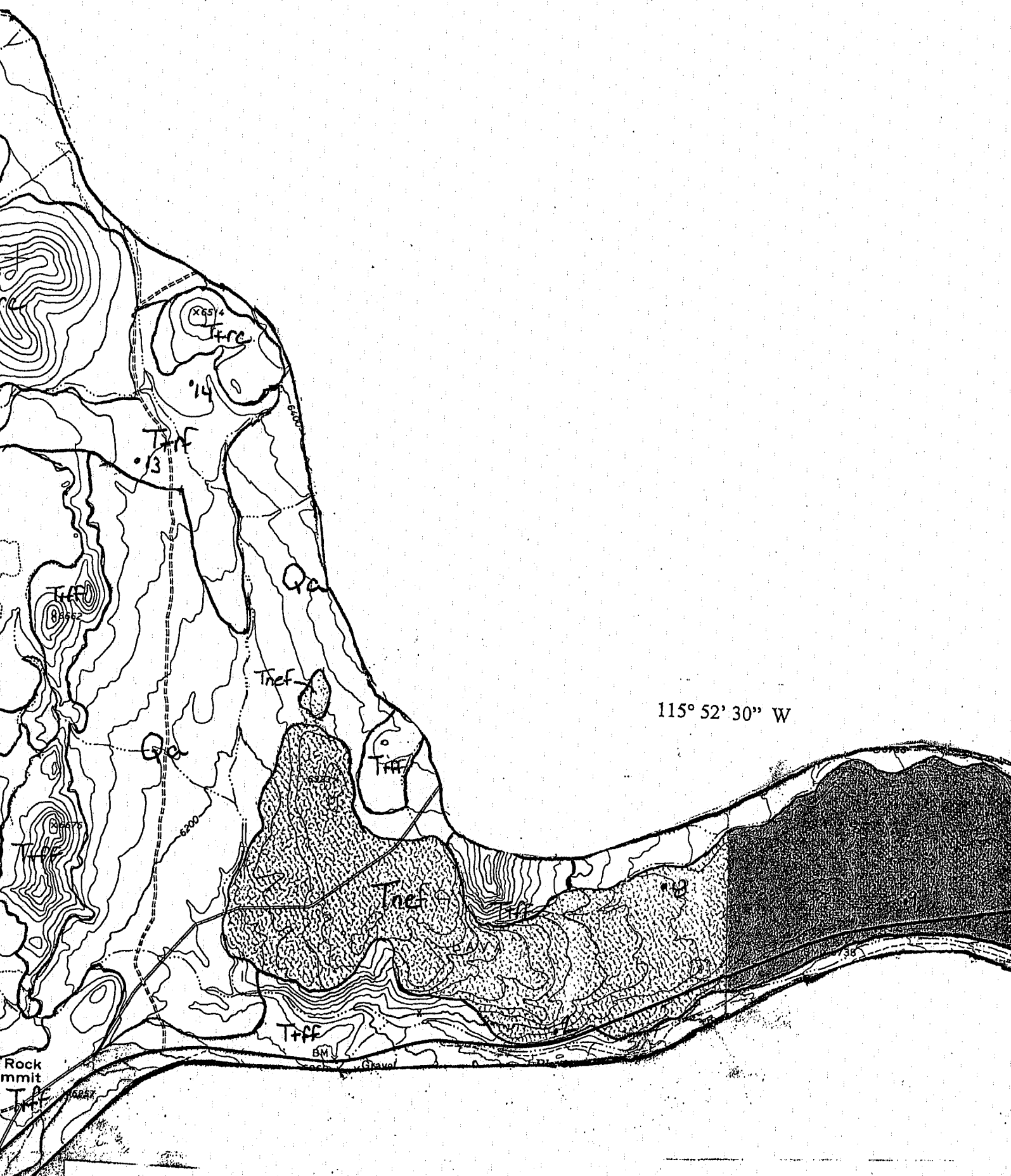


38° 30' N

115° 55' W

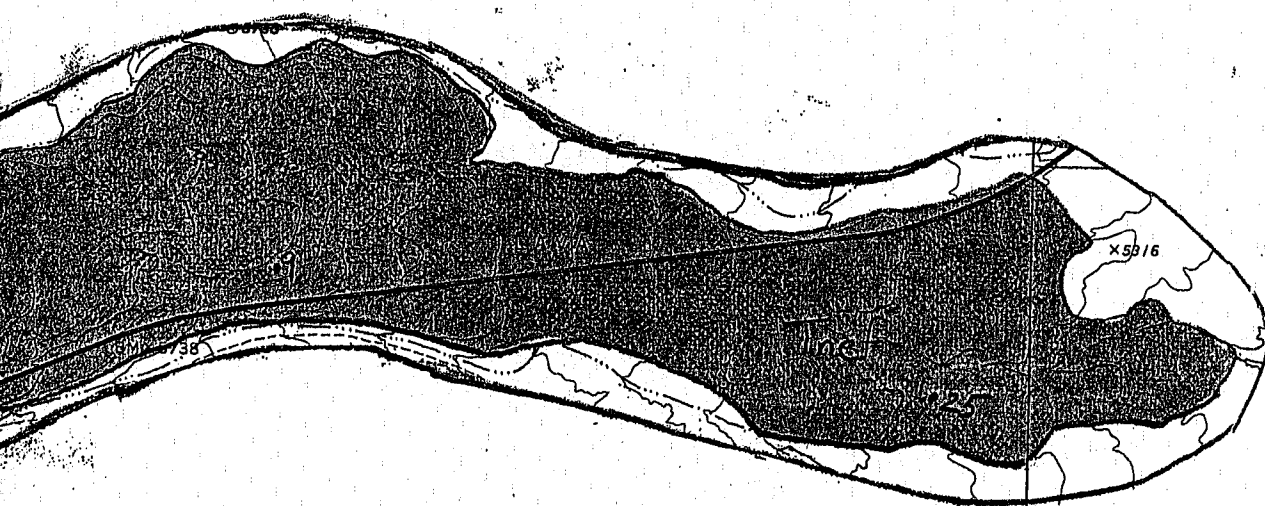


115° 55' W



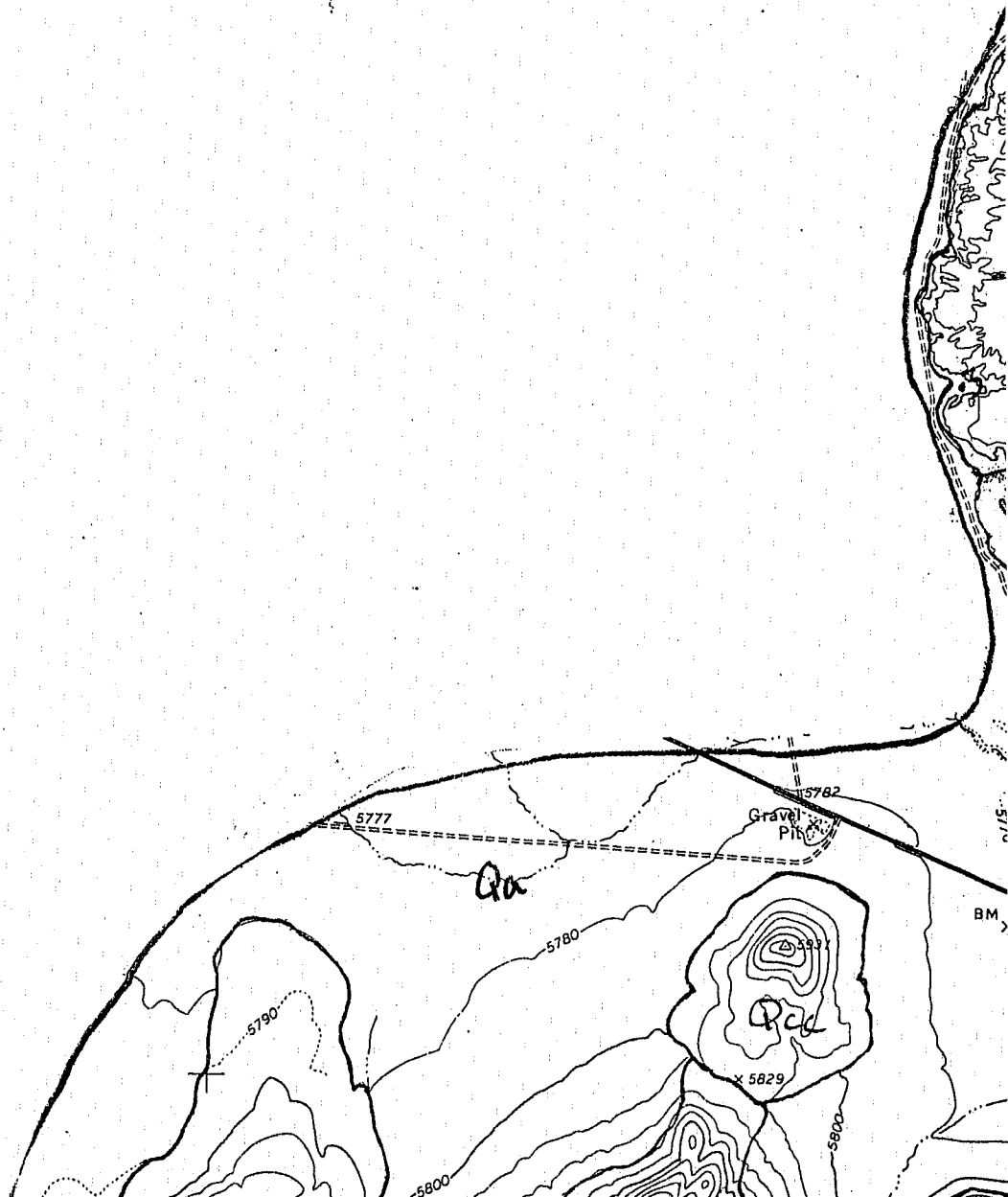
115° 52' 30'' W

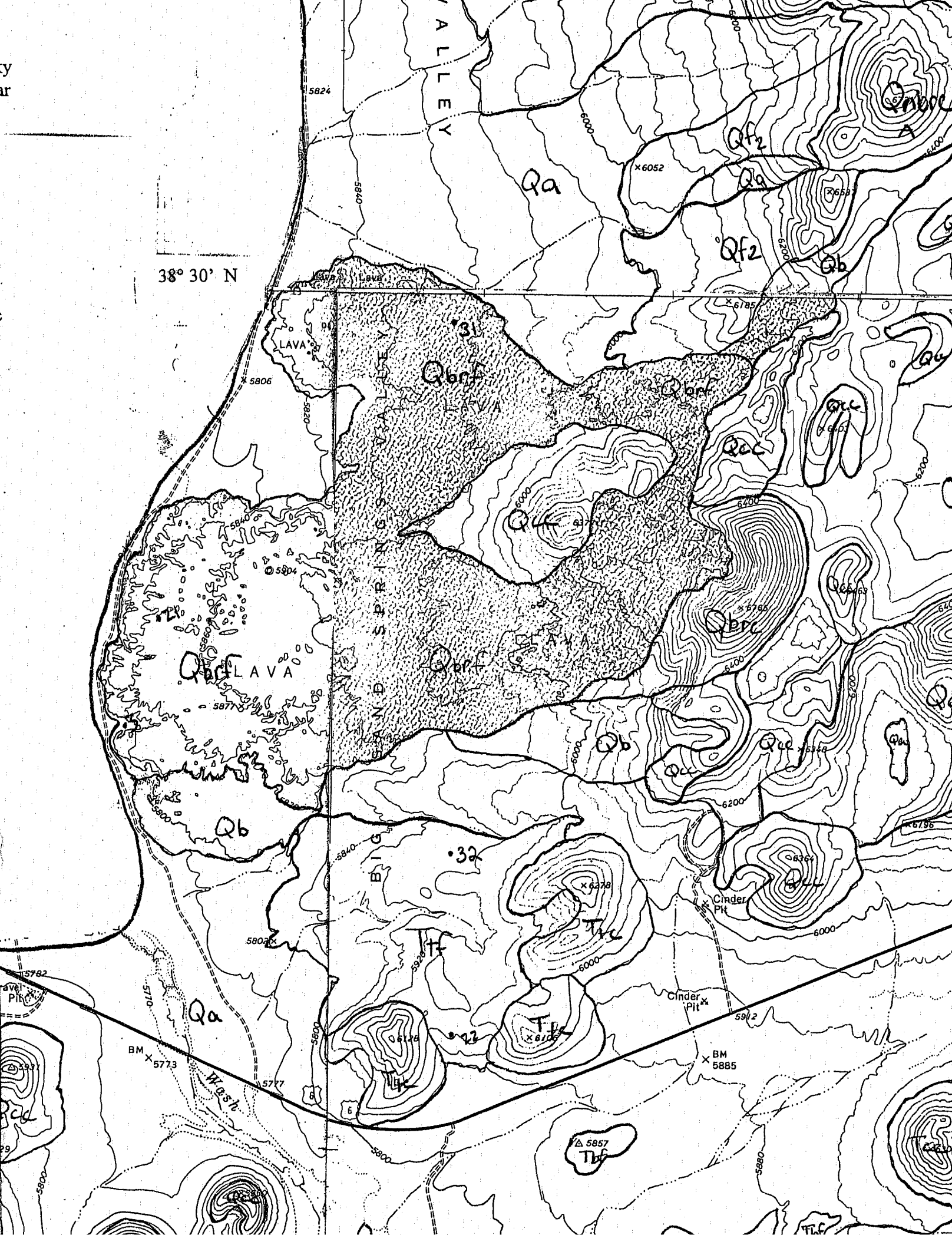
30" W

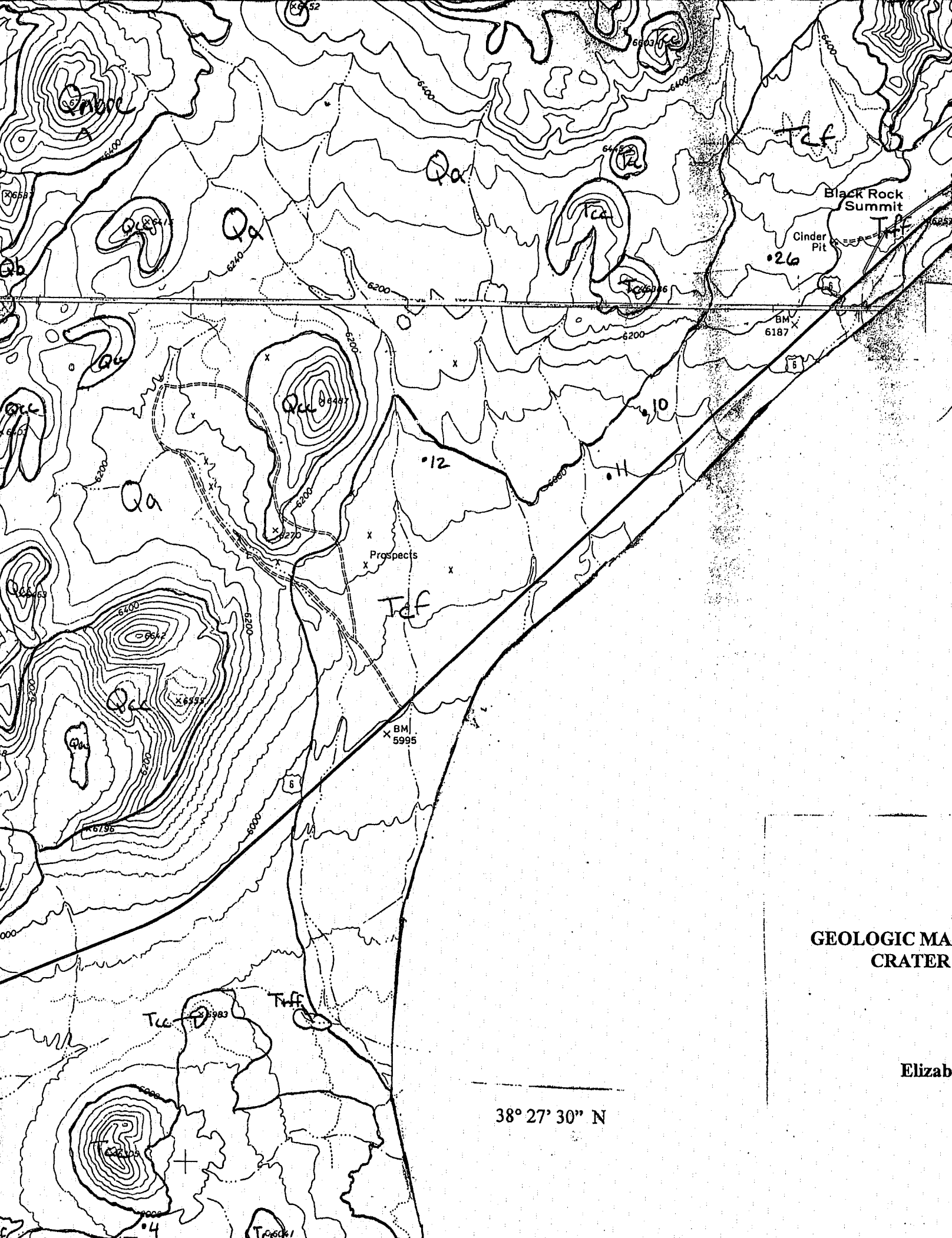


Tgc/Tgf	G-Cone and G-Cone Basalt Flow – 1.5 m thickness – blocky – xenoliths of peridotite and dunite
Tnef	Northeast Finger Basalt Flow - 1.22 ± 0.2 Ma – 2 to 20 m thickness – blocky A'a – xenoliths of rafted tuff and dunite – steep $> 40^\circ$ flow fronts , columnar jointing
Tcf	Central Basalt Flow - 3.1 ± 0.4 Ma – 1 to 4 m thickness – blocky - xenoliths of rafted tuff – highly weathered
Ttrc/Ttrf	Tower Road Cone and Tower Road Basalt Flow – 0.5 to 3 m thickness – Blocky to A'a – xenoliths of peridotite – massive overlain by highly vesiculated lava
Ttff	Oligocene Tuff - 32.8 Ma (tuff) –Rhyolitic to andesitic crystal vitric to vitric welded and nonwelded ash-flow tuff with minor air-fall tuffs and water-laid sedimentary rocks

38° 27' 30" N



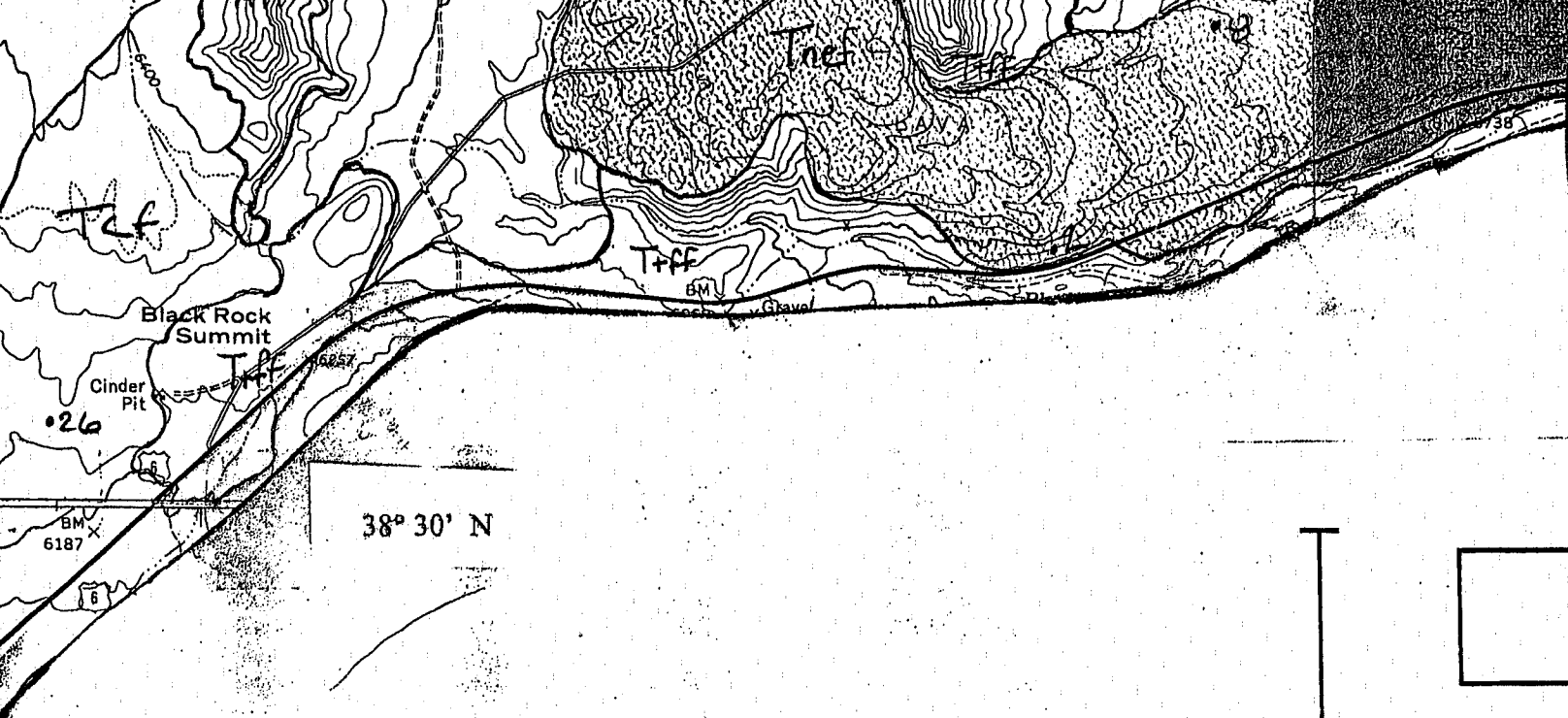




GEOLOGIC MAP
CRATER

Elizabeth

38° 27' 30" N



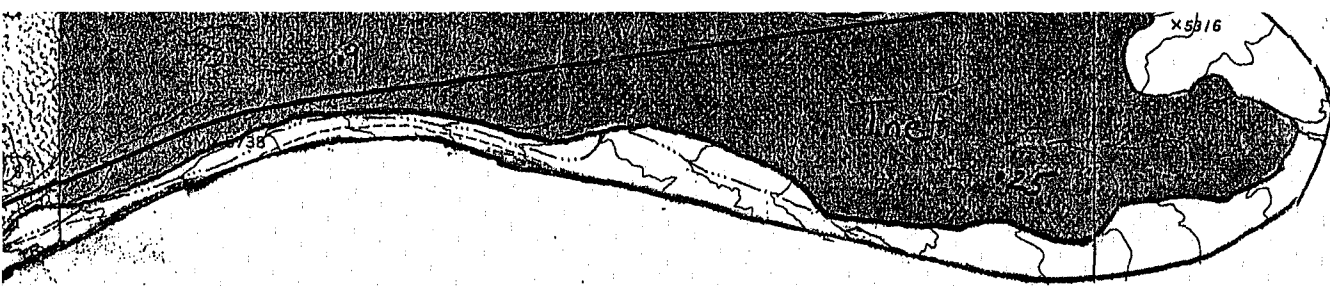
**GEOLOGIC MAP OF NORTHERN LUNAR
CRATER VOLCANIC FIELD**

by

Elizabeth Kay Stickney

2003

Quaternary



Quaternary

Qbf

Qa

Qcc

Qbrf
Qbrc

Qf3
Qnbrc

Qf2
Qnbrc

Qf1
Qnbrc

Tbf

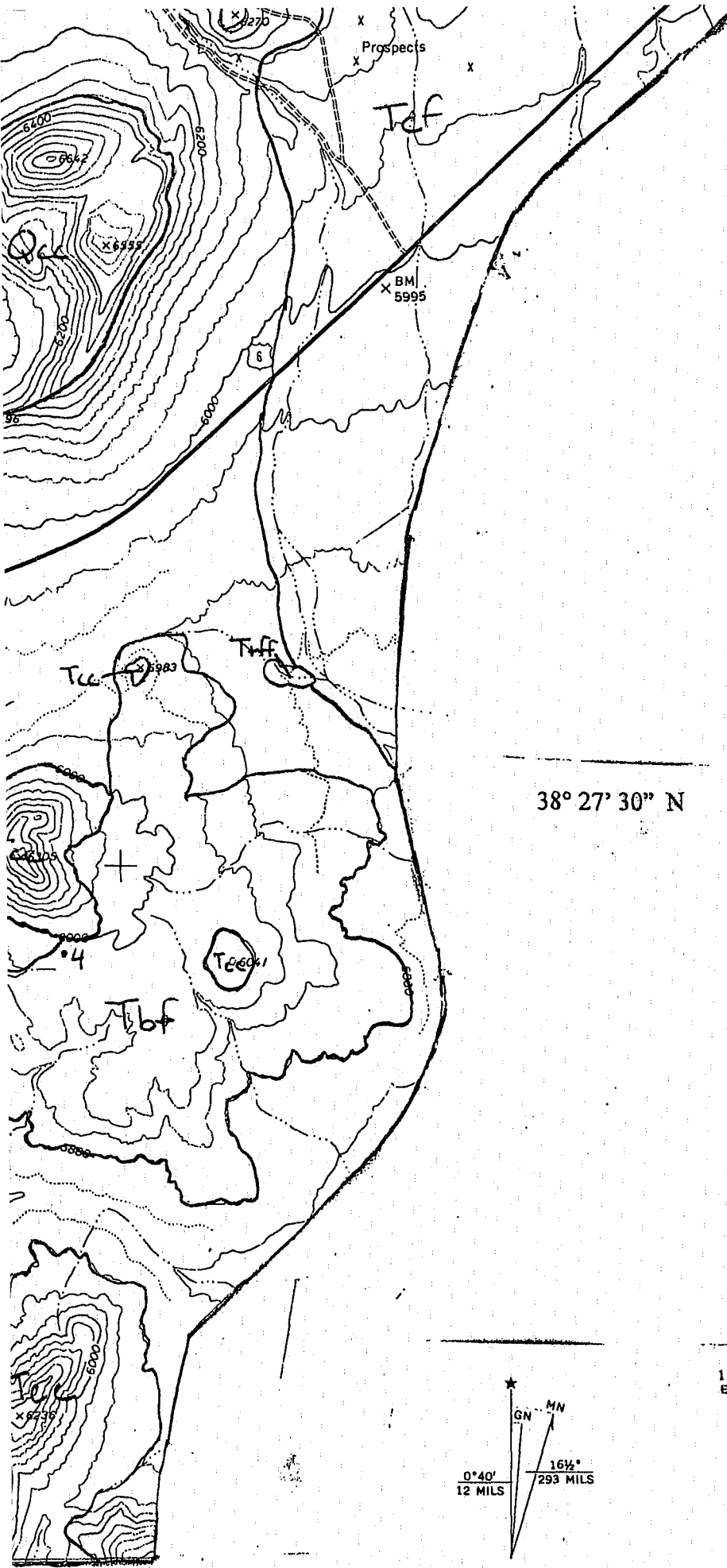
Ttf
Ttc

Thf
The

Tgf
Tgc

Tcc

Pleistocene



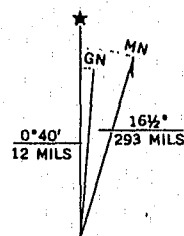
GEOLOGIC MAP OF NORT CRATER VOLCANIC

by

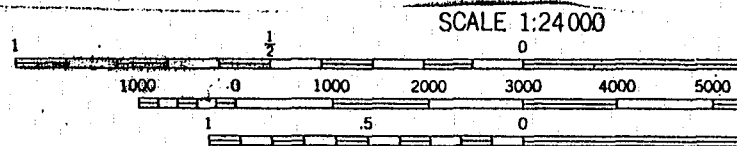
Elizabeth Kay Stiel

2003

38° 27' 30" N



UTM GRID AND 1968 MAGNETIC NORTH
DECLINATION AT CENTER OF SHEET



CONTOUR INTERVAL 40 FEET
DOTTED LINES REPRESENT 20-FOOT CONTOUR
DATUM IS MEAN SEA LEVEL

**GEOLOGIC MAP OF NORTHERN LUNAR
WATER VOLCANIC FIELD**

by

Elizabeth Kay Stickney

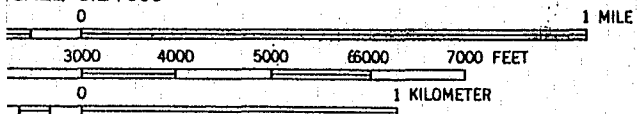
2003

Quaternary

Tertiary

Tbf

SCALE 1:24000



CONTOUR INTERVAL 40 FEET
DOTTED LINES REPRESENT 20-FOOT CONTOURS
ELEVATIONS ARE MEAN SEA LEVEL



QUADRANGLE LOCATION

